Chalcogenide Materials for Renewable Energy Applications

Olivia M. Lenz

A dissertation

submitted in partial fulfillment of the

requirements for the degree of

Doctor of Philosophy

University of Washington

2017

Reading Committee:

Kannan Krishnan, Chair

Marjorie Olmstead

Fumio Ohuchi

Brandi Cossairt

Program Authorized to Offer Degree:

Materials Science and Engineering

University of Washington

Abstract

Chalcogenide Materials for Renewable Energy Applications

Olivia M. Lenz

Chair of the Supervisory Committee:
Professor Kannan M. Krishnan
Materials Science and Engineering

In the effort to reduce dependence on non-renewable energy resources, photovoltaics (PV) have long been an attractive and plausible alternative. Silicon-based PV dominates the industry, but the scientific community continues to investigate alternate materials and processes to bring down the cost per Watt for installed solar. One of the areas of research explored in this thesis is non-silicon based PV with a focus on non-toxic, earth abundant nanomaterials. First, two iron-based chalcogenides are synthesized and characterized, but fail to perform well enough for real PV device testing. The reason for this non-performance is investigated and is likely due to sulfur-vacancies in the material. Staying within the chalcogenide family, WSe_2 is next investigated for PV applications but it too suffers from inherent issues that prevent its use as an absorber material in solid-state solar cells. Finally, the dual polytypes of WSe_2 are exploited for electrocatalytic

water splitting and H_2 gas generation applications. Moving away from precious-metal catalysts for water splitting and from traditional steam reforming for H_2 generation can increase the production of H_2 while limiting the amount of CO_2 released into the atmosphere.

TABLE OF CONTENTS

LIST OF FIGURES

LIST OF TABLES

ACKNOWLEDGEMENTS

Thank you to Prof. Krishnan for giving me the space and freedom to explore these interesting chalcogenide materials for solar cells and hydrogen evolution. Thank you to my committee members for your time and expertise. Thank you to the NASA Space Technology Research Fellowship for supporting my PhD research. To each PI and their group members who welcomed me in to their lab each summer – Dr. Sue Carter (UCSC/NASA Ames), Dr. Maikel van Hest (NREL), Dr. Jon Owen (Columbia), and Dr. Mike Piszczor (NASA Glenn) – thank you! I would not have completed this research without the support of Dr. Brandi Cossairt and I cannot thank you enough for the support you have given me over the past few years. To Danielle – thanks for taking a chance on my weird WSe_2 nanoflowers and testing them for HER catalysts! Thank you to the whole Cossairt lab for welcoming me so readily and completely, it's has been a joy to be a pseudo group member for the past few years.

My deepest gratitude goes out to my family and friends who have supported me without question through this PhD journey. Though too numerous to include everyone here, I'd like to specifically say thank you to Mom, Dad, Madeleine, Elizabeth, Garrett, Grammie, Papa, Kali, Jenni, Sarah K., Stephanie R., Cynthia, Danni R., Danielle, Sarah V., Curtis, Danni H., Stephanie C., Andrew, Dana, Chad, and my cat, Luna.

Chapter 1. INTRODUCTION

Global energy consumption and global climate change are inextricably linked. As more energy is produced from conventional energy sources, such as coal and petroleum, more CO_2 gas is produced, negatively impacting Earth's atmosphere and climate. Reduction of CO_2 emissions is critical for slowing global climate change and one of the most promising ways of achieving that goal is through renewable energy resources. Currently, approximately 20% of the global energy needs are being met with renewable sources, the majority from hydroelectric power. Less than 1% comes from solar power, a vastly underutilized source.[1] In the US, current electricity needs could be met by using 0.4% of the US land mass for solar energy conversion using 21% efficient modules, an area approximately half of that which is already dedicated to biomass renewable fuel production.[2] CO_2 is a byproduct of steam reformation of methane for production of H_2 gas and this source of CO_2 can be eliminated by moving to production via the hydrogen evolution reaction (HER), where water is split to produce the H_2 gas.[1] H_2 gas has applications in transportation, but is also under investigation for use in renewable battery technology.

There are three main challenges to increasing the terrestrial energy-production share of solar: intermittency, cost, and scalability.[2] Away from our planet, solar energy is critical for space exploration and is subject to additional constraints. Power supply weight and efficiency is critical to mission success; less expensive, lighter weight solar cells can allow for more science experiments or extend the life of an off-planet mission. The same solar cells could be implemented terrestrially, collectively working towards the Department of Energy's target of \$0.06/kWh for solar-generated energy by 2020.[3] This thesis seeks to impact the cost and

scalability factors by investigating novel absorber materials for high-throughput solar cell fabrication with a focus on earth-abundant materials.

Cost is also a driving factor for development of catalysts for HER. Pt is considered the best catalyst for HER, however the cost of the amount of Pt needed to build a commercial HER plant would be unsustainably high. Lower cost catalyst materials and flexible electrode fabrication are motivating factors for the HER material work in this thesis.

Overall, this thesis will describe attempts to fabricate photoactive iron pyrite (FeS_2) nanomaterials and discuss why ultimately it is not a suitable material for photovoltaics. Addition of Ge or Si to FeS_2 to make $Fe_2(Ge/Si)S_4$ is suggested as an alternative to FeS_2 that addresses some of iron pyrite's deficiencies, but ultimately it too is found to be unusable for photovoltaic applications. WSe_2, while containing more toxic elements than FeS_2 and Fe_2GeS_4, is another earth-abundant material that is synthesized and explored herein as a solar cell absorber. WSe_2 is also explored as a catalyst for HER, with an in depth investigation into developing syntheses that produce predominately metallic WSe_2 and characterizing the impact of changes on the nanocrystal surface on activity as a catalyst.

1.1 Energy Technologies

1.1.1 *Photovoltaic Energy Conversion*

It is possible, but expensive, to achieve widespread solar adoption with traditional (first generation) silicon cells alone. Shockley and Queisser have described the efficiency limitations of single-junction solar cells, where the power conversion efficiency (PCE or % efficiency) is related directly to the bandgap (E_g) of the material under one sun illumination.[2] Crystalline silicon, with an indirect bandgap of 1.1 eV is near the peak of the resulting "Shockley-Queisser" graph (Fig. 1.1). The second generation of photovoltaic devices has focused on lowering the cost

of solar cells by utilizing thin film technology to minimize the amount of material needed for a cell. However, these cells suffer from an efficiency loss in comparison to first generation cells (Fig. 1.2). Very recently, perovskite-based solar cells, a second-generation type cell, have demonstrated large efficiencies while utilizing minimal material and potentially high-throughput processing.[4] The third generation of devices seeks to increase efficiency while maintaining low costs by fundamentally changing the way solar cells are structured. These devices no longer rely on p-n junctions, but utilize tandem cells, hot-carriers, or multiple exciton generation to break past the Schockly-Queisser limit.[5] The absorber materials explored in this thesis are targeted for second and third generation photovoltaics.

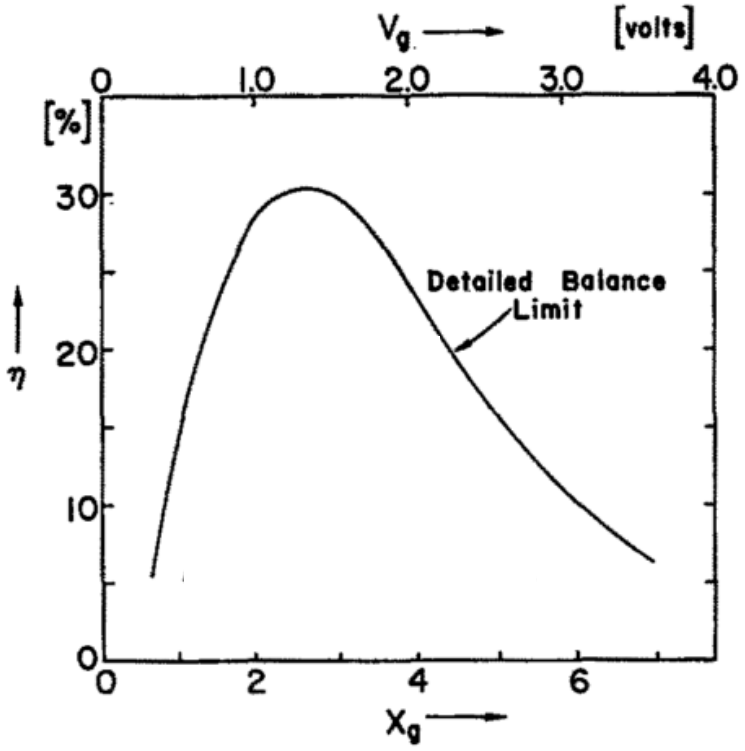

Figure 1.1. Shockley-Queisser graph relating bandgap (X_g here) of a material to overall efficiency in a *p-n* homojuction device.[2]

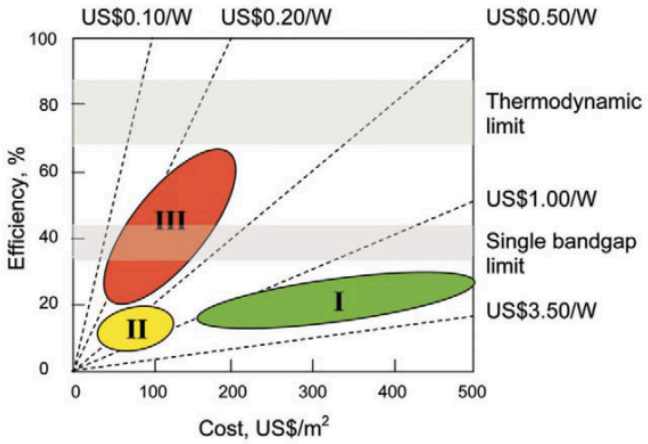

Figure 1.2. Visual representation of first (I), second (II), and third (III) generation photovoltaic device costs and efficiencies. Included are the Shockley-Queisser (single bandgap limit) and thermodynamic limit ranges for reference.[6]

1.1.2 *Hydrogen Evolution*

Eliminating reliance on fossil fuels also necessitates the development of inexpensive batteries to capture excess electricity generated by a photovoltaic device for use when the sun is down. One way to do this is to increase production of hydrogen-based fuels, specifically electrolyzing water to create H_2 and O_2 to store excess solar-generated energy until needed. The hydrogen evolution reaction (HER, eqn 1) is best catalyzed by Platinum metal; however, Pt metal is expensive and efforts have been made to find replacement catalysts made from non-precious metals.[1]

$$2H^+ + e^- \rightarrow H_2(gas) \qquad \text{(eqn 1)}$$

This work investigates the use of WSe_2 nanomaterials as a catalyst for HER, as WSe_2 is less expensive per gram than Pt. Furthermore, because the WSe_2 nanocrystals are fabricated colloidally, the energy input is low and the catalyst can be applied to a wide variety of electrode materials and shapes. HER is also a potential replacement for the current commercial process of steam reformation of methane gas, as the latter produces a significant amount of CO_2 gas byproduct. The cost of precious metal catalysts are prohibitively high for this application, so

utilizing a non-precious metal catalyst for the commercial production of H_2 gas will also aid in decreasing the amount of CO_2 released into the atmosphere.

1.2 CHALCOGENIDE MATERIALS

This work is focused on the class of inorganic chalcogenide materials for energy applications for two reasons: semiconducting nature and materials availability. The chalcogenide materials, compounds containing S, Se, or Te, make up a large group of compounds, many of which are semiconducting (Table 1.1). A semiconductor with a bandgap between 0.75 – 2.0 eV is projected to produce a 20+ % efficient *p-n* homojunction solar cell and many chalcogenide materials have a bandgap in the desired range.[7] In a widely cited plot developed by Wadia *et al*. relating a material's extraction cost to its annual electricity potential, the majority of compounds considered are chalcogenides, indicating that this class of materials should be seriously considered for low-cost photovoltaics (Fig. 1.3).[8] Other chalcogenide materials are metallic in character, which is beneficial for HER catalysis. Predominate PV and HER catalyst materials are expensive and/or have low availability (In, Pt) and thus there is a desire to move away from them in order to effectively expand the presence of solar energy and green hydrogen production. Sulfur is the most abundant of the chalcogenides, followed by selenium and then tellurium.[9] The use of transition metal chalcogenides, such as the FeS_2 and WSe_2 discussed in this work, takes advantage of both their materials availability and ideal electronic character in pursuing increased use of renewable energy resources.

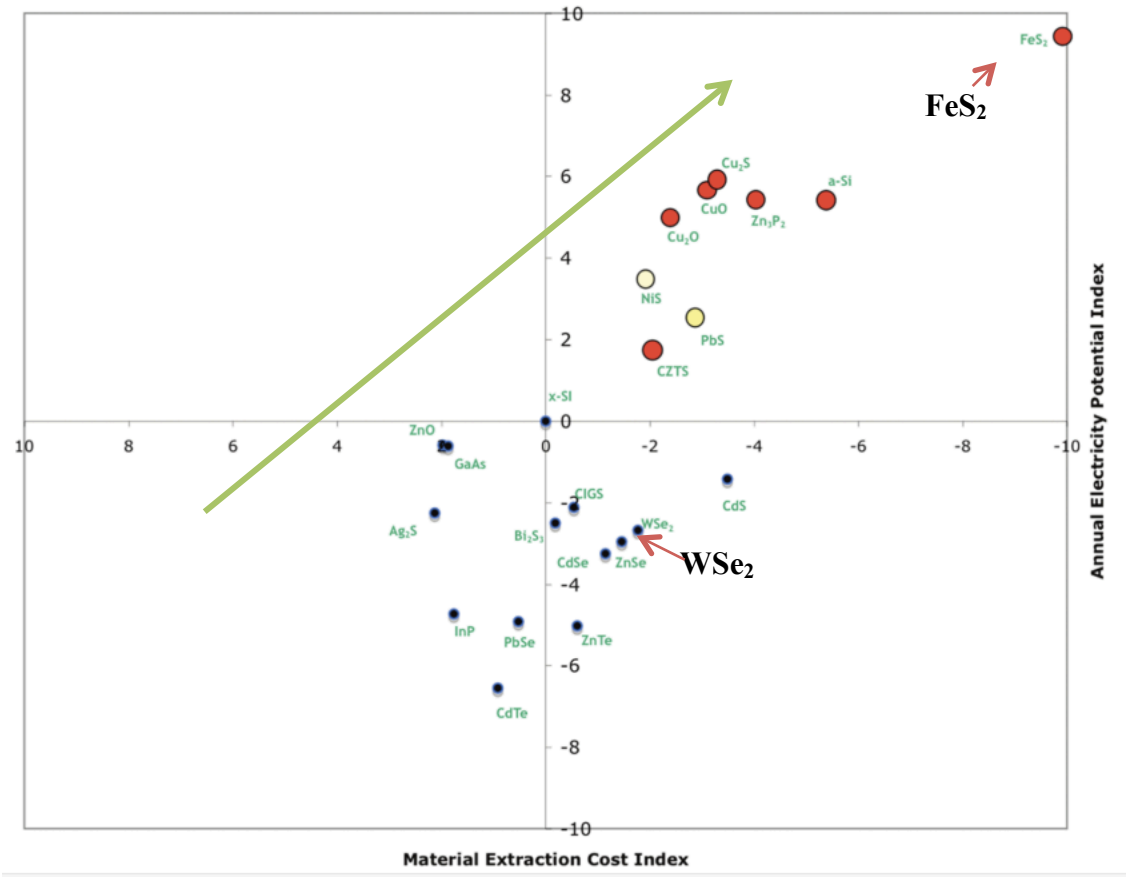

Figure 1.3. Plot from Wadia et al. comparing various potential PV absorber materials by their extraction cost and annual electricity potential (normalized to crystalline silicon).[8] The further right and upwards on this plot (indicated by the arrow), the more attractive the material for PV.

TABLE 1.1. CHALCOGENIDE MATERIALS AND THEIR BAND GAPS, ADOPTED FROM QURASHI *ET AL.*[10]

Material	*Band gap (eV)*	*Band gap type*
CdSe	1.74	Direct
CdS	2.42	Direct
CdTe	1.4	Direct
ZnSe	2.7	Direct
ZnS	3.54/3.9	Direct
ZnTe	2.25	Direct
Cu_2S	1.2	Direct
PbSe	0.27	Direct
PbS	0.37	
SnS	1.0	Indirect
SnS_2	2.2	
GaSe	2.1	Indirect
FeS_2	0.95	Indirect
WSe_2	1.2	Direct

1.3 NANOMATERIAL MOTIVATION

In addition to utilizing chalcogenides for their material abundance and electronic structure, this work describes the use of these materials on the nanometer (<100 nm) scale. Wadia and co-workers calculated that if a 75% reduction in material can be achieved in a solar cell, as is possible in a nanostructured device, the overall cost of 10% PCE PV would be equivalent to that of a traditional/current device with 20% PCE.[8] There are a number of benefits to using nanomaterials, including band gap engineering, solution synthesis and low-temperature, wide-area thin film processing. As the physical size of a material shrinks to below twice the exciton Bohr radius, the material will enter the quantum regime. Here, as the radius shrinks the bandgap will widen due to the energy bands narrowing and shifting. This property expands the versatility of chalcogenide nanomaterials, most notably PbS. However, this thesis is interested in nanomaterials because of their potential for solution synthesis and ink-based thin film formation. Nanomaterials such as those described herein can be prepared by a colloidal solution method, relying on the LaMer principle of nucleation at a critical concentration followed by a growth period.[11] A solution method could cut down on manufacturing costs of the final product or application, as there are no high vacuum equipment or high temperature (>800 ^{o}C) processes required. The ability to form an 'ink' from colloidal nanocrystal (NC) suspensions opens the possibility for the material application in a roll-to-roll printing, large scale manufacturing method, further decreasing cost of the end product.

HER catalysts prepared by a solution route are advantageous for two reasons: the NCs can be easily applied to unusually shaped or textured electrodes via dropcasting from a NC suspension and the small NC size maximizes the surface area to volume ratio. Often a catalyst's

activity is due to unpassivated atoms or defects on the surface of the material, so maximizing the surface area should increase overall efficiency of the catalyst by providing more active sites.

Overall, this research aims to promote progress in renewable energy adoption by investigating low-cost versatile nanomaterials. Development of non-precious metal hydrogen evolution catalysts is vital for eventual commercialization of water-splitting batteries and non-CO_2 forming H_2 gas production. The research described herein attempts to meet some of the continuing challenges for both the PV and catalysis fields: to develop simple, safe, reproducible, and rational syntheses of nanomaterials and to connect the nanocrystal surface with application efficacy.[12]

Chapter 2. IRON CHALCOGENIDES FOR PHOTOVOLTAICS

2.1 IRON PYRITE – PROMISES AND PROBLEMS

Leading silicon photovoltaic (PV) technology efficiency increases typically are achieved at the cost of module price. Other commercial materials (CIGS, CdTe), while moderately efficient, contain toxic elements. In an effort to drive down the cost of PV and increase safety, the scientific community turned to earth-abundant materials. From the excellent review of material costs vs. projected annual electrical potential by Wadia *et al.* and a review of potential PV material elemental toxicity, iron pyrite (pyrite, FeS_2) was clearly an attractive material (Fig 1.3).[8,9] In the years following these publications, iron pyrite research intensified and much of the initial research explored new ways of fabricating FeS_2, but more recent research has focused on identifying the reasons behind pyrites poor performance in actual solar devices. FeS_2 has an almost ideal band gap of ~0.95 eV and is highly absorbing (absorption coefficient $>10^5$ cm^{-1}), meaning a minimal amount of material would be required to absorb 90% of incident photons (a layer 40-200 nm thick), much less than that required by silicon (~300 um thick).[13] Additionally, pyrite is composed of earth-abundant and non-toxic materials, which is not true of current commercial materials such as CuInGa(S/Se) or CdTe. While a variety of solar devices have been fabricated incorporating pyrite, no device has exceeded an efficiency of 3% and, in general, efficiencies less than 0.3 % are reported.[14–17]

The PV community began investigating FeS_2 as an absorber layer in the late 1970's and the state of pyrite for PV was summarized in an extensive review by Tributsch and colleagues in 1993, covering everything from electronic structure (the ~0.95 eV band gap is near the top of the Shockley-Queisser plot) to the ability to produce phase-pure pyrite.[13,18–21] There exists a polymorph, marcasite, which was thought to have a smaller E_g and thus, if present, would be

detrimental to a pyrite-based solar cell.[22,23] It was highlighted that pyrite symmetry and coordination is reduced at the surface of any crystal, which was posited to lead to unfilled states within the band gap. These states within the bandgap would trap carriers and quench any photovoltage. The Tributsch group fabricated and tested a number of PV cell configurations featuring pyrite as the absorber layer. In a photoelectrochemical cell (PEC), efficiencies of 2.8% and short-circuit current densities (J_{sc}) of 42 mA cm^{-2} were recorded, however the open circuit voltage (V_{oc}) was limited to 187 mV.[13] In the same publication, they demonstrated a solid state cell where J_{sc} reached 30 mA cm^{-2}, but V_{oc} was <100 mV. In seeking to replace organic dyes with thin inorganic films, the group also fabricated a FeS_2-sensitized TiO_2 cell, however no J-V curves were reported. In the discussion of their results, the authors point out that the low V_{oc} could be due to a high concentration (10^{14} cm^{-2}) of surface defect states in the band gap and that those states likely pin the Fermi level. The authors sum up the challenges facing this material and include formation of pure stoichiometric pyrite samples, techniques for fabricating thin (5-30 nm) layers, and investigating the impact of structural defects on electron transport.[13] A decade later, the same main challenges are highlighted, as work in the intervening years brought no conclusive data.[24,25] The introduction of pyrite nanostructures with the renewed interested in the material was motivated both by the possibility of low-cost 'inkjet'- type deposition and that it is challenging to keep non-surface defects in nanostructures.

Producing pure, stoichiometric pyrite was initially the greatest research concern; avoiding the smaller band gap marcasite would be critical to increasing the V_{oc} of any solar cells, as would be avoiding the impurities found in natural pyrite crystals.[26] Both natural and synthetic crystals were often found to be sulfur-deficient.[27] Marcasite was found to be a stoichiometric kinetic product and not S-deficient, indicating that with time and heat, the polymorph could be removed,

leaving pure pyrite.[28,29] Indeed, many groups have utilized this strategy to form phase pure pyrite.[30–33] However, as noted in a number of studies and determined in this research, the phase purity can only withstand annealing temperatures of ~400 ^{o}C under specific conditions (Figures 2.1, 2.2).[25,34–37] At higher temperatures the material decomposes into FeS_{1-x} phases. Various fabrication methods including d.c. magnetron sputtering[35], chemical vapor transport[38–42], flux synthesis[43], sulfurization of iron containing films[30,44–46] or nanowires[33], dissolution of natural pyrite[47], aerosol-assisted chemical vapor deposition[48,49], and solution syntheses at both regular[17,31,32,50–74] and elevated pressures[14,57,75–83], have obtained pure iron pyrite. Purity is usually determined via X-ray diffraction (XRD) or Raman spectroscopy, but many of those who believe their material to be phase-pure often report S-deficiency[17,30,40,44,62,77,80,84,85] or excess[31,47,60,65,83] via energy dispersive x-ray spectroscopy (EDS) or inductively coupled plasma (ICP) techniques. Marcasite and pyrite have different magnetic properties and it was proposed that low temperature magnetism measurements could confirm phase purity.[82] When the magnetic response of the pyrite NCs fabricated for this report was tested, no anomalies were found in the magnetism measurements (Figure 2.3); the results show a response only from a paramagnetic material, indicating only pyrite is present.

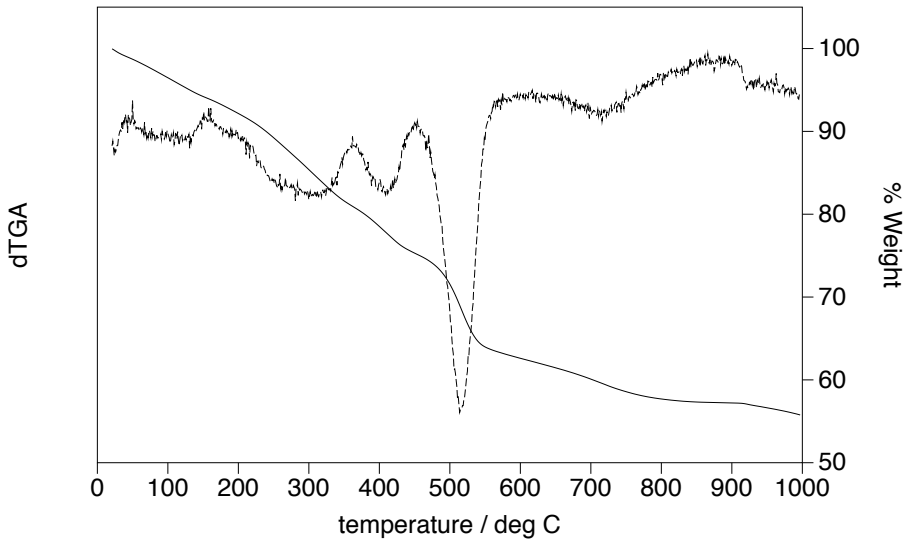

Figure 2.1. Thermogravametric analysis under N_2 of nanocrystal FeS_2 showing the change in weight % with temperature (solid line) synthesized by the Puthussery method.[59]

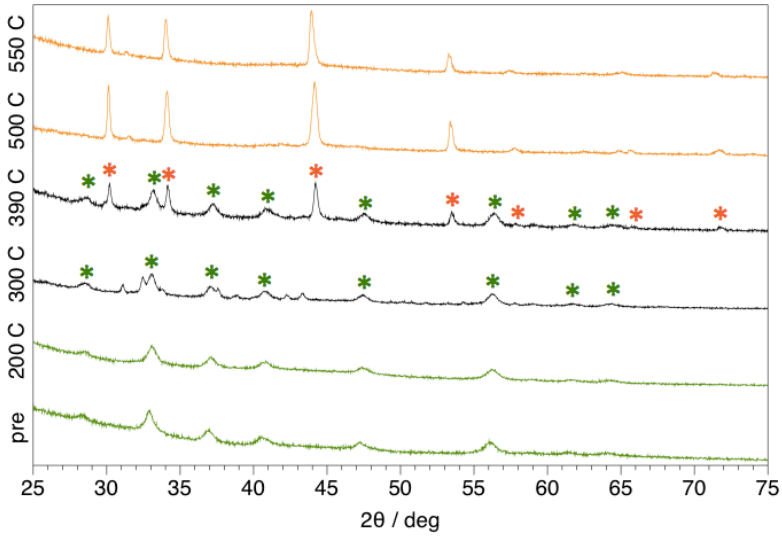

Figure 2.2. XRD annealing study of the sample in Figure 1, demonstrating the iron pyrite (green, PDF#01-071-0053) decomposition into pyrrhotite FeS (orange, PDF#00-024-0220). Samples were deposited on glass slides and then annealed in a tube furnace under Ar for 30 minutes at the specified temperature.

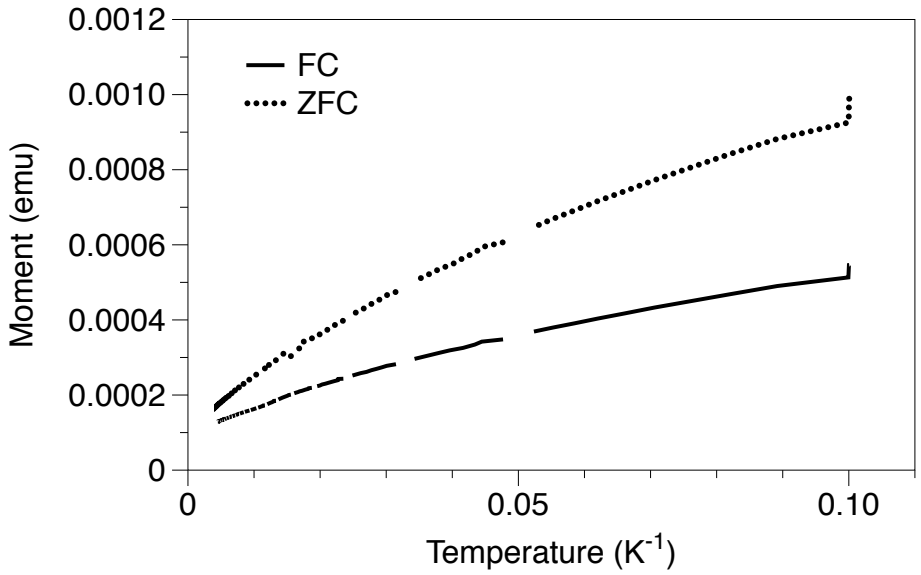

Figure 2.3: Zero-field cooled (ZFC) and field cooled (FC) magnetic measurements of phase-pure pyrite nanocrystals fabricated by a colloidal solution method. Measurements collected on a Physical Properties Measurement System (PPMS) under a field of 1000 Oe.

The band structure of iron pyrite has been long investigated, with particular attention paid to determining why all pyrite devices showed a lower than expected V_{oc}.[23,86–91] Defects from sulfur vacancies (V_S), both in the bulk and at the surface, were put forth early on as the problem behind the low V_{oc}[27,39,40]. Much work was done by the Tributsch group and one early study with XRD by Birkholz *et al.* carefully measured changes in unit cell parameters to determine that their sample had V_S in the "percent range," (concentration of ~10^{21} cm^{-3}), however quantum efficiency (QE) measurements led them to believe the defects did not lead to higher recombination rates.[27] Strikingly, the measured structural changes were very small and did not impact the long range order, leading researchers to conclude that the vacancies must be point defects homogenously distributed so as to not construct a superlattice.[40] Such an observation led the researchers to develop a iron-sulfur phase diagram where pyrite is not strictly a line compound, but can tolerate a small range of sulfur concentrations (Fig. 2.4). It was calculated that 5% V_S affects 25% of the Fe centers in a typical pyrite structure and proposed that the

vacancy formation energy of V_S was ~0.3 eV; however, the calculation did not specify if the vacancies were found in the bulk or on the surface.[27] The change in symmetry from O_h to C_4 with a sulfur vacancy causes deviations in the 3*d* band splitting and thus a defect state develops; but the authors were not able to predict if it overlapped the conduction band (CB) or if it was a discrete level in the band gap. In a first clarification step, low temperature luminescence measurements were reported by Birkholz *et al.* on the order of $< 10^{-7}$, a low yield.[27] Such a low yield indicates that the defect states are likely located within the band gap, quenching the photoluminescence (PL) and limiting the V_{oc}. Additionally, a temperature dependent V_{oc} study concluded that the low V_{oc} was due to mid-band gap states from sulfur vacancies, resulting in sharp band bending at a junction with Pt (Fig. 2.5) and thus limiting V_{oc} to ~200 mV.[39] Further confirmation of a state within the bandgap can be inferred from very early measurements, where the Fermi level of FeS_2 was often found at or near the VBM, likely pinned due to a high level of defect states.[92]

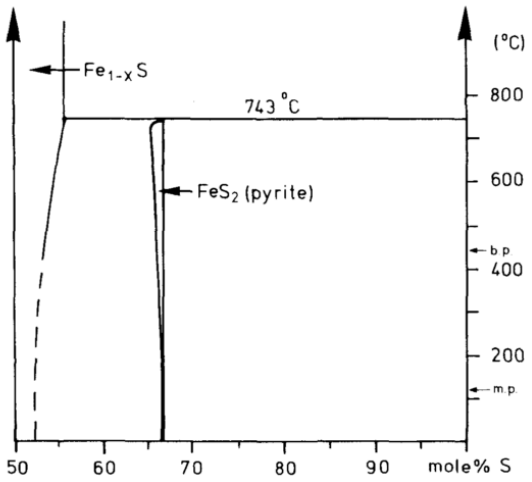

Figure 2.4. Phase diagram from Fiechter *et al.* demonstrating range of S-deficient iron pyrite that remains structurally the same.[40]

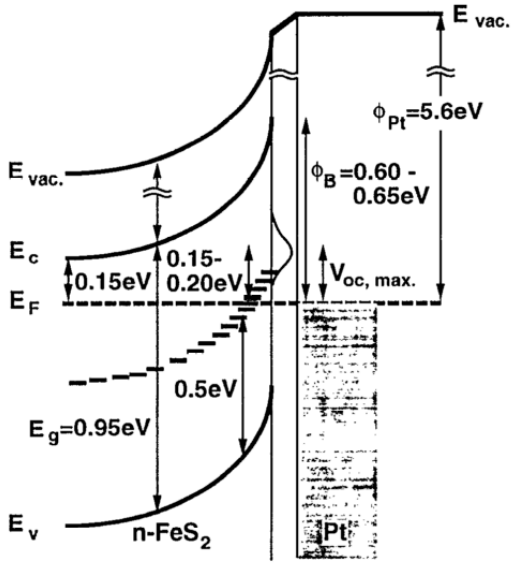

Figure 2.5. Example band diagram of FeS_2/Pt junction, illustrating mid-gap states and sharp band bending at the interface, leading to a small V_{oc}.[39]

Following the publication by Buker *et al.*, there is no more work published on the low V_{oc} of FeS_2 until 8 years later, when the Tributsch group brought the topic of pyrite for PV up again at a workshop on quantum solar energy conversion.[93] Though the existing research indicated that sulfur-vacancies were the culprit, it was not until another decade passed that scientists again looked to S-vacancies as limiting V_{oc}. And at first, some scientists wondered if the V_{oc} was limited by the presence of marcasite, as the presence of marcasite's reportedly low (0.34 eV)[94] band gap could explain the low V_{oc}. Two theoretical studies of the phase stability between pyrite and marcasite confirmed that marcasite could be formed under kinetic reaction conditions whereas pyrite was the more thermodynamically stable polymorph and modeled marcasite's band gap at 1.3 eV, which is much higher than the previously published experimental value.[95,96] Due to the nature of the experiment that originally determined marcasite's band gap – a natural, impure sample and thermal resistivity measurements – the authors of the theory study believed their model to more accurately reflect reality and thus any marcasite presence would not

cause the low V_{oc}.[96] This is later confirmed by experiments in the Law group, where they produced a 50% marcasite sample and did not see a reduction in optical band gap.[32]

Unsatisfied by the theory that S-vacancies caused the low V_{oc}, as it did not "directly address the distinctions between n-type single crystals and p-type films," Zunger's group postulated that the sulfur deficiency was not necessarily caused by sulfur vacancies.[97] Using a density functional theory and plane-wave projector augmented-wave model, the authors found the formation energy of V_S under S-rich conditions was almost twice that of a Fe-vacancy and that V_S should only form under S-poor conditions; but even then the formation energy is rather high at 2.42 eV as a function of chemical potential (Fig. 2.6). These high formation energies should lead to a low concentration of bulk vacancies and consequently, should not be responsible for the Fermi level pinning. Instead, it was argued that pyrite decomposes to or spontaneously forms S-deficient phases, such as FeS and $Fe_{0.877}S$ with a little heat (Figure 2.7).[97] These other phases are known to be metallic and could form especially easily on the surface of a pyrite film, where in S-poor conditions the formation energy for V_s is only 0.4 eV, and not allow for carrier separation, hence producing a low V_{oc}.[97] Experimental authors concur - there is work published of nanocrystal colloidal syntheses where the monomer precursor is believed to be FeS and incomplete conversion to FeS_2 could cause S-deficiency.[62,73] More theoretical work by the Wu group cautions that the high energy of formation calculated for V_S by Yu *et al*. could be due to the DFT method used, pointing out that oxygen vacancies have high theoretical formation energies, yet they exist easily in some metal oxides. Their calculations also find larger formation energies for S-vacancies in the bulk and that the induced defect states are located within the band gap, near the valence band. Coupling these results indicates to Hu *et al.* that the vacancies should

not produce many free carriers and should not have a large effect on the overall band structure and V_{oc}, but the Fermi level is predicted to be at the defect state energy level.[98]

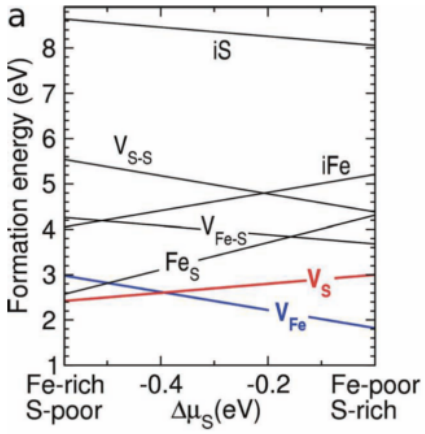

Figure 2.6. Calculated energies of formation for various defects in FeS_2 under S-poor and –rich conditions.[99]

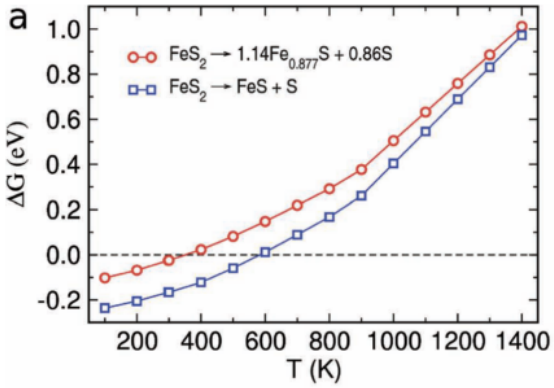

Figure 2.7. Gibbs energy of formation for the formation of FeS (squares) and $Fe_{0.877}S$ (circles) from pyrite with respect to temperature.[99]

Though Zunger's group put forth a compelling argument for the thermal phase instability of pyrite causing the S-deficiency, other researchers continued to look closely at pyrite's surface. Zhang and colleagues choose to theoretically study the (100) surface, as it should be stoichiometric. The effects of the surface are calculated to only affect the first three layers of the pyrite sample, or < 1 nm below the surface. Though it would be surprising for the carriers to be unable to tunnel through this layer, it is a possibility, and the small-gap surface layer would force a smaller V_{oc}. Additionally, Zhang *et al.* mention that there could be band bending present that

would lower the V_{oc}.[100] Krishnamoorthy *et al.* also studied the (100) surface with theoretical calculations and postulate that the reduction of symmetry at the surface causes surface states at the VBM and CBM, reducing the band gap and thus reducing the maximum possible V_{oc}.[101]

From an experimental point of view, Herbert *et al.* studied the FeS_2 (100) surface by scanning tunneling spectroscopy (STS). Aware that STS often induces band bending, the researchers measured their sample at a variety of tip separations and found that the surface E_g is approximately 0.4 eV. Using density functional theory (DFT) with simplified surface structures, they determined the reduction in band gap is caused by Fe dangling bonds forming intrinsic surface states that overlap with the CB and VB (Fig. 2.8), supporting the theoretical work by Krishnamoorthy *et al.* described previously. The best model fit for their data required the addition of mid-gap surface states from S- and Fe-vacancies at 12.5% surface coverage each, which act to pin the Fermi level.[102] Experiments by the Law group did not separate out a small surface band gap, but found that overall the band gap was a smaller (~0.8 eV) and with a softer edge in their thin films formed from an annealed solution precursor than that found in chemical vaport transport (CVT) grown crystals. Most significantly, regardless of composition or fabrication method, they observed the same electrical properties: high conductivity, low mobility, highly doped non-degenerate p-type transport. This indicated to the authors that there was a single type of impurity or surface effect that controlled transport in pyrite in general. They suggest the best explanation for this behavior is a hole accumulation or inversion layer on the surface.[103]

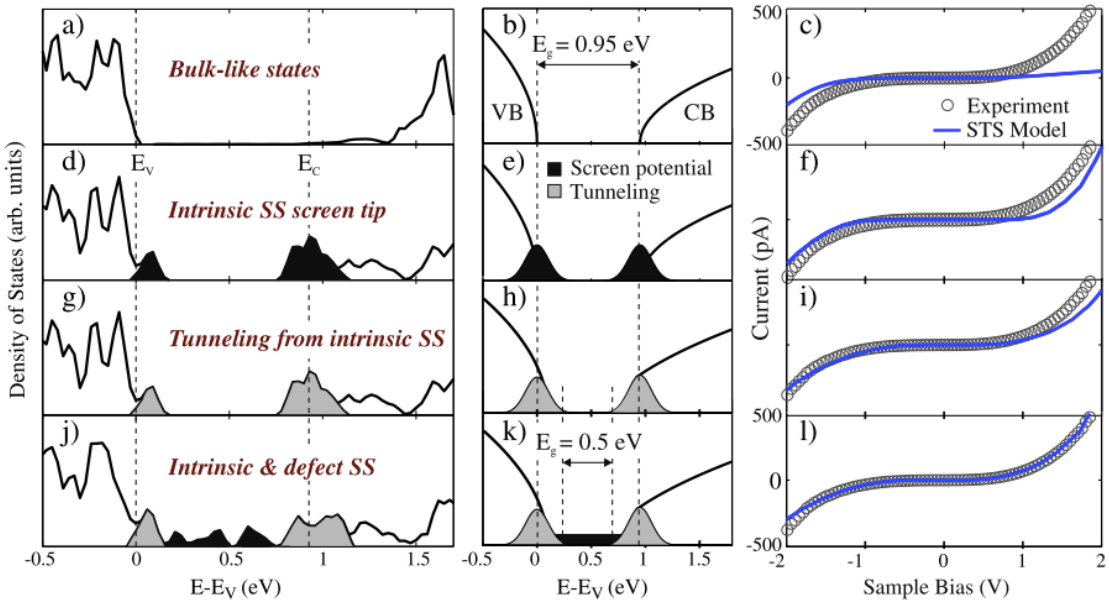

Figure 2.8: density of states, simplified DOS, and modeling fit to experiment. See Herbert *et al.* for more details.[102]

This conclusion was actually suggested two decades earlier by Bronold *et al.* after surface photovoltage (SPV) measurements on FeS_2 (100) indicated a mid-band gap defect level from Fe 3*d* states due to S-vacancies.[104] Electrons could tunnel through the resulting ~0.2 nm surface barrier directly or with assistance from the defect states, with both options contributing to the observed low V_{oc} (Fig. 2.9). The Law group followed up their first study with one using high-purity single crystals to experimentally show that there does, indeed, exist a thin p-type inversion layer at the surface of n-type bulk pyrite, though they do not explicitly tie it to any particular defect, only citing that passivation of surface states and subsurface defects should be able to minimize the inversion layer.[43] Their key experimental finding was that a *p*-type/*n*-type/*p*-type slab model was required to numerically fit their temperature dependent Hall measurements (Fig. 2.10, 2.11). As postulated by Bronold *et al.*, the authors offer the conclusion that the inversion layer creates a barrier that electrons can tunnel across, decreasing V_{oc} and pinning the Fermi level. The likely reason for this is the under coordinated Fe atoms, which change symmetry at the

surface.[43,104] The possibility of a low E_g surface layer on top of a larger E_g bulk, which would also explain their experimental data and low V_{oc}, is considered but ultimately not supported by either the optical measurements nor the theoretical model.

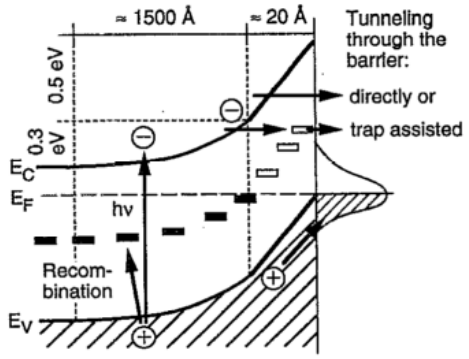

Figure 2.9. Proposed band structure with mid-gap defects due to S-vacancies from SPV mesurements by Bronold *et al.*[104]

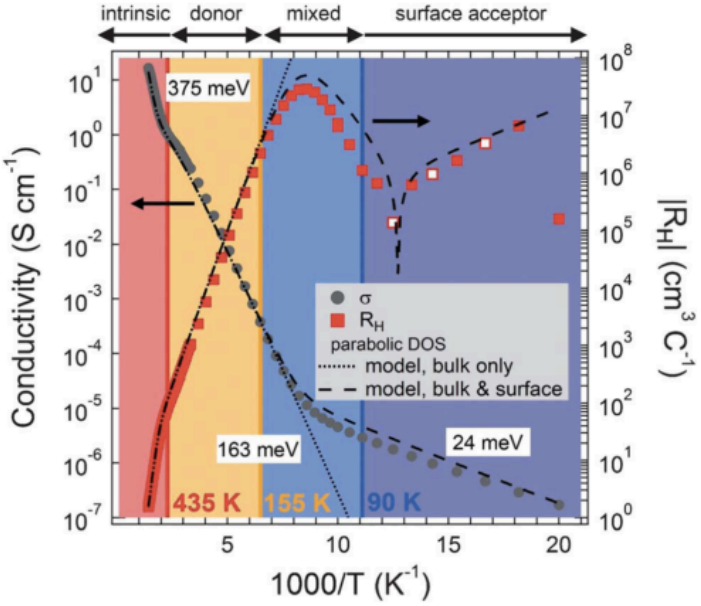

Figure 2.10. Raw Hall data of a pyrite (111) slab, plus fits. For more details see Limpinsel *et al.*[43]

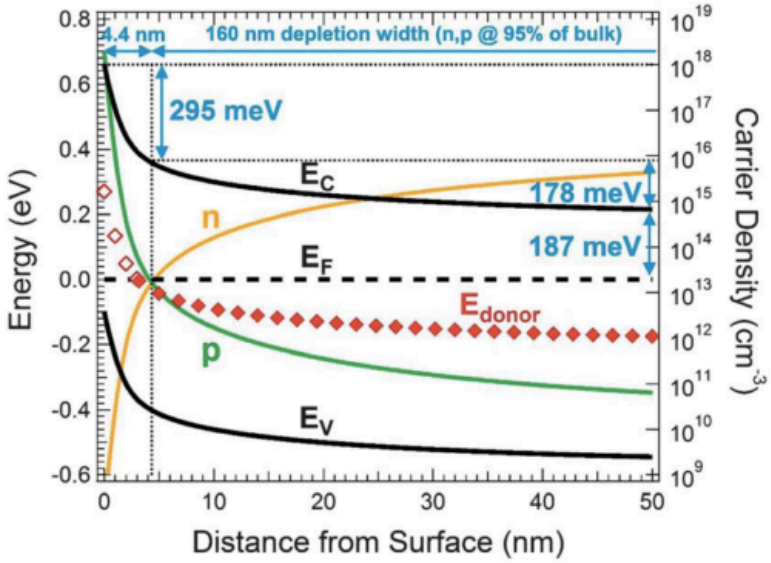

Figure 2.11. Calculated pyrite band structure at equilibrium, using values experimentally determined by Limpinsel *et al.*[43]

Shortly after the Law group published their findings of a p-type inversion layer, Song Jin's group simultaneously published two papers, one supporting the existence of an inversion layer on the surface and one arguing that the low V_{oc} is best explained by a high density of ionized deep donor states, not the inversion layer.[42,105] Using electrolyte-gated Hall measurements, Liang *et al.* plot the gate voltage (V_g) against conductance (G) and Hall coefficient (R_H) (Fig. 2.12). As the slope of G vs V_g is initially negative, it is inferred that the surface has p-type conductance. Additionally, because the slope at V=0 (the transconductance) is negative, band bending is occurring at the surface. The authors confirm that bulk pyrite is n-type by observing that R_H is negative at every gate voltage. Their calculations estimate the inversion layer is ~1.3 nm thick and that the Fermi level is pinned 150 meV below the valence band (VB) at the surface, due to the sharp band bending of ~1 eV.[105] However, the Jin group does not believe that this inversion layer at the surface is causing the consistently low V_{oc} in pyrite devices. In their other publication, by Cabán-Acevedo *et al.*, they give experimental support for

the idea that the low V_{oc} is due to high-density bulk deep donor states, which they attribute to S-vacancies in the bulk. They also show the Fermi level pinned at the valence band, but argue that this should cause the resulting barrier height, and V_{oc}, to be high. Essentially, not only is there a high density of donor defect states (~10^{20} cm^{-3}) from electrochemical impedance spectroscopy (EIS) and electrical transport analysis, the defect band is located at ~450 meV from the CB, placing it squarely in the center of the band gap and the resulting bulk Fermi level is between it and the CB. The pinned Fermi level at the VB from the surface states creates a pseudo n-p junction and cause the donor states to be constantly ionized. From temperature dependent Hall measurements, it is revealed that there is a low (10^{15} cm^{-3}) free carrier concentration with corresponding high thermal activation energy (~226 meV). Together, the defect states force the formation of a narrow space charge region where electrons can tunnel to the surface and limits the barrier height to ~230 mV (figure 2.13). This, the authors argue, is the actual cause of the low V_{oc} and therefore simply attempting to passivate the surface of FeS_2 will not result in increasing the V_{oc}.

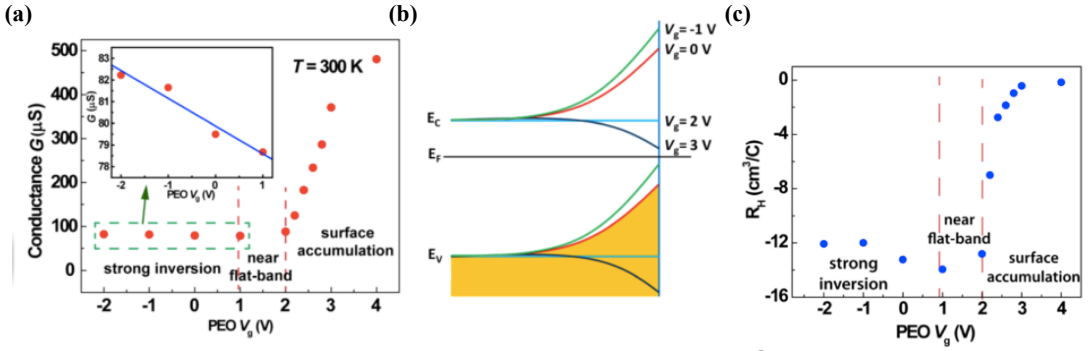

Figure 2.12. (a) Gate Voltage (V_g) vs Conductance (G), inset is magnification of G from -2 to 1 V. Slope is initially negative, specifically at V_g =0, indicating p-type conduction and (b) inherent band bending – due to high density of surface acceptor states near the valence band. (c) A plot of V_g vs Hall coefficient (R_H) reveals that the bulk of the pyrite sample is n-type.

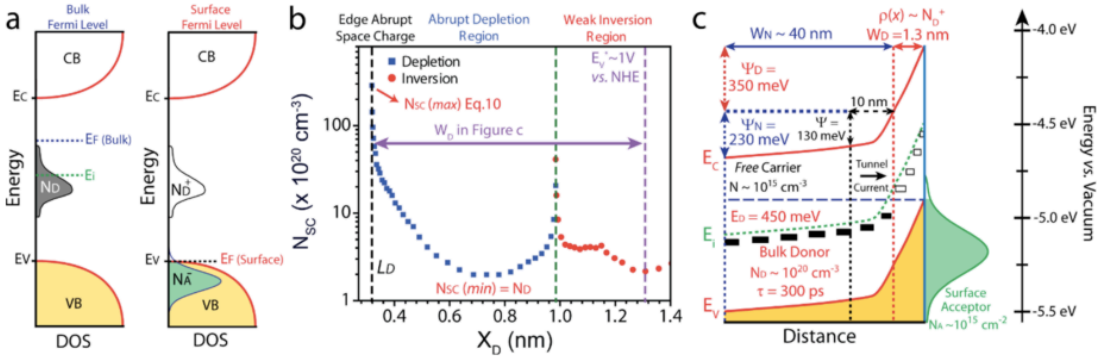

Figure 2.13: This figure, from Cabán-Acevedo *et al,* illustrates (a) how the position and occupation of defect states and Fermi level changes from the bulk to the surface of pyrite via EIS measurement and (b,c) the experimentally determined energy band scheme for a {100}-faceted FeS_2 single crystal.[42]

Though it is doubtful that passivation will solve the outstanding issues with pyrite, a few different strategies for passivation of the various defects in pyrite have been published in the literature. Etching the surface showed a minor improvement[43], but the most prominent strategy is doping with various other elements. Ni doping has shown *n*-type behavior and improves carrier mobility, but destroys photoconductivity[106] and introduces a filled deep-donor level.[41] Cobalt dopants also dope *n*-type, as well as increasing photoconductivity and Hall mobility.[41,81,107,108] Arsenic produces *p*-type material, but forms a defect state in the mid band gap area.[41,98] Zn increased E_g and photoresponse while reducing dark current;[15] Mn doping also increased E_g.[109] Cl_S or Br_S should produce *n*-type material and oxygen substitution might eliminate the mid band gap states.[98] However, doping control is challenging and there is limited experimental research in the field as to the exact nature of the band structure of the doped material. For each dopant, a deep investigation as to the defect bands and carrier concentrations, etc., similar to the one completed on pure pyrite, is needed. Doping can potentially increase cost and energy required to make the absorber material, which would offset one of the initial reasons pyrite was an attractive solar material. A detailed experimental attempt of doping has been reported by the Jin group, where FeS_2 is grown via chemical vapor deposition (CVD) on a CoS_2 substrate. They find that

beneath a layer of compact FeS_2 resides a Co-doped $FeSe_2$ layer, confirmed by XRD, Vegard's Law, and EDS analysis. The overall film displays a direct $E_g = 0.76$ eV, a work function of 5.0 eV, and ultraviolet photoelectron spectroscopy (UPS) reveals that the surface Fermi level is still pinned at the VBM. Fitting the S 2*p* peaks in the x-ray photoelectron (XPS) spectrum, the authors determine that the bulk Fermi level is dominated by a *n*-type donor state that forces the Fermi level into the conduction band, but here, unlike in pure pyrite, there is a high free carrier concentration. The authors use this conclusion to strengthen their earlier hypothesis that control of the bulk defect states is more important than surface states, at lease initially, to making pyrite work for PV.[110] Alloying with oxygen is also a promising idea, however it presents the challenge of balancing oxygen incorporation and iron oxide phase formation and segregation. Theoretical studies predict that a 10% random incorporation of O_S could increase the band gap of FeS_2 and avoid or passivate gap states, but there has yet to be any experimental work reported to support the theory.[111]

The picture pyrite presents then, is a material with inherent defects that are very challenging to overcome. Processing bulk pyrite at high temperatures, even in a S-excess atmosphere in an attempt to passivate V_S, can easily lead to the formation of S-deficient metallic phases, hurting device performance.[112] If lower temperature syntheses are pursued, such as the formation of pyrite nanocrystals and polycrystalline films, the surface defects increase in their proportional effect on the transport, plus the addition of grain boundaries makes extracting carriers even more challenging. There is also no guarantee that shrinking the domain size will help reduce S-deficiencies in the bulk lattice. Since simply doping FeS_2 has not been successful, forming a distinct ternary compound by incorporating Ge or Si in to FeS_2 to form $Fe_2(Ge/Si)S_4$ has been proposed as an alternate way to retain the positive properties of FeS_2 (high absorption

coefficient, favorable band gap), yet avoid any spontaneous phase separation into S-poor metallic phases[97] and eliminate bulk S- vacancies. Yes, like adding a dopant, this will increase cost, but forming a ternary compound can provide more control over composition and crystal structure than doping a material. There has been limited experimental work published on these ternary compounds and in the following sections work will be presented on the synthesis and characterization of Fe_2GeS_4 for photovoltaics.

Finally, though it seems that pyrite's promise for PV turned out to be a fool's promise after all, there have been attempts to use pyrite for other energy applications. These include thermal batteries[46], a catalytic or counter electrode for DSSCs[113,114], an anode material for Li-ion batteries[82], a nanowire cathode for Li-ion batteries[33], a bi-functional layer for protecting perovskite PV material from air and water vapor[115], and solar fuel production[50]. It remains to be seen if the issues highlighted here will hinder the use of FeS_2 in these other applications.

2.2 Fe_2GeS_4 for Photovoltaics

2.2.1 *Introduction*

$Fe_2(Ge/Si)S_4$ [F(G/S)S] was proposed as a photovoltaic absorber material by Yu *et al.* after a theoretical study of sulfur-deficiencies and thermal phase stabilities in FeS_2.[97] The results of these calculations can be seen in figure 2.7, which plots the calculated Gibbs Free Energy of formation energies for two different S-deficient phases, demonstrating the low temperatures needed for the non-pyrite phases to form. Alloying FeS_2 with Ge or Si to make the ternary compound was predicted to form films with increased thermal stability while not sacrificing the high absorption coefficient demonstrated by iron pyrite. This stability was demonstrated in thin films fabricated via ion sputtering of a prepared F(G/S)S pellet.[116] These experimental Ge and Si ternary films had a band gap of 1.2 and 1.4 eV, respectively (figure 2.14a), which according to

the Shockley-Queisser plot should produce cells with higher efficiencies than with iron pyrite's 0.95 eV band gap[7]. The $Fe_2(Ge/Si)S_4$ was also predicted to have a high absorption coefficient, which was a feature of FeS_2, requiring for less material to absorb 90% of the incident photons than other photovoltaic active materials like Si (Fig. 2.14b). As fabricating solar absorber materials in a scalable, colloidal manner motivates a portion of this thesis, I sought to fabricate both compounds via a solvothermal method. This chapter details how I successfully fabricated Fe_2GeS_4 with lower cost and less air sensitive precursors than previous syntheses and discusses the inherent issues with this material that will likely prevent Fe_2GeS_4 from use as a solar absorber.

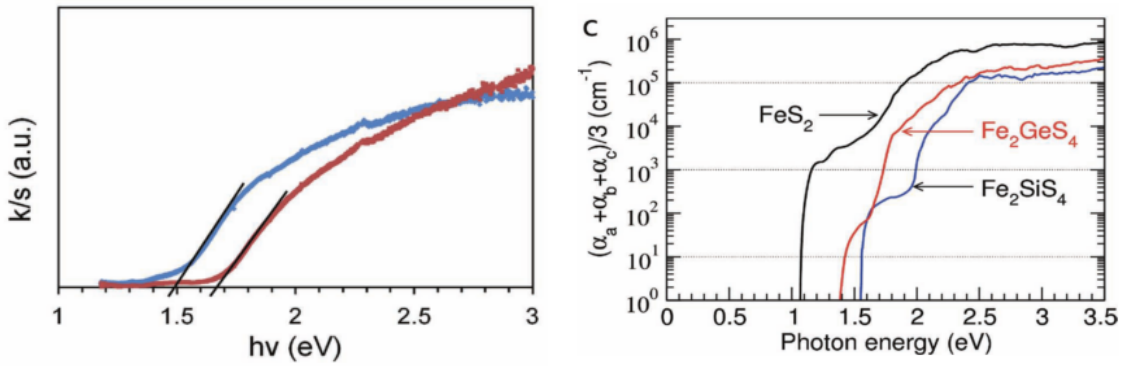

Figure 2.14. (a) Experimental band gap of FSS (blue) and FGS (red) thin films. (b) Calculated absorption coefficient of FeS_2, FSS, and FGS, prediciting >10^5 cm^{-1} absorption above 2.3 eV. Figures from Yu *et al.*[97]

2.2.2 *Results & Discussion*

Following the introduction of $Fe_2(Ge/Si)S_4$ as an alternative to iron pyrite, limited studies were completed of the material properties on sputtered thin films.[116] I first pursued synthesis of Fe_2SiS_4 by colloidal methods, but was ultimately unable to produce the material, likely due to the low reactivity of Si and its precursors. In 2013, Fredrick and Prieto (F&P) successfully developed a colloidal nanocrystal synthesis for Fe_2GeS_4.[117] However, the published reaction requires relatively long reaction times (24 hr) and expensive, air-sensitive precursor compounds

(GeI_4, Bis(trimethylsilyl) sulfide) . In searching for less expensive and air-stable precursors, I modified the synthesis in three ways: adoption of a less expensive and air-stable Ge precursor; a greener, less-smelly sulfur precursor; and a decreased reaction time. The first modification was the replacement of the GeI_4 with diaquabis(glycolato-O,O')germanium(IV) (Ge-gly). Previously, Ge-gly was successfully used in the synthesis of Cu_2GeS_3 Cu_2ZnGeS_4 nanocrystals.[118]

Using the Ge-gly in place of the GeI_4 in the F&P synthesis resulted in phase pure Fe_2GeS_4 after 24 hours at a reaction temperature of 320 ^oC (FGS-G, Fig. 2.15). Surprisingly, when the TMS-S was replaced with plain sulfur powder, FGS nanocrystals could be identified by XRD after one hour of reaction time (FGS-GS, Figure 2.15). Visually, one notices that the solution turns the expected light brown color within the hour for the S-powder synthesis, whereas it takes the full 24 hours for the TMS-S synthesis to change from black to brown. This was unexpected, as TMS-S is considered a very reactive precursor and generally S powder is first reacted with an amine before addition to the nanocrystal synthesis to increase its reactivity.[119] In this synthesis, it is thought that the sulfur powder reacts with the amine solvent or vinyl group in the octadecene (ODE) and liberates reactive H_2S gas. It is critical to remove all adventitious water from the reaction flask before adding the sulfur precursor, as products from contaminated reactions had extraneous XRD peaks present, indicating non-phase pure material. Visually, one will observe a greenish color to the reaction mixture if water is still present; time under vacuum at 120 ^oC will cause a color change to beige brown when the solution is dry. As the material has been shown to be air-sensitive, care was taken to work up the products in an inert environment with aprotic solvents.[117,120,121] The peak sharpness in the XRD is indicative of the morphologies and under TEM analysis, one observes that the FGS-G sample is composed of larger crystals with less disorder around the edges than the FGS-GS samples (Fig. 2.16). Both

syntheses produce plate-like crystals and the nanocrystals are single-crystalline, as analyzed by high-resolution transmission electron microscopy (HRTEM).

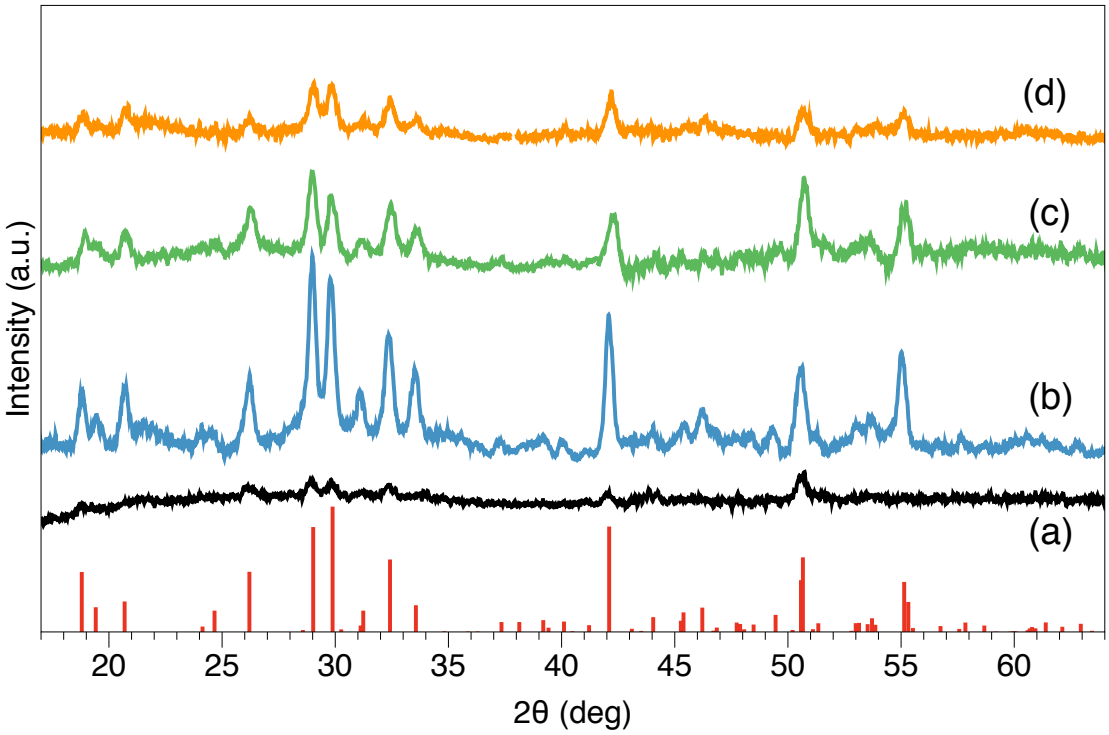

Figure 2.15. XRD spectra of products from the FGS synthesis precursor variations. Products of (a) duplication of the literature F&P synthesis, (b) using Ge-gly and TMS-S, and (c) using Ge-gly and S powder. An aliquot (d) taken at the 1 hr time mark of the same synthesis as (c) is included. The standard spectrum fro Fe_2GeS_4 is from PDF#01-073-1074.

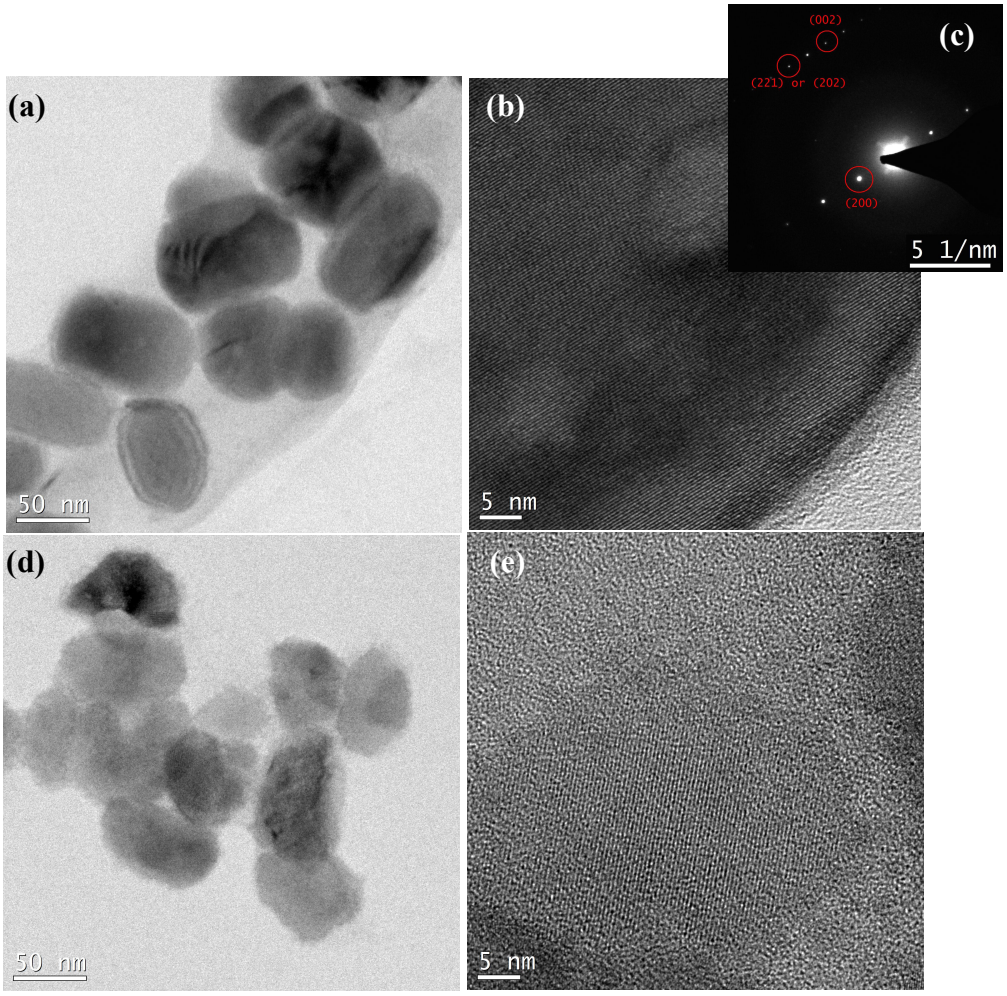

Figure 2.16. TEM images of FGS nanocrystals fabricated with (a,b) TMS-S and (d,e) sulfur powder. The electron diffraction from (b) is recorded and indexed in (c).

For the FGS-GS reactions, sulfur addition temperature was tested and was found to have a significant impact on the product. While the XRD displays little different in the structure of the products (Fig. 2.17), the UV-Vis data indicates that electronically the two products differ and TEM analysis reveals a large difference in crystal size. With sulfur addition at 120 ^{o}C, the FGS-GS nanocrystals either have a band gap too small to be detected on the UV-Vis instrument or have so many sub-band gap states that there is no clear absorption cutoff. The sample that had the S-powder addition at 160 ^{o}C had a more obvious direct band gap between 1.5 – 1.6 eV (Fig. 2.18).

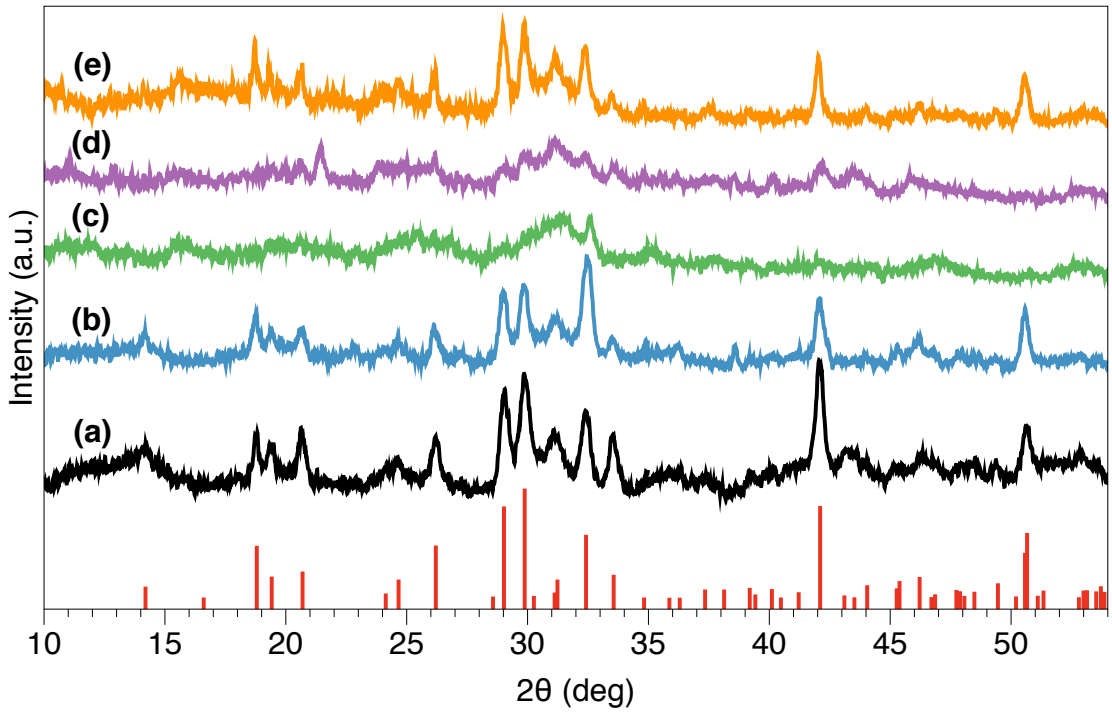

Figure 2.17. XRD of products from variations of the FGS-GS synthesis: (a) S addition at 120 °C, (b) S addition at 160 °C, (c) octadecane used in place of octadecene, (d) $FeCl_2*5H_2O$ used a Fe precursor, and (d) FGS-GS after an anneal in H_2S gas at 450 °C for 2 hours.

To determine if the band gap was direct or indirect, the absorption spectrum (A, acquired with an integrating sphere) was transformed by

$$(A*hv)^{(1/n)} \qquad \text{(eqn 2)}$$

and plotted against hv to make a Tauc plot. Fitting the linear portion of the plot when n = 0.5 indicates a direct E_g, whereas a fit when n = 2 indicates that the band gap is indirect.

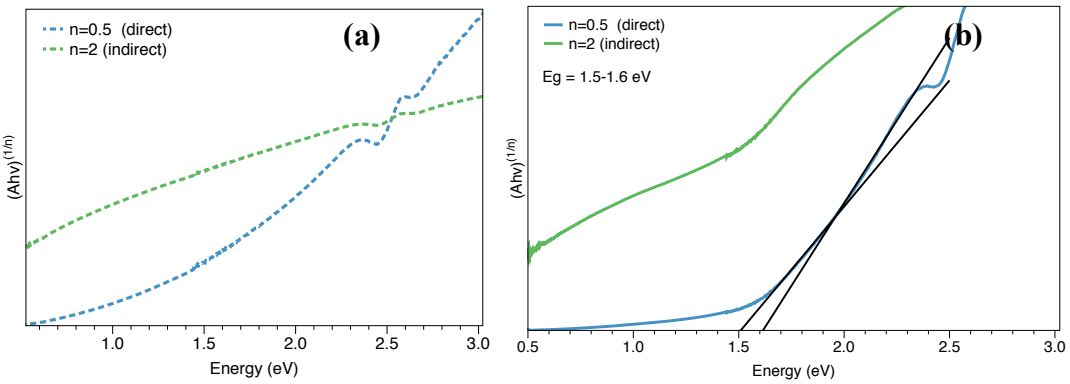

Figure 2.18. (a) Tauc plots of FGS product with sulfur addition at (a) 120 ^{o}C and (b) 160 ^{o}C. The spectrum from the 160 ^{o}C addition has been fitted in the cutoff region to determine a direct band gap between 1.5-1.6 eV.

The reason for the smaller bandgap in the 120 ^{o}C sulfur addition sample is clarified with TEM analysis. The lower addition temperature leads to significantly larger particles than the higher temperature (Fig. 2.19). The Bohr radius is not known for Fe_2GeS_4, but if it is on the larger end (>100 nm), then the smaller size nanocrystals are expected to have a larger bandgap. However, this a tentative rationale for the difference in bandgap, as thin films of FGS with large grain sizes have demonstrated a bandgap in 1.2 eV range. In the larger crystals, one observes distortions in the plane, which could contribute to that sample's lack of visible band gap by introducing mid-gap defect states (Fig. 2.19a).

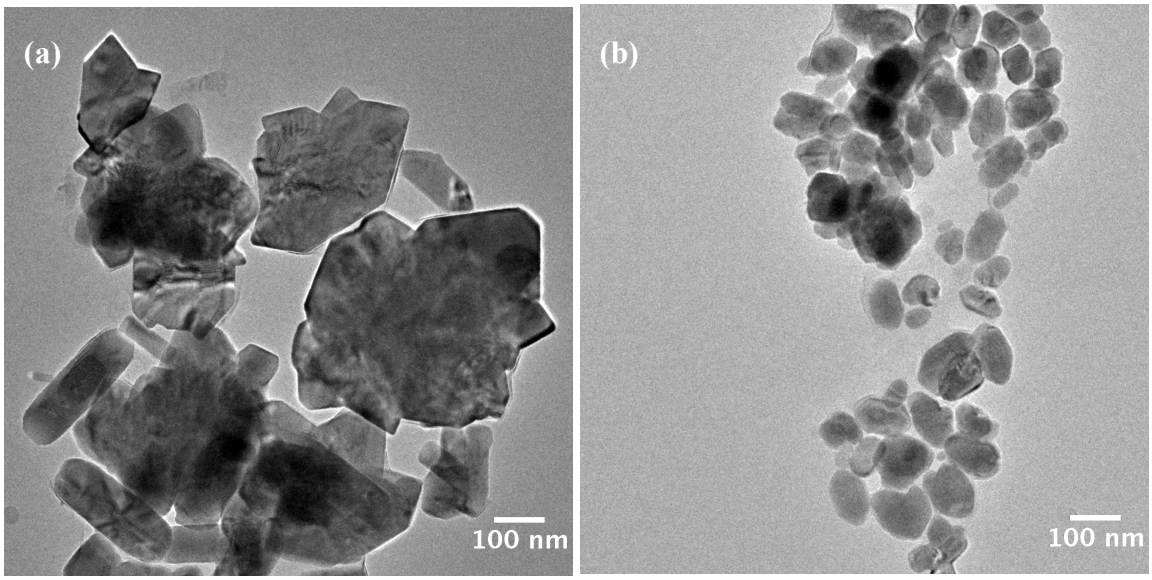

Figure 2.19. Transmission electron micrographs of FGS-GS crystals from the synthesis with (a) 120 ^{o}C or (b) 160 ^{o}C sulfur powder addition.

Additionally, I tested the necessity of the vinyl bond present in the octadecene and found that the double bond in ODE was required for a successful reaction with the sulfur powder precursor. If octadecane was used instead of ODE in the reaction, no FGS products were identified with XRD (Fig. 2.17c). The double bond in ODE must react with the cyclic sulfur powder, converting the sulfur into a more reactive state.[122] Amines reduce sulfur powder, so the lack of FGS product indicates that the ODE is not just a non-coordinating solvent in this reaction, but that the reduction of sulfur by ODE is critical to making FGS.

In an effort to make this reaction even more air-friendly, I attempted to use the hydrated form of $FeCl_2$, which is stable when stored in ambient conditions, instead of the anhydrous version. While the sample size is a n = 1, it appears that even an extended time under vacuum (~60 min) after $FeCl_2$*$5H_2O$ addition is not sufficient to rid the reaction of water. XRD analysis of the product of this reaction included some FGS peaks, but it was not phase pure (Fig. 2.17d). Contrary to the published and expected thermal stability for Fe_2GeS_4, the nanocrystal FGS decomposed at low temperatures (Fig. 2.18) in an inert atmosphere. XRD analysis reveals that,

additionally, the FGS NCs decompose before they experience any grain growth, which is somewhat unusual in the nanocrystal thin film literature. The germanium was the first element to leave the material with annealing (EDS), and, unexpectedly, the FGS decomposed into what appears to be phase-pure FeS_2 by XRD and Raman spectroscopy (Fig. 2.19, 2.20). Notably, this iron pyrite exists above annealing temperatures that were previously demonstrated to cause decomposition of the FeS_2 material (Fig. 2.2). Though there is no 'standard' FGS Raman spectra, the only other published spectrum matches that of the nanocrystals synthesized here.[121] The spectrum features an intense peak at ~350 cm^{-1} with a few weak peaks on either side. Fe_2GeS_4 is described by the orthorhombic space group *Pnma* with the point group symmetry of D^{16}_{2h}. The D_{2h} character table indicates that there should be four fundamentally active Raman modes: A_g, B_{1g}, B_{2g}, B_{3g}.[123] There has been no attempt in the literature to theoretically calculate Raman shifts and intensities for this material. Raman is more surface sensitive than XRD and it appears that the surface of the FGS crystals begin to decompose to FeS_2 at 450 ^oC.

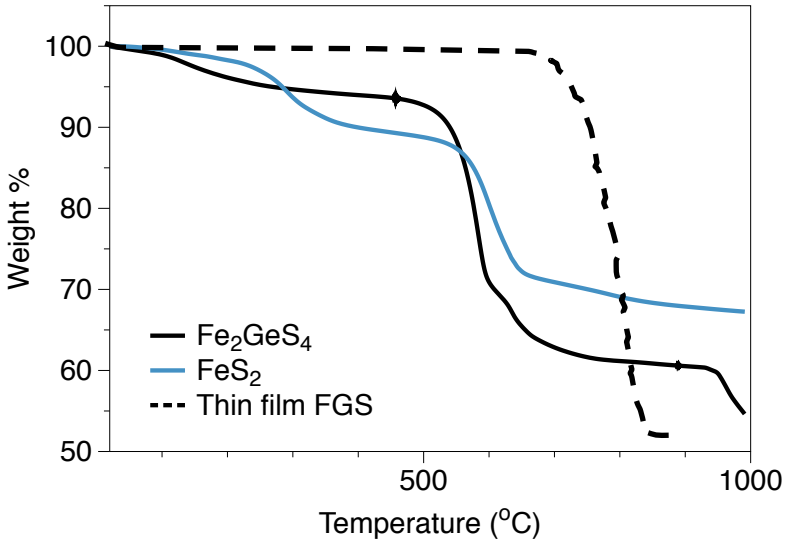

Figure 2.18. Thermogravimetric analysis of Fe_2GeS_4 and FeS_2 nanocrystal samples synthesized by the author. For comparison, a duplicate of a published experimental TGA trace of a Fe_2GeS_4 thin film has been included.[116]

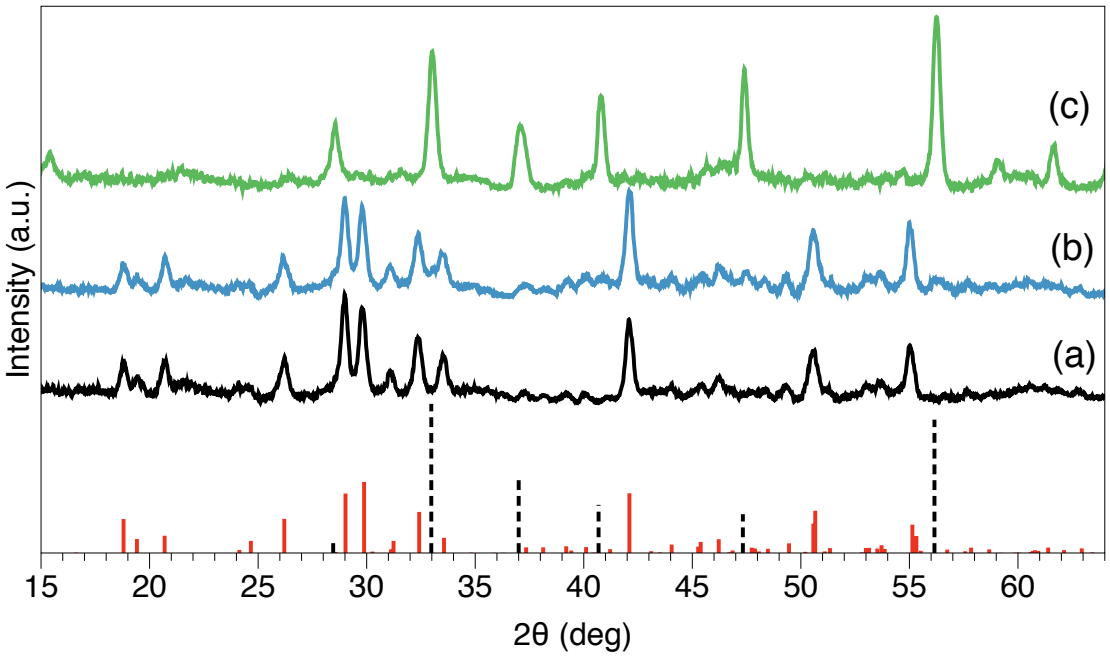

Figure 2.19. XRD spectra of (a) FGS heated under Ar to (b) 450 °C and (c) 550 °C. One observes the phase transformation from FGS to FeS_2 at 550 °C. Solid lines are the FGS standard PDF#01-073-1074 and dashed lines are the FeS_2 standard PDF#01-071-0053.

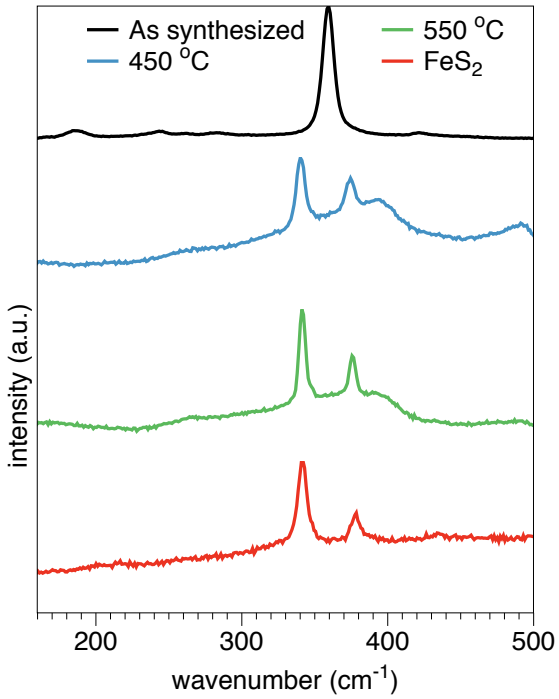

Figure 2.20. Raman spectroscopy of FGS annealed in Ar at the specified temperatures and of an experimental FeS_2 nanocrystal sample, demonstrating FGS transformation to FeS_2 at even lower temperatures on the surface of the sample.

To further investigate the electronic structure of Fe_2GeS_4, a sample of FGS-GS underwent XPS and UPS analysis. Though care was taken during synthesis and work up to keep the sample air-free, the sample was exposed to ambient air when transferred to the UPS instrument. The as-synthesized nanomaterials are covered in hexadecylamine capping ligands and their presence is reflected in the UPS spectra by the appearance of a large distance between E_F at 0 eV and where the data significantly takes off around -4 eV (Fig. 2.21, black traces). The cross-section of C and N are larger than Fe, Ge, or S when probed with He(I) photons, meaning that that the ligands have an outsized contribution to the UPS spectra, potentially obscuring the real VBM of the material. In an effort to remove the ligand contribution, I removed the ligands with an annealing treatment, using the TGA trace as a guide. At 400 ^oC under an inert atmosphere (Ar), the ligands should be removed from the sample. This is confirmed by FTIR in Fig. 2.22.

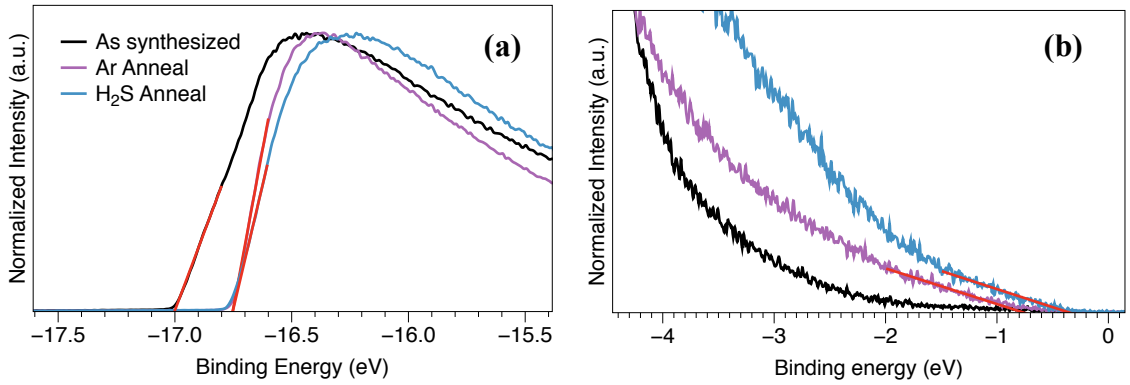

Figure 2.21. UPS spectra of (black) as synthesized, (purple) Ar annealed, and (blue) H_2S annealed FGS-GS samples. Plots are of the (a) workfunction region and the (b) VBM region are shown with fit lines to determine the values discussed in the text.

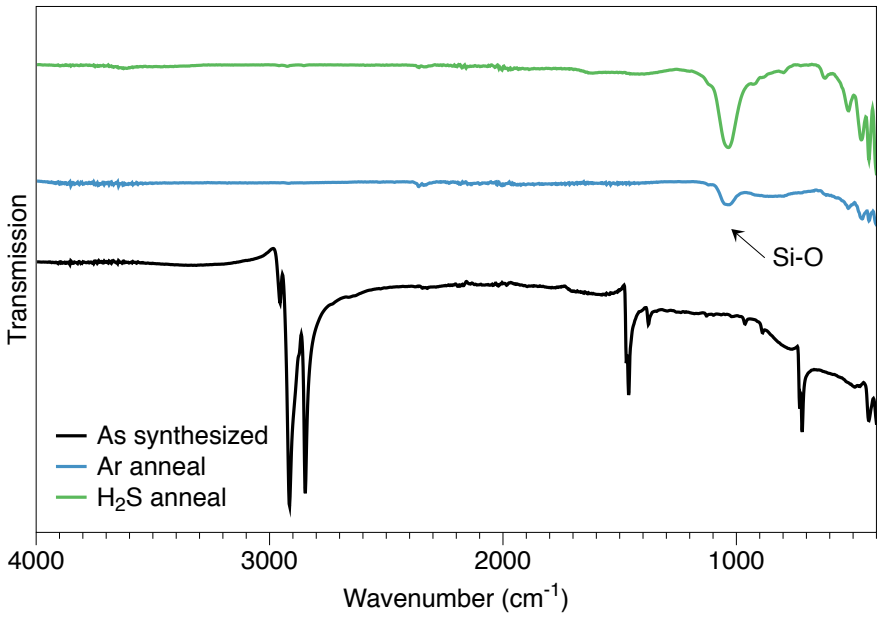

Figure 2.22. FTIR transmission spectroscopy of FGS material as synthesized, after Ar anneal, and after H_2S anneal. The annealed samples were on a Si-O substrate and that peak is identified in the plot.

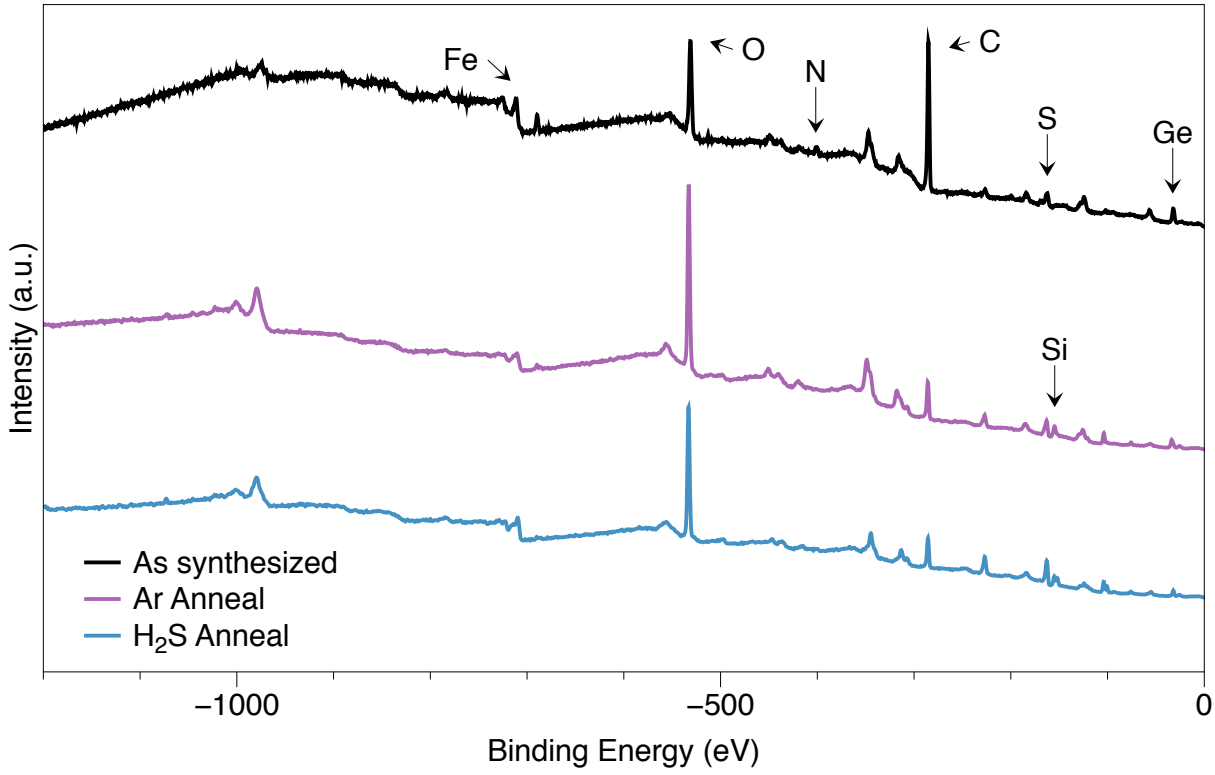

Figure 2.23. Low-resolution XPS survey scans for the (a) as synthesized, (b) Ar annealed, and (c) H_2S treated FGS-GS samples.

A close look at the composition of the nanocrystals by EDS (Fig. 2.22) revealed that generally, as synthesized FGS was sulfur deficient. Annealing the material under Ar with a boat of S powder upstream did not affect the composition but a H_2S anneal effectively eliminated the sulfur deficiencies. The H_2S treatment included annealing a sample at 425 ^oC under Ar + H_2S gas (generated *in situ*, see methods section). This temperature was selected because the only published Fe_2GeS_4 synthesis in the literature that saw photoluminescence (PL) from the material required a similar anneal.[121]

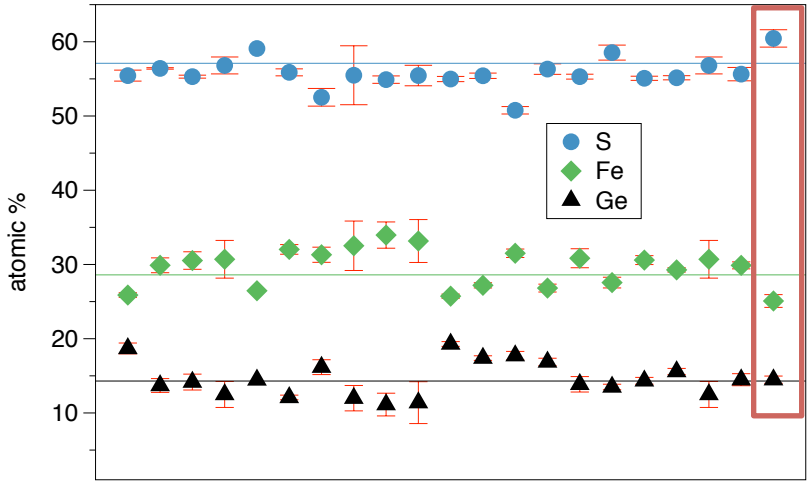

Figure 2.24 Compilation of composition of FGS products by EDS, showing S-poor products on average. A box is drawn around the sample annealed under H_2S gas.

UPS analysis of the H_2S annealed sample appeared to reveal a much smaller VBM-E_F difference where the E_F was located within the bandgap (Fig. 2.21, green traces). The post-H_2S-anneal sample demonstrates a band gap of ~1.1-1.3 eV, a workfunction of 5.457 eV, and a VBM-E_F distance of 0.34775 eV. These values place the Fermi level within the band gap and the material is *p*-type. XPS analysis of a sample annealed under Ar at 400 ^oC does show a similar, but not identical spectra as that of a sample treated with H_2S. In this sample, the V_S still exist and are mostly likely the reason that the E_F is further from the VBM (~0.759 eV) than in the H_2S sample, making it more *n*-type. However, the experimental apparatus available at this time

always requires two points of exposure to ambient air and, as it has been noted in the literature that FGS is easily oxidized, so this discussion of UPS data must bear in mind possible oxygen surface contamination.[117] High resolution analysis of the Fermi region by XPS might give some additional insight, but it was not undertaken for this report due to time constraints.

Thus, the appearance of photoluminescence emission from the FGS material after H_2S treatment (Fig. 2.25) is most likely due to elimination of S-vacancy induced trap state(s) that were present in the as-synthesized material. It is worth noting that the equivalent of ~78 suns incident light was required to generate any appreciable PL. From the PL response, the bandgap is estimated to be 1.4 eV. Insight as to the trap states present and/or eliminated with the H_2S treatment could be gained through transient absorption spectroscopy.

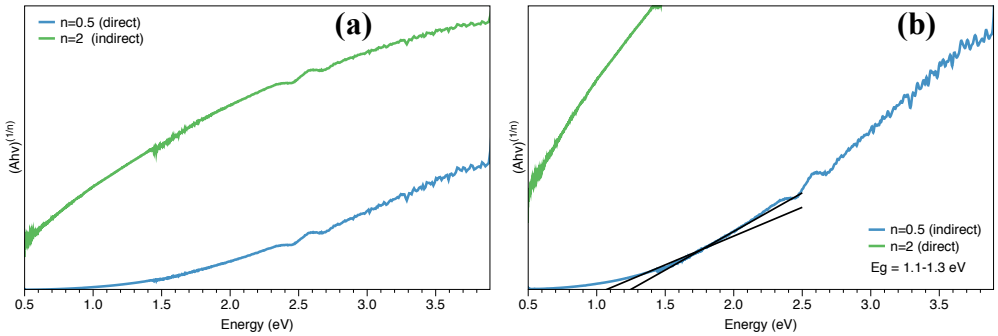

Figure 2.24. (a) Tauc plots derived from the UV-Vis absorption of the FGS post-H_2S-anneal, (b) displays the lines used to estimate the bandgap.

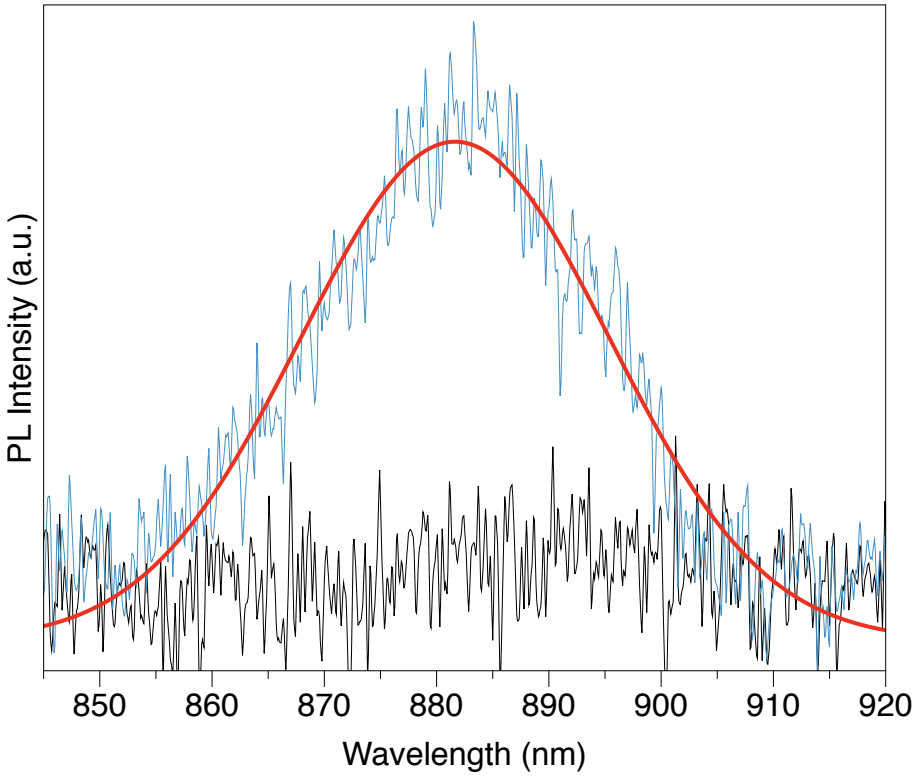

Figure 2.25. PL emission spectra from the (black) as synthesized and (blue) H_2S annealed samples.

Unfortunately, the FGS NCs were not colloidally stable for any significant length of time in any solvent, so before any thin films were fabricated, the suspension was sonicated briefly. Fabricating thin films from any synthesis, including F&P, had limited success. Occasionally a solution would dropcast well or be stable enough for dipcoating, but good NC suspensions were rare. This is likely due to the large size of the nanocrystals. To aid electron transport through a FGS nanocrystal film, some were treated with a ligand exchange procedure; most commonly the film was dipped into a solution of 1,2-ethanedithiol in acetonitrile in an effort to exchange the long-chain insulating amine ligands remaining after synthesis with the shorter thiol-terminated ligands. This strategy has been successfully applied in the past with other semiconducting nanocrystal materials; however, regardless of the rigorous air-free nature of the ligand exchange, or any subsequent thermal annealing under Ar, the FGS thin films did not experience a

measureable decrease in resistivity.[61,124,125] After a dropcast film of FGS-GS was annealed under H_2S, the sheet resistance did decrease from overloading the multimeter to approximately 45 MΩ/sq. More rigorous four-point probe and thickness measurements are needed to provide accurate resistivity measurements and to determine the carrier mobilities, but it is noted that the initial measurement is more than three orders of magnitude greater than reported values for other semiconductors.[126–128]

2.2.3 *Conclusions*

Fe_2GeS_4 nanocrystals of varying sizes can be produced by a colloidal synthesis method using less expensive and air-stable Ge and S precursors. Additionally, the use of sulfur powder as a precursor enables the reaction time to be significantly shorted from 24 hr to 1 hr. Thermal analysis reveals these nanocrystals are not as thermally stable as a sputtered thin film and elemental analysis indicates that they are sulfur-deficient as synthesized. This deficiency raises the Fermi level of the material in comparison to a non-sulfur-deficient sample due to the excess electrons required for charge balance in the material. It is likely that the V_S creates trap states within the bandgap of the FGS material and that with an anneal under H_2S gas, the V_S reduction allowed for weak PL emission. Overall, the challenges in consistently fabricating a uniform film with good transport, PL, and thermal stability do not make FGS nanocrystals very attractive as a solar absorber material.

2.2.4 *Experimental Details*

2.2.4.1 Synthesis of diaquabis(glycolato-O,O')germanium(IV)

The synthesis of the Ge-gly followed a published procedure by Chesman *et al.*[118] 3.0 g glycolic acid (TCI America) was combined with 1.0 g GeO_2 (Sigma Aldrich) in a round bottom

flask containing 100 mL deionized H_2O and brought to reflux, with stirring, for 3 hours. After refluxing, the solution was cooled, the water rotovapped off and the resulting white powder dried under vacuum overnight.

2.2.4.2 Fe_2GeS_4 NC synthesis with Ge-gly precursor (*FGS-G*)

0.1038 g (0.42 mmol) of $[Ge(gly)_2(H_2O)_2]$ and 2.0 g of hexadecylamine (Sigma Aldrich, 90%) are stirred under low vacuum at 155 ^oC for 30 minutes to complex the Ge precursor with the amine and drive off any H_2O ligands. 2 mL of octadecene (technical grade, ODE) is injected, the flask filled with Ar, and cooled to 80 ^oC. At this temperature 0.063 g of $FeCl_2$ (0.5 mmol) is added to the flask under flowing Ar and the temperature is set to 120 ^oC. At 120 ^oC, the flask is exposed to vacuum for 10 minutes to pull off any remaining water vapor. If there is water remaining in the flask, the color of the solution will be green. When all the water is removed the solution will be a beige orange color. The temperature is then set to 320 ^oC and at 160 ^oC, a solution containing 1 mL hexamethyldisilanze (TCI America, HMDS), 1 mL ODE, and 0.45 mL bis-trimethylsilalsulfide (Sigma Aldrich, TMS-S, 2 mmol) is injected. The reaction is held at 320 ^oC for 1-24 hours. When reaction time has elapsed, the flask is cooled to 80 ^oC and injected with ~8 mL of toluene. If working up in a glovebox, cannula transfer to a Schlenk flask and washed via centrifugation with ethyl acetate/toluene three times.

2.2.4.3 Fe_2GeS_4 NC synthesis with Ge-gly and Sulfur powder (*FGS-GS*)

Same as synthesis for FGS-G, but instead of the HMDS/TMS-S/ODE injection solution, sulfur power (0.038g, 1.2 mmol) is added at 160 ^oC. Additionally, when ODE is injected, the volume injected is increased to 4 mL.

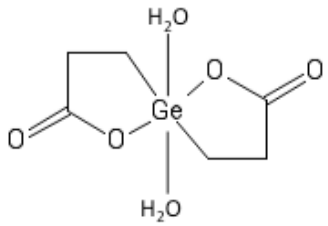

Figure 2.26. Diaquabis(glycolato-O,O')germanium(IV) compound

2.2.4.4 H_2S anneal

Samples were annealed under H_2S generated from a 1:2 mixture of sulfur powder:eicosane (icosane) mixed in a round bottom flask under Ar at 180 ^oC. Paraffin wax can also be used instead of eicosane. The Ar/H_2S was passed through a tube furnace at room temperature containing the samples. After H_2S generation was confirmed, then the furnace was elevated to the specified temperature and held for the specified time. The exhaust from the tube furnace was piped into a flask containing a $CuSO_4$ solution and then a flask containing a solution of NaOH. One can observe the precipitation of CuS_2 (black) in the $CuSO_4$ (blue) solution to confirm the generation of H_2S gas.

2.2.4.5 Characterization

Scanning electron microscope (SEM) images were acquired with a FEI XL830 dual beam instrument with integrated electron dispersive X-ray spectrometer (EDS) by Oxford. Typical operating conditions were 5 keV electron beam for SEM and 20 keV for EDS. Powder X-ray diffraction patterns (XRD) were taken with a Bruker D8 Discover with GADDS 2-D XRD using Cu Kα radiation. The background fluorescence was manually subtracted from the resulting diffraction patterns. X-ray photoelectron spectroscopy (XPS) and ultraviolet photoelectron spectroscopy (UPS) was performed under high vacuum conditions in a Kratos AXIS Ultra instrument; samples were prepared by dropcasting the nanocrystals from an organic suspension on to a clean piece of Si or Ti, typically within a glovebox. Once on the substrate, samples were

treated by annealing in H_2S or chemical stripping as mentioned in the text and quickly transferred to the instrument chamber to minimize oxidation in air. Samples were exposed to air during transfer to and from the furnace but stored in a glovebox until analysis. An Al Kα source was used for XPS and He(I) for UPS. UPS spectra were referenced to an Au sample. A TA Q50 thermogravimetric analyzer (TGA) under N_2 atmosphere was also used for characterization. UV-Vis spectra were acquired with a dual beam Perkin Elmer Lambda 1050 Spectrometer with an integrating sphere attachment; samples were dropcasted on to glass slides for measurement. TEM images were recorded under bright field condition on a FEI Tecnai G2 F-20 instrument. TEM samples were prepared by dropping ~ 10 μL of a very dilute solution of nanocrystals in hexanes on to copper grids covered with carbon film. A Horiba LabRam confocal steady-state photoluminescence instrument recorded photoluminescence responses. It was calibrated with a NIST-calibrated blackbody and a 785 nm laser at ~78 suns intensity was used to excite the sample. Raman spectra were collected by a confocal Horiba instrument with 514 nm incident light. Samples were dropcasted on to glass slides for measurement and carefully monitored for changes due to local heating by the laser.

Chapter 3. WSe_2 FOR PHOTOVOLTAICS

3.1 INTRODUCTION

As early as 1968, WSe_2 was recognized as a potential absorber material for photovoltaic energy conversion, however there was a large break in the published literature between the late 1980's and recent years.[129] While the reason for this break is unclear, the recent surge of interest in WSe_2 can be tied to the increased research of thin film PV and 2D materials, the ability of the MX_2 (M = Mo/W, X = S/Se) material to exist in monolayer form, and the chemically inert van der Waals planes holding each layer together.[130–132] WSe_2 has been utilized in a high performing photoelectrochemical cell (eff = 17%), but solid state heterojunction cells have seen limited success, with the best performing cell produced in 1989 with an efficiency of 8.38%.[133] Furthermore, many of the WSe_2 samples in the literature are fabricated via energy- and time-intensive vapor transport methods.[131,134–139] These samples are generally p-type and show bandgap measurements of 1.15-1.5 eV, mobilities on the scale of 10-10^2 cm^2 V^{-1} s^{-1}, and carrier concentrations in the range of 10^{16} cm^{-3}. This thesis has interest in scalable colloidal synthesis of photovoltaic materials, and while there have been a number of recently published solution-based approaches, electronic characterization and device applications are limited.[140–144] While there is no fundamental reason that the projected Shockley-Queisser efficiency of 30-33 % cannot be achieved, there are a number of material properties that must be considered and engineered around for a successful solid state cell.

First, WSe_2, as well as WS_2 and the Mo analogs, exists in two polytypes: trigonal prismatic (2H) and octahedral (1T) (Fig. 3.1). The 2H configuration is the thermodynamically preferred structure and thus is more commonly found in nature, so for papers that do not remark

on the polytype of their samples, I have assumed the samples are in the 2H polytype. The difference between these two polytypes is critical, as the 2H conformation demonstrates semiconducting properties, but the 1T form is metallic.[145,146]

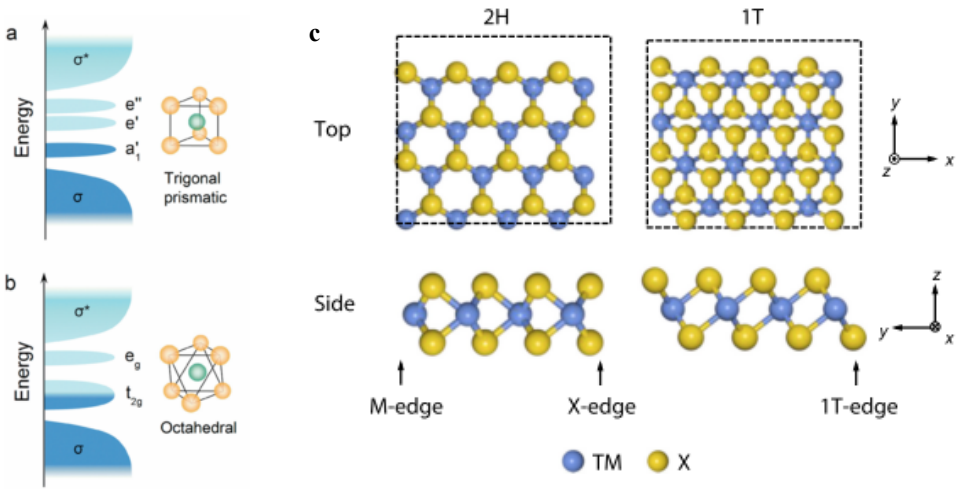

Figure 3.1 Illustrations from literature of (a,b) metal coordination & band diagram, and (c) unit cell for generic 2H and 1T MX_2 structures.[145,146]

It is very difficult to separate the two phases via XRD, especially since few synthetic materials prove to be wholly composed of a single polytype. Some authors have elected to use TEM or Raman to determine polytype, but XPS is an accessible and generally unambiguous method for calculating 2H and 1T proportions.[140,145,147–151] For WSe_2, high resolution scans of the W 4f binding energy can yield up to 3 peak pairs: peaks appearing at ~ -34 and -32 eV can be attributed to the 1T phase, where as the pair at ~ -35 and -33 eV is the 2H binding energy (Fig. 3.2a).[149] The oxide peaks are lower in energy than the peaks for 2H. With annealing, the 2H proportion has been shown to increase in a sample (Fig. 3.3).[145] If a WSe_2 sample contains some 1T polytype, charges generated by incoming photons will quickly recombine, rendering the material useless for PV applications. In an effort to avoid this issue, the material described in this chapter was heated at an elevated temperature for 100 hours during synthesis, creating fully 2H-polytype samples via XPS (Figure 3.2b).

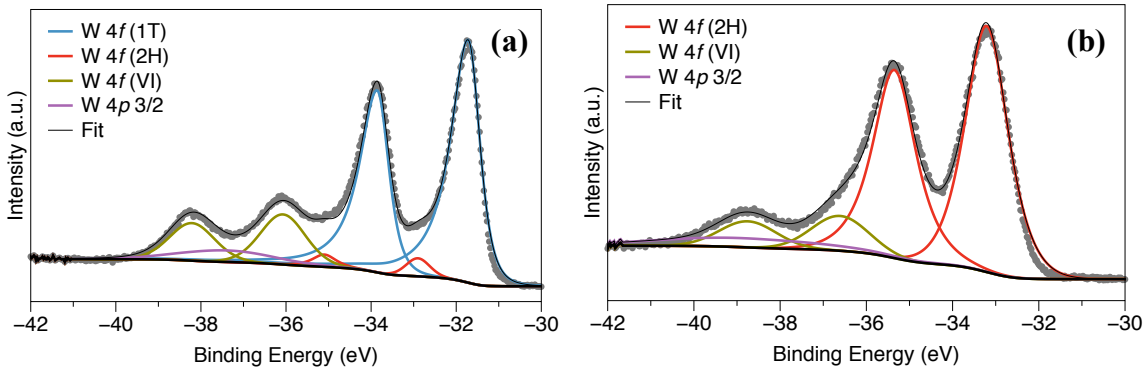

Figure 3.2. XPS of WSe_2 nanocrystals produced by (a) Antunez method and (b) Duphil method, demonstrating the control over the 2H and 1T polytypes with colloidal synthesis.

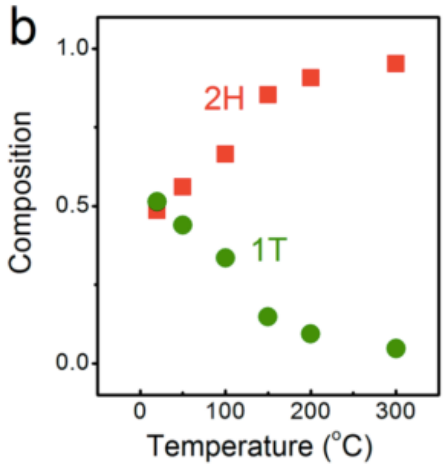

Figure 3.3. Composition of polytype vs temperature for MX_2 materials.[145]

A second challenge with utilizing WSe_2 for solid-state photovoltaics is the highly anisotropic transport through the material. WSe_2 forms stacks of Se-W-Se units (Fig. 3.1), with each sheet interacting with the next via van der Waal's interactions. Naturally, WSe_2 forms hexagonal platelets on the macroscale. With this morphology, electronic carriers move much more easily perpendicular to the c-axis ($c\perp$, along the sheet) than parallel ($c_{||}$, between the sheets). Generally only the $c\perp$ values are reported, but when both have been measured, resistivity ratios ($\rho_{||}/\rho\perp$) on the order of 10^4 Ωm.[138,152] This anisotropy means that $c_{||}$ carrier mobilities are limiting in a traditional solar cell device configuration when the WSe_2 sheets lay with the c-axis normal

to the substrate. Non-traditional devices made from a monolayer absorber or an organic bulk heterojuction could be a way to engineer around the carrier anisotropy and utilize the fast charge movement along c⊥. This is perhaps why WSe_2 has demonstrated good photoelectrochemical (PEC) cell performance but dismal solid-state performance. In a PEC cell, the liquid redox couple can be in contact with the edges of the material and not just the basal plane, capturing the carriers that move perpendicular to the c-axis.

The third major challenge for using WSe_2 in a solar device can be found at the edges of each sheet. While the Se atoms in the basal plane are fully satisfied, the dangling bonds found at the edges act as recombination sites. Passivating these dangling bonds has been more explored in PEC applications than in solid-state devices and it has been observed that passivation with iodine greatly increases the efficiency of PECs. Generally this passivation is achieved through photoetching the material in acid or an iodine solution (KI or NaI/I_2), annealing under an I_2 atmosphere, or adding an organic polymer.[153–164] As expected, even with passivation, single crystalline WSe_2 PEC cells demonstrated higher conversion efficiencies than polycrystalline absorbers.[165] It should be mentioned that the fully saturated basal planes make WSe_2 even more attractive for PEC devices, as they are chemically inert and provide great stability against corrosion.

A fourth challenge for WSe_2 solid-state photovoltaics is the observation that the semiconducting form has both an indirect and direct bandgap in close proximity. This manifests itself in a conversion from a direct bandgap to an indirect one when more than one layer of material is present. Photoluminescence decreases four-fold between 1 and ~24 layers (20 nm), making all but the thinnest films impractical for efficient devices.[166–168] Additionally, mono- and

few-layer WSe_2 samples are difficult to produce, usually requiring exacting CVD conditions or a Li intercalation process.

3.2 Results and Discussion

With these challenges in mind, we can now discuss how I approached developing WSe_2 for a solid state PV cell. To overcome the 2H/1T polytype co-existence, I selected a synthesis that would include enough time at an elevated temperature for the material to come to the thermodynamically preferred 2H type. In this case, I utilized a synthesis by Duphil *et al.* where the WSe_2 powder formed over the course of 100 hours.[141] This extended time was required for the full decomposition of the $W(CO)_6$ precursor but was also critical for obtaining all 2H WSe_2 (Fig 3.2b). As described in the next chapter, generally solution syntheses of WSe_2 demonstrate majority 1T until sufficient reaction time has passed. By EDS, the WSe_2 material is Se-heavy until it is annealed (Fig 3.4). Raman and XRD indicate that the material is WSe_2 by matching the major peak locations with that found across the literature (Fig. 3.5).[169,170] Due to the small crystallite size, the Raman peak at ~ 250 cm^{-1}, which is composed of both the E_{1g} and A_{1g} peaks, is broad.[171,172] UPS analysis of the as synthesized product revealed a workfunction of 5.522 eV and that the valence band maximum is 0.697 eV below the Fermi level (Fig. 3.6). With a band gap (via UV-Vis) of ~0.75 eV, which is smaller than expected, this material can be considered n-type (Fig. 3.7).

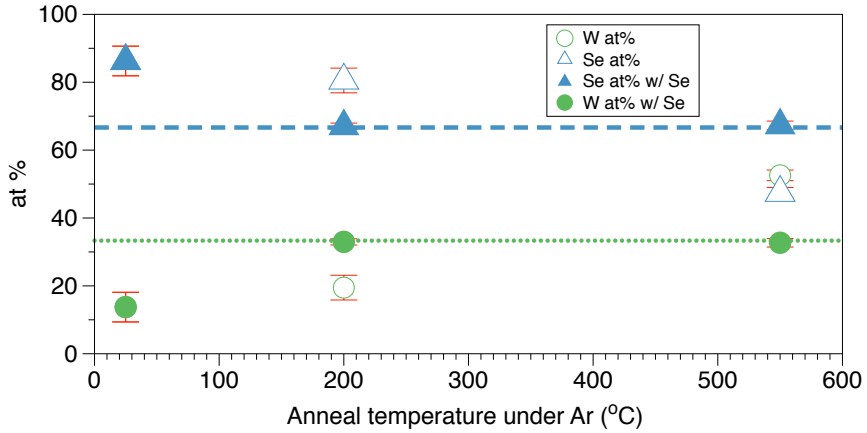

Figure 3.4. Composition via EDS for films annealed under (open shapes) Ar only and (filled shapes) Ar and Se powder. The films annealed without Se powder become Se-deficient by 550 °C.

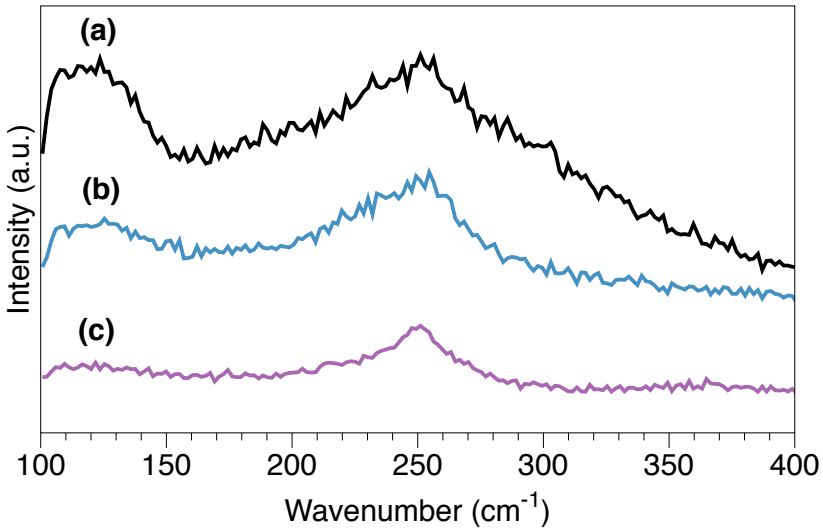

Figure 3.5. Raman spectra from WSe_2 samples (a) as synthesized, (b) BOAI-exchanged, and (c) BOAI-exchanged and annealed at 400 °C.

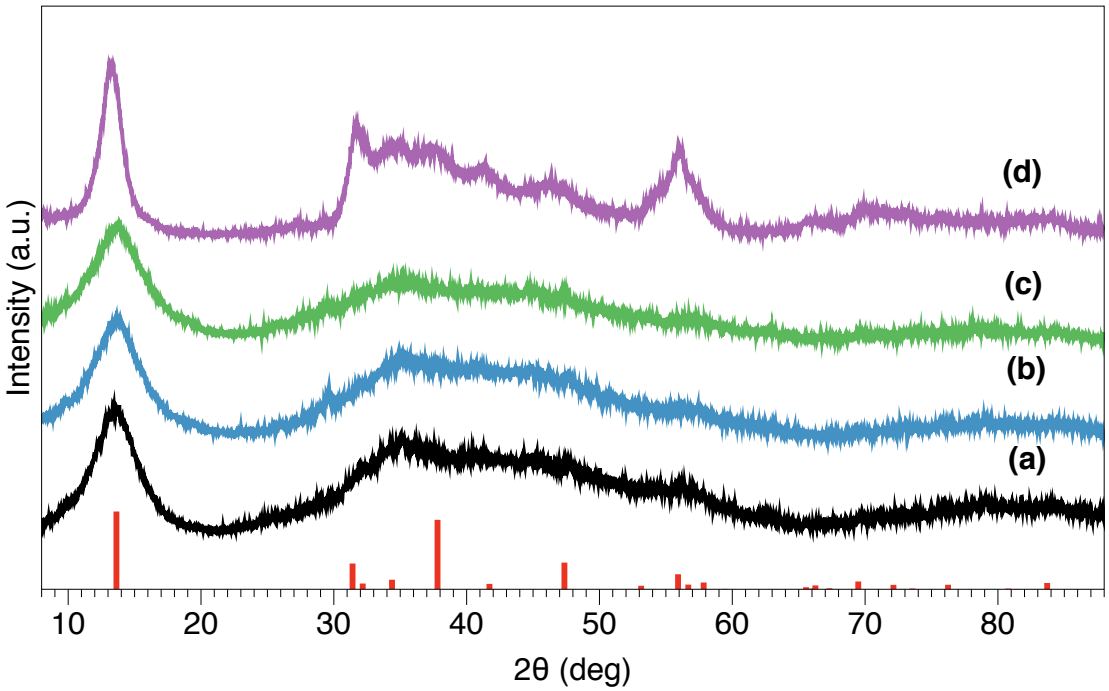

Figure 3.6. XRD spectra of the (a) as-synthesized 2H WSe_2, (b) after BOAI-exchange, (c) after BOAI-exchange and 200 ^oC anneal, and (d) after BOAI-exchange and 400 ^oC anneal. Standard WSe_2 lines at the bottom of the plot are from PDF#00-038-1388.

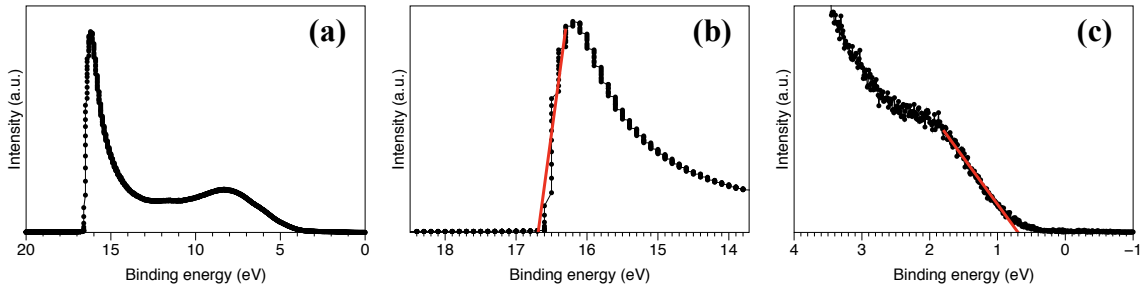

Figure 3.6. UPS spectrum of as-synthesized 2H WSe_2 nanocrystals. (b) and (c) include best fit lines used to determine WF and VBM-E_F.

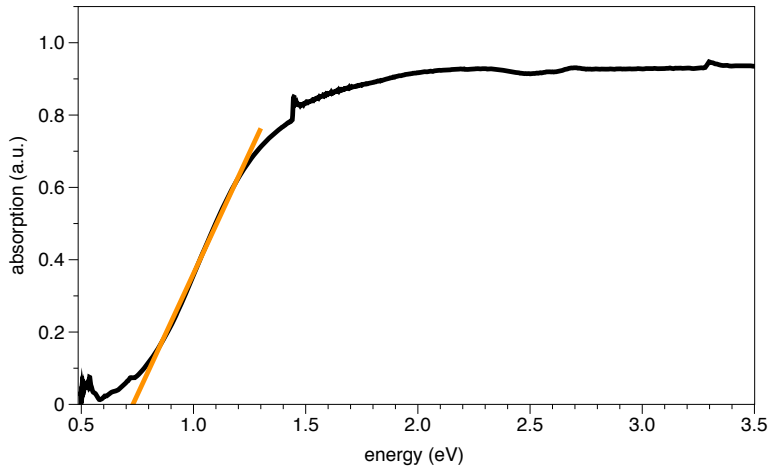

Figure 3.7. UV-Vis spectrum of 2H-WSe_2 fitted to determine band gap at 0.75 eV. The sharp peak at ~1.5 eV is due to the instrument.

After successfully fabricating 2H-WSe_2 via a colloidal synthesis, the next challenge was to passivate the dangling bonds at the edge of the crystallites. This particular synthesis does not use any specific capping ligand, as besides W and Se, there are only carbonyl ligands and para-xylene solvent present. From FTIR data, it appears that the carbonyl ligands do not remain in the final product (Fig. 3.8). In order to minimize edge oxidation, the WSe_2 product was worked up under air-free conditions. On average, the as-synthesized material was 4.65 nm in the (002) direction (via Scherrer analysis of the XRD) and the small size of the crystallites was confirmed by TEM (Fig. 3.9). Initially I attempted to decrease the number of dangling bonds by heating a dropcasted thin film to allow the grains to grow in size. I found it was critical that a boat of Se powder be present upstream from the samples in the annealing tube, else there was a loss of Se to substoichometric levels (Fig. 3.4). While there was a small amount of grain growth (via XRD), the material did not show a PL response (data not shown).

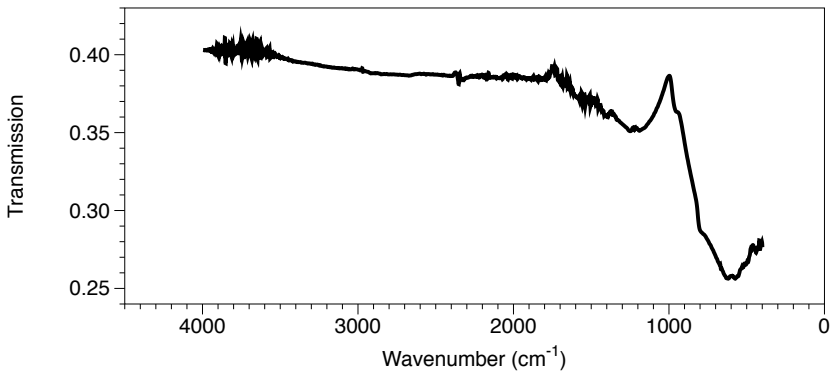

Figure 3.8. FTIR of 2H WSe_2 nanocrystals. The lack of peaks in the 3000 cm^{-1} and 1670-1820 cm^{-1} regions indicate that the nanocrystals are not passivated by either carbonyl or p-xylene.

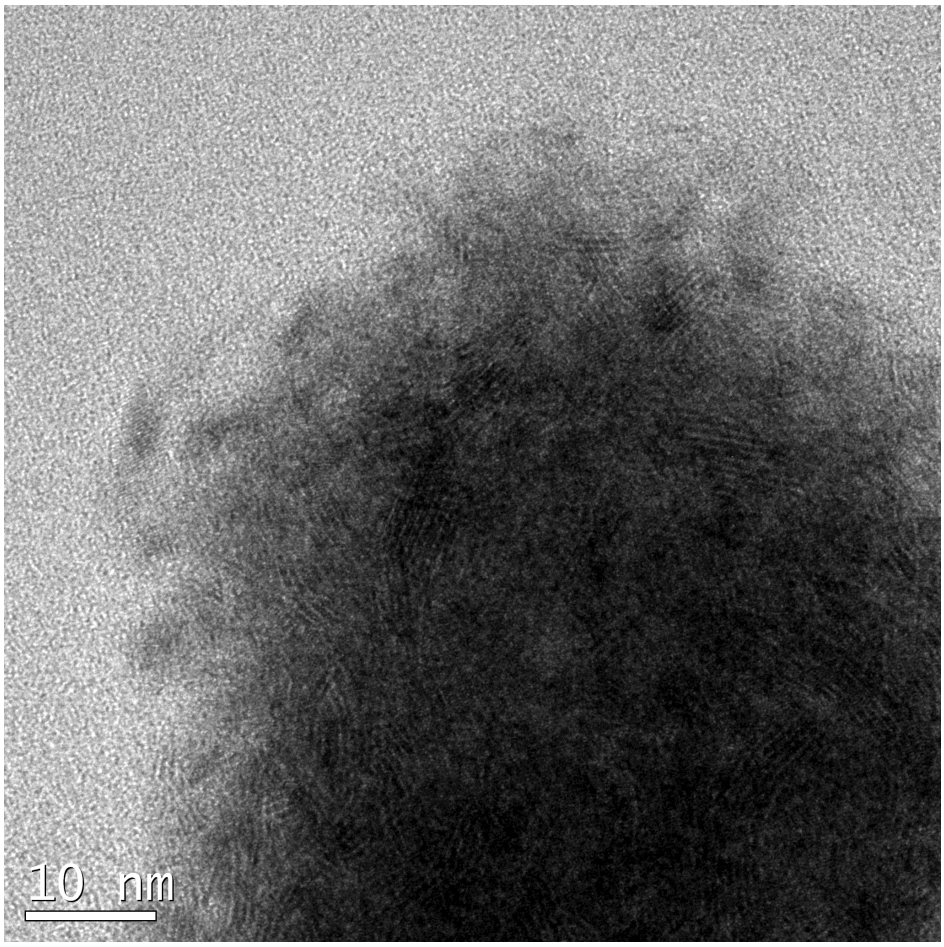

Figure 3.9. TEM of 2H-WSe2 nanocrystals, displaying small crystallite size.

I next tried chemical passivation by utilizing WSe_2's affinity for iodine. Instead of photoetching in an iodine electrolyte, as was done in the literature for WSe_2 PEC cells, I

synthesized N-butyloctadec-9-en-1-aminium iodide (BOAI) to passivate the material in a colloidal suspension. BOAI was suggested by the Sargent group in the literature where they demonstrated its ability to bind and passivate PbS.[173] In addition to passivation with BOAI, I also annealed the samples for 30 minutes at a low (200 ^{o}C) and high (400 ^{o}C) temperature. With both the BOAI exchange and annealing at the higher temperature, there were distinct changes in the electronic structure by UV-Vis (Fig. 3.10). Consistently, the as synthesized material demonstrated a band gap of ~0.75 eV (Fig. 3.7), which is much lower than the bulk values of 1.4-1.5 eV from the literature. After BOAI exchange, the bandgap shifts even lower, to perhaps below 0.5 eV (Fig. 3.10a), but because of instrument limitations one cannot precisely infer the bandgap from the UV-Vis spectra. The structure essentially did not change after the 200 ^{o}C anneal (Fig. 3.10b) but did shift to what appears to be a metallic compound after annealing at 400 ^{o}C (Fig. 3.10c). Due to the small size of the bandgap, I was unable to test a PL response, nor is a material with a bandgap smaller than 0.75 eV desirable for photovoltaic applications, as it would be limit solar cell efficiency to < 20%.

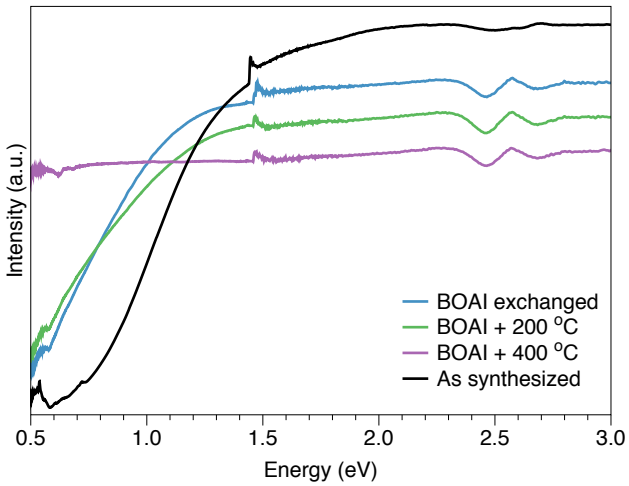

Figure 3.10. UV-Vis spectra of as synthesized WSe_2 NCs, BOAI-exchanged WSe_2 NCs without annealing, with a 200 ^{o}C anneal, and with a 400 ^{o}C anneal under Ar with Se boat. Spectra are offset for clarity.

As the WSe_2 nanoparticles synthesized and described above are not suitable for photovoltaic applications, I will briefly mention that I attempted a number of other syntheses, including one put forth by the Brutchy group that claimed to produce 2H-WSe_2 with high in-plane conductivity. While high in-plane conductivity is desirable, it would still require rethinking the conventional solar cell device design. In the publication, the authors only used Raman spectroscopy to characterize the polytype, which as demonstrated previously is a fairly ambiguous method. When I duplicated the synthesis and examined the material with XPS, it was clear that the high conductivity was likely due to the prominent 1T polytype present (Fig. 3.2a). Before this XPS analysis, I did fabricate a few full devices (Mo/WSe_2/CdS/AZO/Al) with the WSe_2 nanosheets and they did not show any photoresponse nor an obvious bandgap via UV-Vis spectroscopy; again, likely due to the 1T polytype presence. While I did attempt to convert the material to all 2H by annealing at an elevated temperature for an extended amount of time, there was no significant difference in the UV-Vis spectra and no PL response even after 12 hours at 200 ^{o}C. The average platelet thickness of 3 nm (~3 layers) (via Scherrer analysis of the (002) XRD peak) would lead one to expect some weak PL response if it was fully 2H and contained minimal basal plane defects. This may not have been a high enough temperature and it is perhaps worth looking into different annealing temperatures. Finally, I will note that when tested for catalysis activity, these nanosheets were very good at catalyzing the hydrogen evolution reaction, supporting the 1T characterization.

3.3 CONCLUSIONS

In summary, this work attempted to engineer around a number of issues for using nanocrystalline TMDCs, specifically WSe_2, for solid-state photovoltaics. While semiconducting 2H-polytype nanomaterials were successfully synthesized, the nanocrystals displayed a smaller-

than-expected bandgap. Passivation of the nanomaterials with an iodide-containing ligand acted to shrink the bandgap further and with annealing appears to have made the material metallic. Additionally, though the nanocrystals were small (~4 layers thick), any PL response is still expected to be dampened from the response of a monolayer. Overall, while WSe_2 and other TMDCs are attractive materials for solid-state photovoltaics due to their bulk and monolayer properties, colloidally synthesizing nanomaterials with a high proportion of edge sites does not appear to be a successful route to efficient solar absorbers. While perhaps more energy- or labor-intensive, exfoliation of bulk 2H TMDC samples into monolayers deserves more research for use of TMDCs in solid-state solar. While monolayers do not approach the thickness requirement for absorbing 90% of the incident light, one could imagine such thin and slightly transparent solar cells as a layer in windows, acting to both harvest energy and modulate the amount of light coming through the window.

3.4 Experimental Details

3.4.1 *2H-WSe_2 Nanocrystals by Duphil et al.*[141]

18 mg Se powder (Sigma Aldrich, 200 mesh) is dispersed in 100 mL p-xylene (TCI America) and stir for 30 min at 140 ^{o}C under Ar atmosphere. The solution is cooled to 100 ^{o}C and 0.040 g $W(CO)_{6,}$ (Sigma Aldrich) is added. The temperature is then raised to 140 ^{o}C and the reaction is held there for 100 hours. The concentrations of Se and $W(CO)_6$ were increased 8x with no obvious changes in product. Nanocrystals were worked up via centrifugation under N_2 with toluene and ethyl acetate.

3.4.2 *Highly Conductive Nanosheet synthesis by Antunez et al.*[140]

0.46 mmol (150 mg) WCl_4 (Strem Chemicals, 97%) was added to 25 mL dodecylamine (TCI America) and, under Ar, heated to 95 ^oC, where the solution is held for 10 min. The reaction is cycled under vacuum three times to remove any lingering water. The solution is then heated to 150 ^oC where ~ 185 µL of $^tBu_2Se_2$ (synthesized via method by Antunez *et al.*) in hexanes is injected, though the actual concentration of this solution is unknown. The temperature is then raised to 225 ^oC and held for 6 hours. The solution is cooled to room temperature, injected with 10 mL of 20 mg/mL trioctylammonium bromide (TOAB, Sigma Aldrich) in dichloromethane (DCM, Fisher Scientific) and centrifuged. The nanocrystal product is resuspended in TOAB/DCM and washed 2x with ethanol. The product is finally suspended in toluene.

3.4.3 *Synthesis of N-butyloctadec-9-en-1-aminium iodide*

2.21 g of tetrabutylammonium iodide (Sigma Aldrich) is mixed with 10 mL oleylamine in a Schlenk flask under N_2. The solution is heated to 200 ^oC, and held there for 2 hours, after which it is cooled to 40 ^oC and held at this temperature under vacuum for 2 hours. While warm, the vial is brought into a glovebox where ~1 mL BOAI per 10 mL of nanocrystals suspended in toluene. This solution was then stirred at room temperature overnight and then precipitated once with ethanol. The BOAI-exchanged nanocrystals were then suspended in heptane at an unknown concentration.

3.4.4 *Characterization*

Scanning electron microscope (SEM) images were acquired with a FEI XL830 dual beam instrument with integrated electron dispersive X-ray spectrometer (EDS) by Oxford. Typical

operating conditions were 5 keV electron beam for SEM and 20 keV for EDS. Powder X-ray diffraction patterns (XRD) were taken with a Bruker D8 Discover with GADDS 2-D XRD using Cu Kα radiation. X-ray photoelectron spectroscopy (XPS) and ultraviolet photoelectron spectroscopy (UPS) was performed under high vacuum conditions in a Kratos AXIS Ultra instrument; samples were prepared by dropcasting the nanocrystals from an organic suspension on to a clean piece of Si or Ti, typically within a glovebox. Once on the substrate, samples were treated by annealing as mentioned in the text and quickly transferred to the instrument chamber to minimize oxidation in air. Samples were annealed under Ar in a tube furnace with a boat containing Se powder upstream. Samples were exposed to air during transfer to and from the furnace but stored in a glovebox until analysis. An Al Kα source was used for XPS and He(I) for UPS. XPS spectra were referenced to the C-C peak at 284.4 eV and UPS spectra were referenced to an Au sample. A sample of WSe_2 grown via CVD from HQ Graphene was analyzed and used as a standard for fitting of the W 4*f* spectra. A Bruker Vertex 70 Fourier transform infrared spectrometer (FTIR) and a TA Q50 thermogravimetric analyzer (TGA) were also used for characterization. UV-Vis spectra were acquired with a dual beam Perkin Elmer Lambda 1050 Spectrometer with an integrating sphere attachment; samples were dropcasted on to glass slides for measurement. TEM images were recorded under bright field condition on a FEI Tecnai G2 F-20 instrument. TEM samples were prepared by dropping ~ 10 μL of a very dilute solution of nanocrystals in hexanes on to copper grids covered with carbon film.

Chapter 4. WSe_2 FOR HYDROGEN EVOLUTION CATALYSIS

4.1 INTRODUCTION

As discussed in the previous chapter, WSe_2, as well as other transition metal dichalcogenides (TMDCs) MoS_2, $MoSe_2$, and WS_2, can form in two (or more) polytypes with a hexagonal (2H) or tetragonal (1T) crystal structure. Again, this crystal structure difference has consequences on the band structure, resulting in either a metallic (1T) or semiconducting (2H) material. While the metallic 1T structure is detrimental for a solar cell application, it can be useful for catalyzing the hydrogen evolution reaction. The TMDCs mentioned previously have been highlighted for possible catalysis applications.[150,174–181] The materials are promising earth abundant alternatives to Pt metal, which, while excellent for catalyzing the hydrogen evolution reaction (HER), is both expensive and difficult to source. As reflected in the literature, MoS_2 has seen intense research for catalysis applications, but the other materials less so, especially WSe_2.[176,182] In addition to their earth abundance, mentioned previously, the outside chalcogenide layers in the basal plane are resistant to corrosion, promoting the stability of TMDCs as a HER catalyst. The corrosion resistance stems from the fully satisfied chalcogenide bonds, so if there are defects present the material is more prone to corrosion. Even though the basal planes of the WSe_2 materials discussed here are likely defective, as no care was taken to ensure perfect basal planes, the materials demonstrate remarkable corrosion resistance.

Previously, WSe_2 has been synthesized via mechanical exfoliation and CVD, but both methods are not easily scaled.[183–185] Recent work with MOCVD and vapor-liquid-solid growth show potential for scalable mono- and thin-layer WSe_2 and for vertically aligned WSe_2, respectively, but material must still be grown on a substrate and requires high reaction temperatures.[175,180,186,187] The most scalable methods in the literature can form very thin and

active WSe_2 layers on a substrate, but the material must be chemically exfoliated before deposition to transform into the 1T polytype.[147,188]

Herein is described synthesis of WSe_2 nanocrystals via a substrate-free solvothermal route. The WSe_2 material is predominately in the 1T-WSe_2 form without exfoliation and is useful for catalysis. A substrate-free material could expand design and engineering opportunities for hydrogen evolution reactors. Additionally, Meerwein's salt, a mild stripping reagent, is used to remove ligands from the colloidal synthesis from the surface of the nanomaterial, correlating with an increased catalytic activity post-stripping. However, the increase in surface area alone cannot account for all of the increased activity. Instead it is determined that there is a change in electron density on the surface of the material with removal of the ligands that alters the hydrogen absorption energy.

Before detailing the experimental results, a brief introduction to the mechanism of HER catalysis is presented. Initially, a hydrogen ion is absorbed on to the surface of the catalyst, termed the Volmer mechanism. The metal-hydrogen (M-H) bond strength influences the strength of this absorption (ΔG_{ad}). After absorption, the reaction proceeds via one of two mechanisms. In the Tafel mechanism, a second H^+ is absorbed on to the catalyst and then the two H^+ ions bond and desorb from the catalyst as H_2. The second possible route is termed the Heyrovsky mechanism. In this mechanism, a second H^+ ion bonds with the absorbed H^+ without first bonding with the catalyst surface. For an excellent illustration of these two mechanisms, the reader is referred to the paper by Morales-Guio *et al*.[189] Within this thesis, the focus will be on the M-H bond strength as it relates to catalytic activity with little discussion as to rate-limiting mechanisms, as the electrochemical measurements do not give a clear indication of what mechanism is rate limiting in these material systems.

Within the electrochemical measurements, linear sweep voltammetry (LSV) will be featured in this report. The key value in an LSV plot is the overpotential (V) at 10 mA/cm^2. This is a measure of how much potential must be applied to generate a current at that value and is typically used across the HER field to compare catalyst activity. A catalyst that requires a lower overpotential is a "better" catalyst. Platinum, with an overpotential of ~0.05 V at 10 mA/cm^2 is the standard against which HER catalysts are measured. Tafel plots, which are generated from the LSVs and are a measure of how much potential must be applied to increase the current by an order of magnitude, will also be included in the following discussion. Essentially, a smaller Tafel slope infers increased electron movement through the catalyst or an increase in reaction kinetics. The exchange current density is the current produced with no applied overpotential and is found by extrapolating the Tafel plot to the x-axis, where V=0. This value is a measure of intrinsic electron transfer rates between the catalyst/electrode and the analyte, where a higher value infers a better catalyst.

4.2 Results and Discussion

The WSe_2 nanocrystals produced by this synthesis were imaged via SEM and found to have a plate-like structure (Fig. 4.1). XRD analysis revealed the amine intercalation and utilizing Bragg's law it was determined that the (001) spacing along the c-axis is widened from 6.408 Å to 10.40 Å (Fig. 4.2). The difference in spacing indicates that the intercalated dodecylamine lays perpendicular to the c-axis, parallel to the WSe_2 basal plane.[190] This is not unusual for TMDC materials; over a decade ago, Vanchura and colleagues published an autoclave synthesis for M/WS_2 in dodecylamine that resulted in an amine-intercalated compound.[191] More recently, octylamine intercalated $MoSe_2$ was reported via synthesis similar to the one used in this

report.[192] Outside of these reports, intercalated TMDCs are produced via lithium exfoliation. We interpret the ~4 Å increase in interlayer spacing as the dodecylamine lying parallel to the basel plane (Scheme 4.1). If the dodecylamine were perpendicular to the basel plane, we would expect to see at least a 17.7 Å increase in spacing (length of DDA via Bain's formula[193]). When dodecylamine intercalated bentonite, researchers determined the DDA to be parallel to the silicate layers and to have a thickness of ~4.1 Å, a value similar to that found in the WSe_2 material here.[194] By virtue of the extreme excess of DDA versus diphenyl ether present in the reaction, we believe the DDA is the intercalated species. It is unclear how the WSe_2 material is intercalated, though it seems likely that the DDA, with a pKa of ~10, remains protonated during the reaction and stabilizes each layer through a Columbic interaction. In some of the annealed samples there appears to be a peak at ~23.7 ^{o}, which we attribute to WO_3 This peak is not consistent in presence or intensity across samples and is likely due to sample oxidation with air exposure.

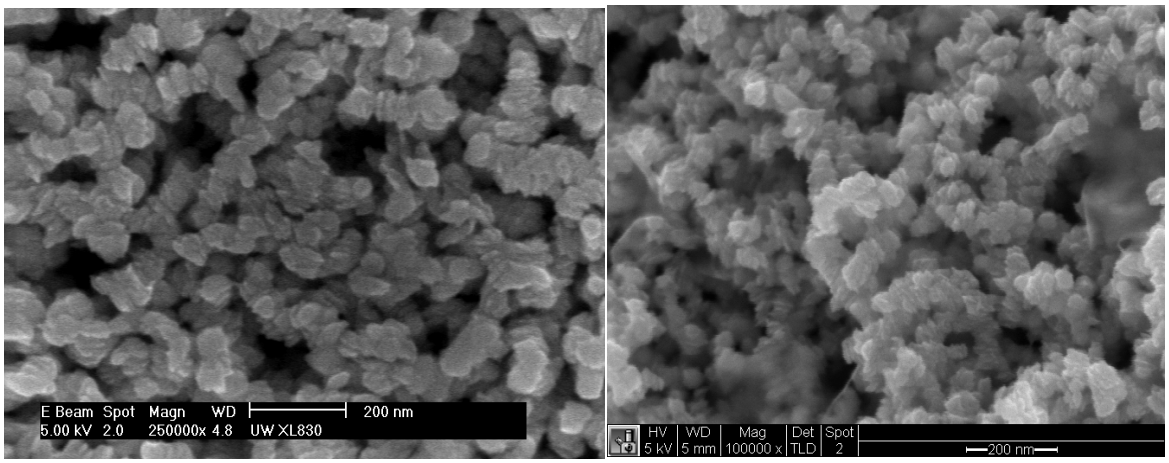

Figure 4.1. The WSe2 nanocrystals have a slight plate-like structure.

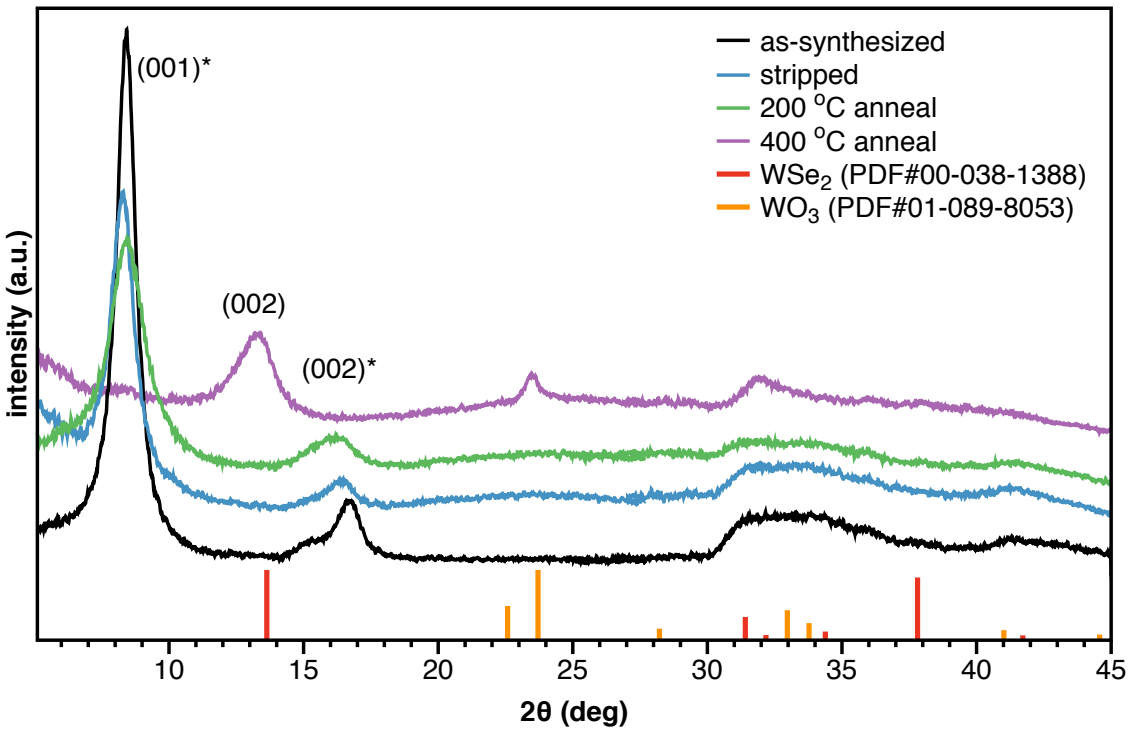

Figure 4.2. XRD spectra for WSe_2 nanocrystals comparing as synthesized, chemically stripped, and annealed crystals. The samples were annealed at 200 °C or 400 °C for 30 minutes in a tube furnace under flowing Ar with a boat of Se powder present.

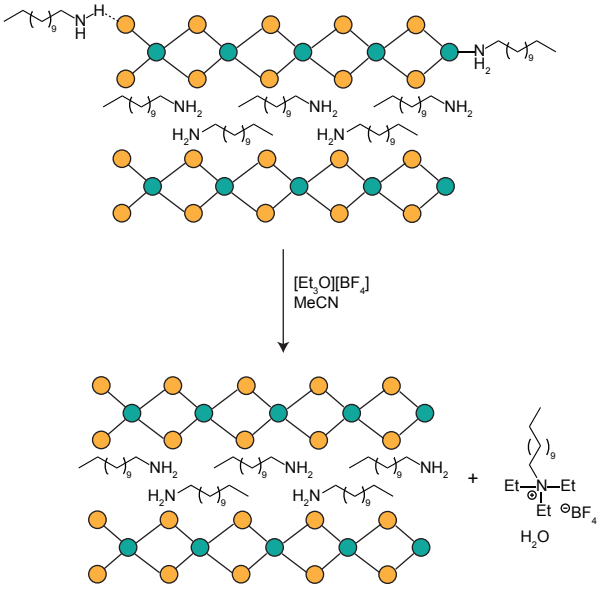

Scheme 4.1. Illustration of ligand removal by Meerwein's reagent. Intercalated ligands are not affected.

A number of different long-chain amines can be used for this reaction; we have specifically synthesized WSe_2 nanocrystals with oleylamine (OLA) and octadecylamine (ODA)

as the solvent. While octylamine was tested, the boiling point was too low for the 1,3-Diethyl-imidazolidine-2-selenone to react. Oleic acid was also tested, however the product of the reaction was a mixture of WSe_2 and WO_3 (Fig. 4.3). Scherrer analysis found a small expansion in interplane spacing with the longer chain amine, but no significant difference if a vinyl group was present (OLA) or not (ODA) (Fig. 4.4). We found that the ratio of precursors does not impact the final product morphology or composition (Fig. 4.5a,b). It was discovered that the Se precursor injection solvent affects the morphology of the final product, producing nanoplates to nanoflowers (Fig. 4.5), but it is unclear if the ether type affects morphology just due to a higher boiling point or if the interaction with the Se precursor directs the morphology change.

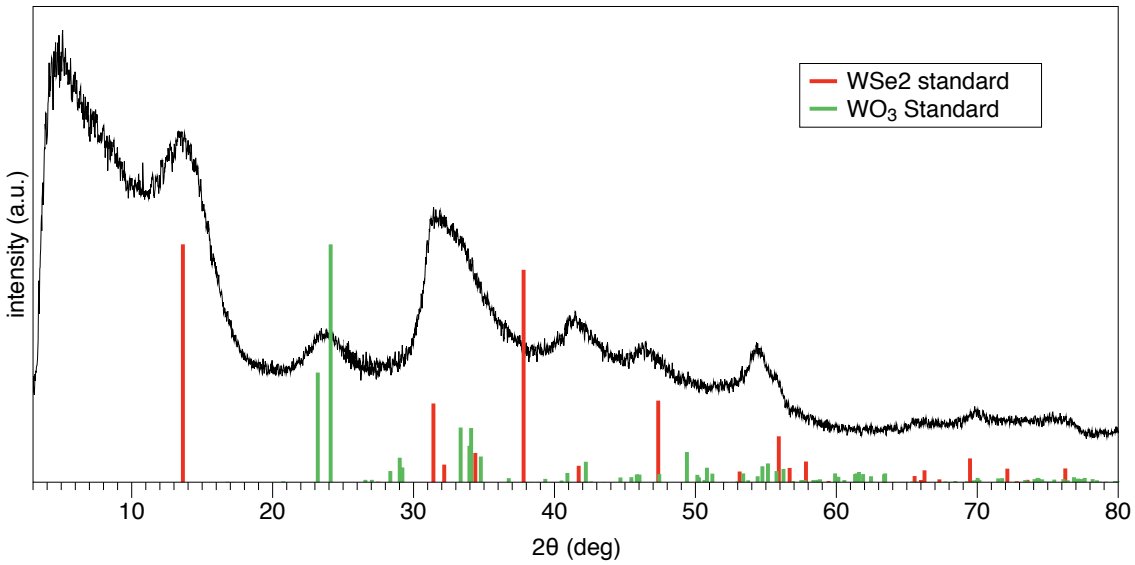

Figure 4.3. XRD spectrum of nanomaterials synthesized with oleic acid as the solvent and capping ligand.

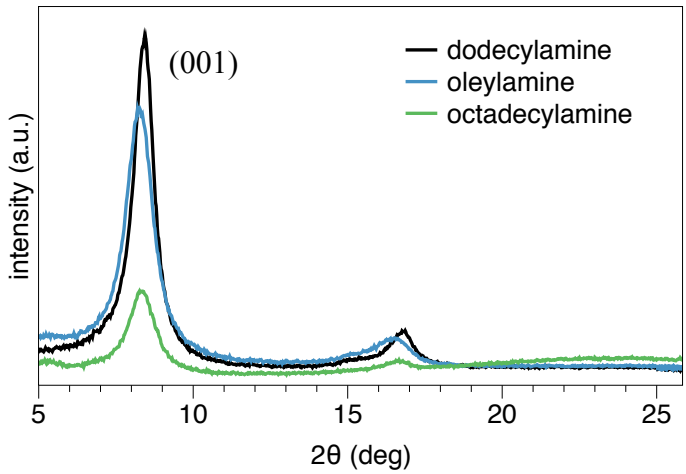

Figure 4.4. XRD spectra of samples synthesized in DDA (black), OLA (blue), and ODA (green), demonstrating change in (001) spacing with different amine.

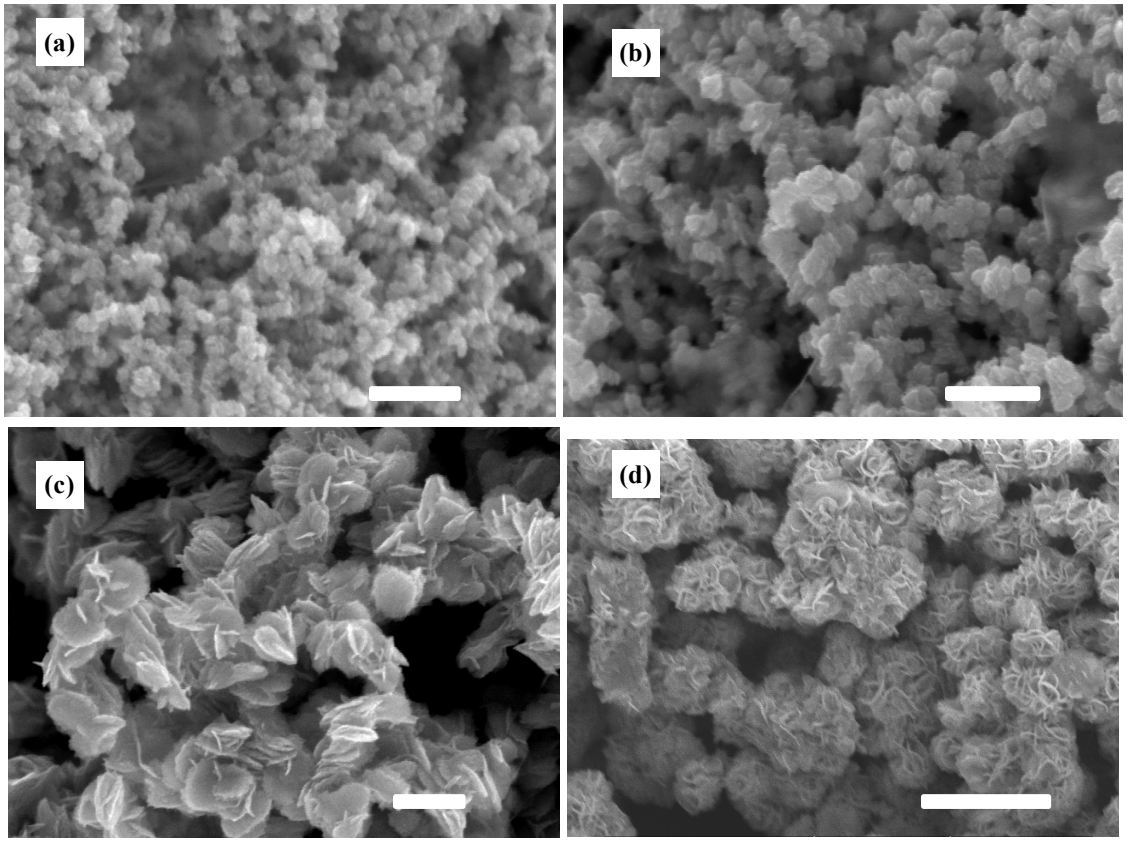

Figure 4.5. (A) 2:1 Se:W; diphenyl ether injection solvent; (B) 1:1 Se:W; diphenyl ether injection solvent; (C) 2:1 Se:W; tetraglyme injection solvent; (D) 1:1 Se:W; octyl ether injection solvent. The scale bars in (a-c) are 200 nm and in (d) is 2 µm.

There was no effort to get precise loading values because the nanocrystal capping ligands prevented accurate weight measurements, however the electrodes were loaded with the same

volume of suspension each time. Initially, the WSe_2 NCs performed modestly, requiring an overpotential of ~580 mV to produce a 10 mA/cm^2 current. When the electrode was treated with Meerwein's reagent in acetonitrile (ACN), the overpotential decreased by 118 mV at 10 mA/cm^2_{geo} (Fig. 4.6a). To confirm that it is indeed a removal of the ligands that causes the change in overpotential (Δ_{OP}), the electrode was dipped in a solution of DDA in toluene and remeasured. It was found that the overpotential increases with addition of the amine (Fig. 4.6b). When the LSVs were corrected with electrochemically active surface area values, it was found that the Δ_{OP} was not fully accounted for with the correction (Fig 4.6a inset). To account for this, it is thought that there is a fundamental change in the intrinsic catalytically ability of the WSe_2 in the form of a change in hydrogen adsorption energy (ΔG_{ad}).

The specific effect of Meerwein's reagent on the overpotential of HER catalyzed by WSe_2 is also influenced by material preparation. If the WSe_2 is post-synthetically worked up in air, an appreciable amount of oxide (indicated by the presence of W^{6+}) is observed by XPS (Fig. 4.7b). Comparatively, samples processed under air-free conditions have a minimal W^{6+} content (Fig. 4.7a). Additionally, Meerwein's reagent treatment decreases the oxide content in samples worked up in air (Fig. 4.8). With these oxide-containing samples, a loading study was conducted where more of the WSe_2 suspension was systematically added to the electrode between LSV scans. A decrease in overpotential was observed with higher WSe_2 loading until a point when the trend reversed, presumably due to significant resistance within layers of the deposited material (Fig. 4.9).[195,196] Upon treatment of the oxide-containing samples with Meerwein's reagent Δ_{OP} was found to range from 118 to 180 mV as a function of loading (Fig. 4.9). The electrochemically active surface area (ECSA) of the oxide-containing sample also had a greater

increase in surface area (5.4x) than the non-oxide containing samples, indicating that the W^{6+} is not as catalytically active as the W^{4+} and removal of the oxide exposes more active sites.

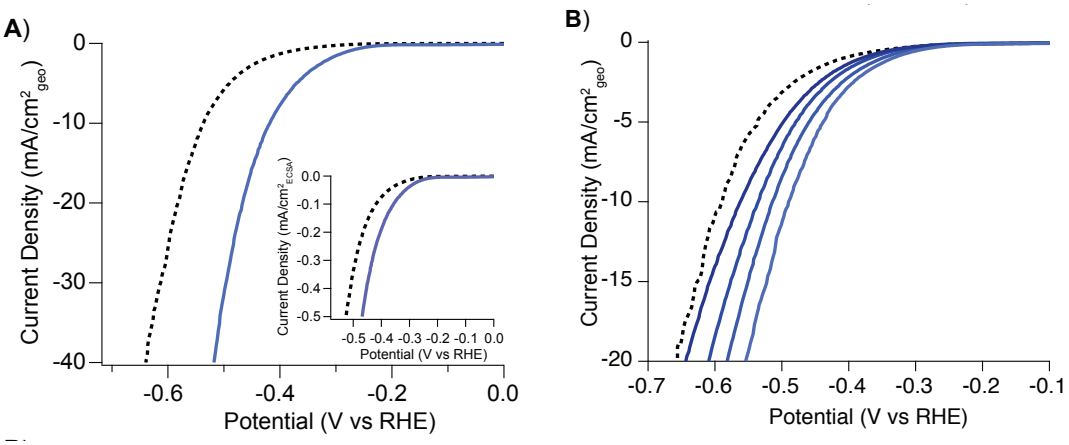

Figure 4.6. (a) LSV of WSe_2 deposited on a carbon fiber electrode before (dashed black line) and after treatment with Meerwein's reagent (solid blue line) in 0.5M H_2SO_4, inset depicts the same LSV corrected for ECSA calculated by CV. (b) LSVs of increasing amounts of amine religated on the surface of WSe_2 electrode. The as synthesized (dashed black) and the Meerwein's (solid blue) are the outermost traces. As the electrode is exposed to more dodecylamine (darker blue), the LSVs trend toward the as synthesized trace. All LSVs from Henckel *et al.*[197]

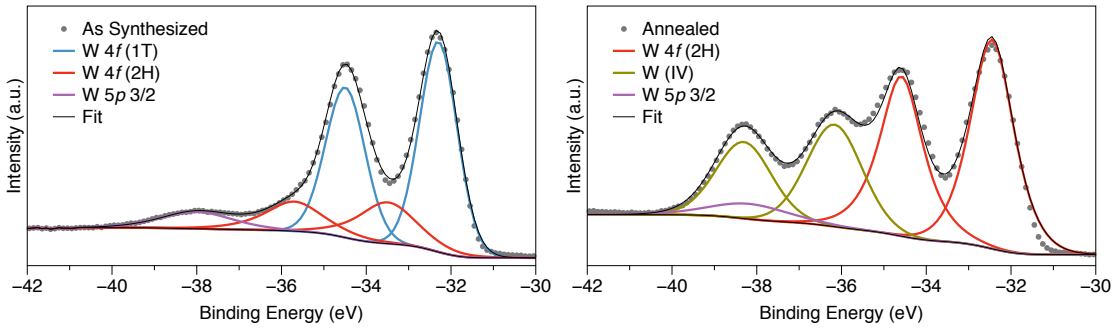

Figure 4.7. XPS of nanocrystals that underwent an (a) air-free work up or (b) work up in ambient conditions, indicating air-instability of W atoms.

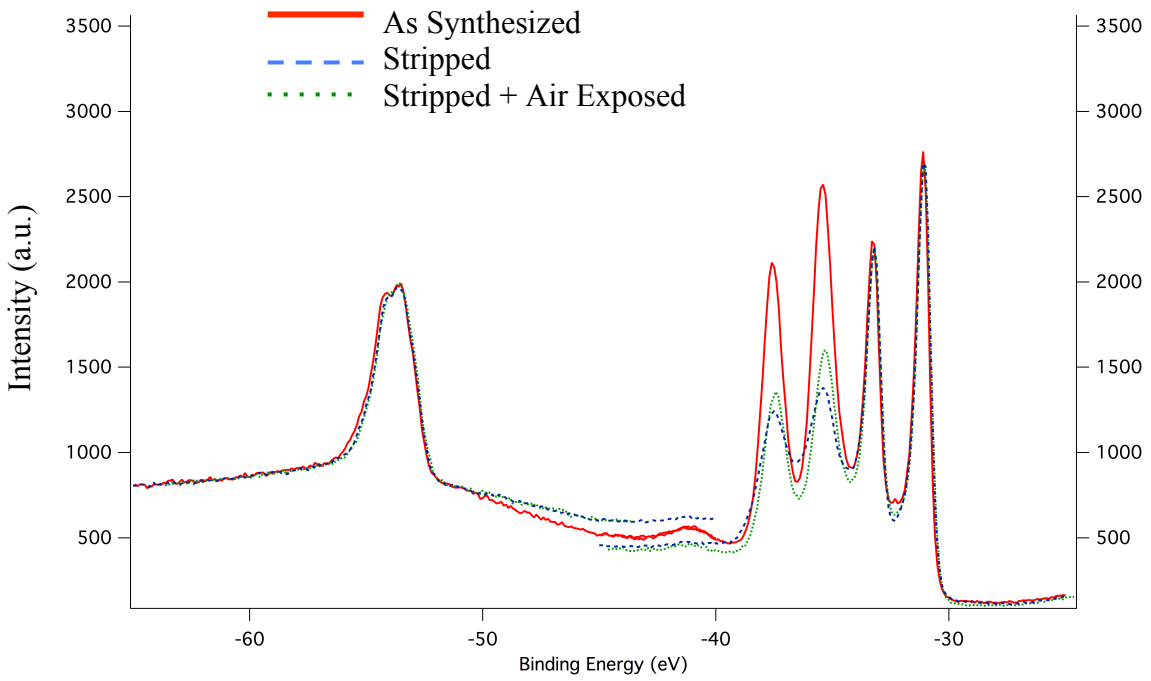

Figure 4.8. XPS spectra indicate that there is no SeO_2 present before or after stripping (expect a peak around -58 eV) and that the Se binding environment does not change noticeably in general with stripping. The W 4*f* (VI) binding area indicates that the Meerwein's reagent strips the W^{6+} sites. After stripping the quantity of W^{6+} increases when exposed to ambient air. The W^{4+} peaks align under all conditions, indicating insignificant change in the W^{4+} quantities with stripping or air exposure. The spectra here were taken at the Pacific Northwest National Lab and the stripped sample was not exposed to air before collecting data.

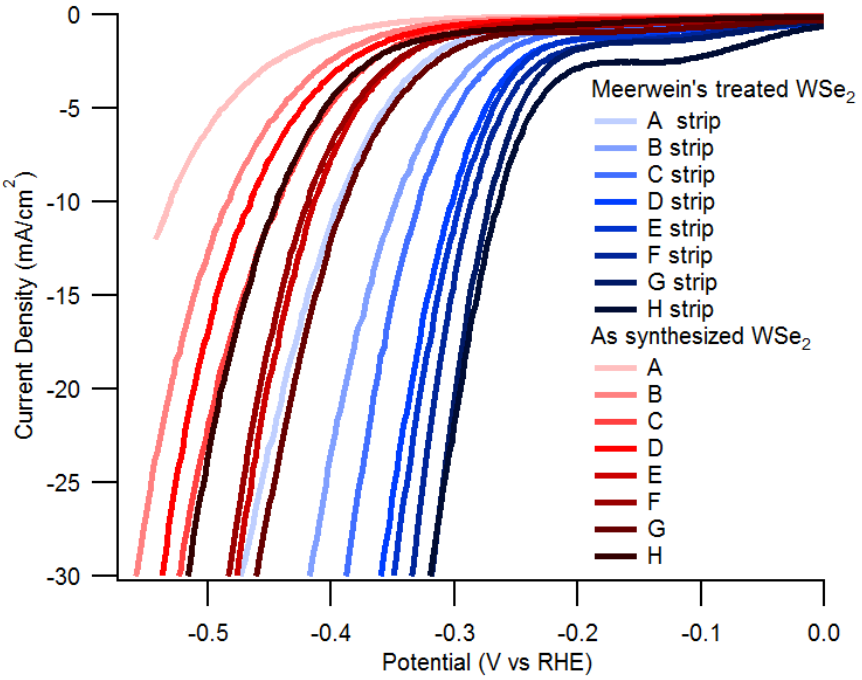

Figure 4.9. Study on the effect of loading where each trace has 20µL of additional nanoparticle suspension loaded on Δ_{OP} between the as synthesized and Meerwein's treated WSe_2.

To probe ΔG_H, ultraviolet photoelectron spectroscopy (UPS) was utilized of the samples worked up in air-free conditions (Fig. 4.10). From the UPS data one can estimate the location of the center of the d-band states nearest E_F. Typically a higher d-band center correlates with higher electron density near E_F (within 1 eV) and may explain the M-H bonding trends more accurately than a d-band center value calculated from a wider bandwidth, so for this data the focus is in the 0-1 eV binding energy range.[198] The "d-band center" value is determined by calculating the area under the curve from 0-1 eV and then finding the energy above and below at which the areas are equivalent. The distance between the d-band center and E_F has frequently been related to the M-H bond strength and/or ΔG_H.[199] While I recognize that the WSe_2 sample is not a pure metal, generally for TMDCs the d-band are the most significant contributor to valence band maximum region.[200,201] Qualitatively, from inspection of the VBM region in Figure S14, one can observe

that the stripped sample has lower electron density near E_F than the as-synthesized sample, which is attributed to the removal of the electron donating dodecylamine ligands Following relationships developed in the metallic HER catalyst literature, this indicates that the as-synthesized sample, with the smaller (E_d-E_F) distance and increased electron density near E_F, has fewer filled antibonding states than the stripped sample (Fig. 4.11). A stronger M-H bond has been correlated with more available antibonding states, leading to the conclusion that for these samples, the as-synthesized sample should have a stronger M-H bond than the stripped sample. If one uses the volcano plot relationship for metal catalysts, where a weaker M-H bond corresponds to a more thermoneutral ΔG_H, then it is expected that the stripped sample will produce a higher exchange current density (log j_0) than the as-synthesized WSe_2.[199] This fits the trend seen in these samples from the Tafel plots, where the Meerwein's treated WSe_2 has an exchange current density of 19 $\mu A/cm^2$ compared to 5.9 $\mu A/cm^2$ of the as-synthesized WSe_2 (Fig. 4.12).

A comparison of the electronic structure – catalytic activity relationship between the as synthesized/stripped samples with a fully annealed sample (>400 ^oC) is not as straightforward due to the amine intercalation. If the previous analysis of the as synthesized and stripped samples is extended, the UPS data would indicate that with the d-band center at 0.758 eV (again, looking only at the 0 to 1 eV range), one would expect the annealed sample performance to be similar to the stripped sample (Fig. 4.10). This does indeed correlate with the experimental data (Fig. 4.13). While this d-band center – performance trend is encouraging, it is noted that the annealed sample is significantly different from the others in two ways: annealing has increased the proportion of 2H-WSe_2 present and removed the intercalated amines. Thus, we do not attempt to attribute the increase in catalytic activity in the annealed sample to the same ligand removal in the stripped sample. Other intercalated TMDC studies in the literature suggest that if the material is

intercalated and the interlayer expanded, the material acts more like a monolayer than the bulk material, further increasing the differences between the as synthesized and annealed samples.[192,202] The increase of the semiconducting 2H-WSe_2 polytype potentially introduces more resistance, decreasing how readily electrons can flow from the electrode to the active site on the catalyst. Additionally, annealing promotes defect elimination. The combination of all these differences between an annealed and Meerwein's stripped sample make any comparison between the two, beyond the d-band center/activity relationship, complicated.

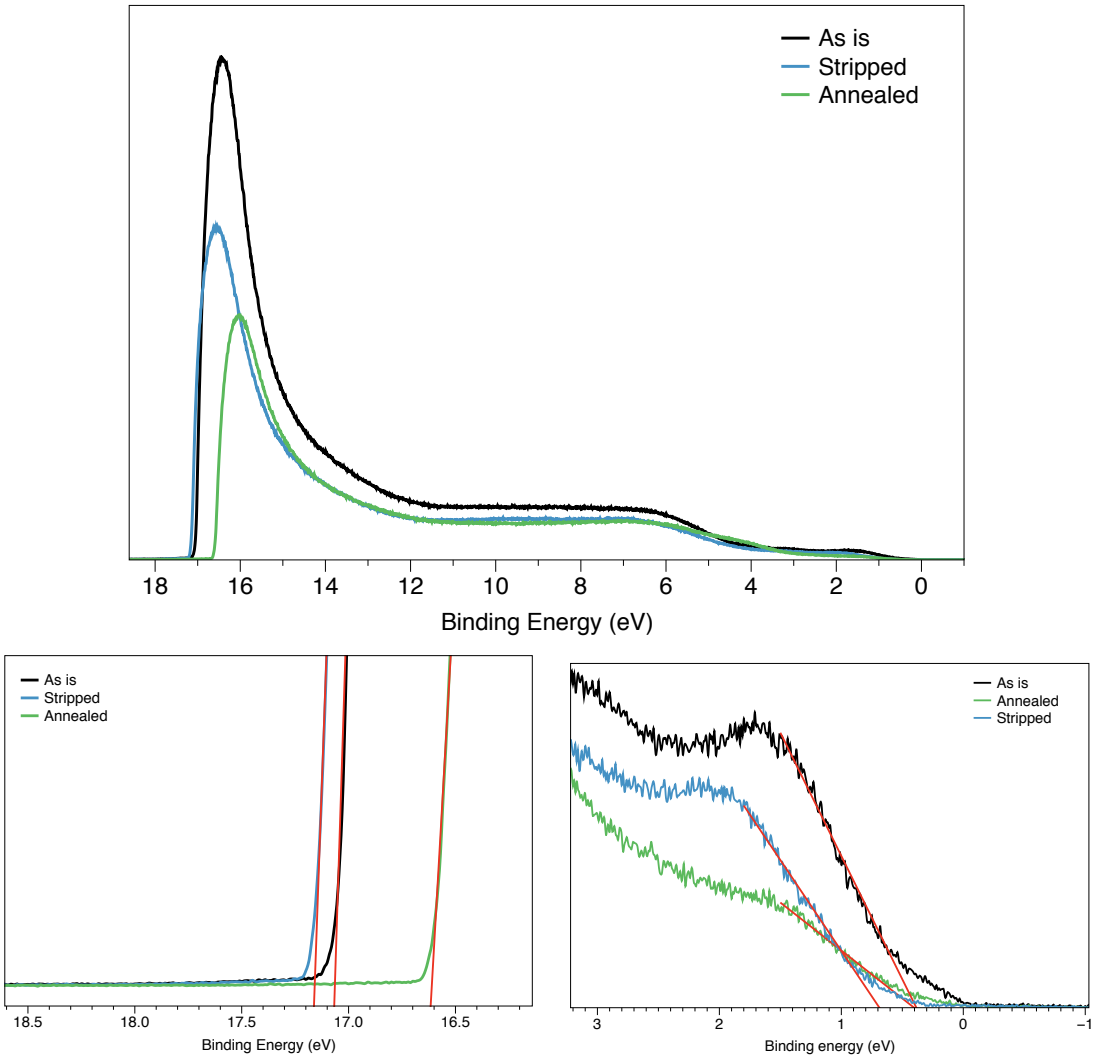

Figure 4.10. UPS spectra of the as synthesized (black), stripped (blue), and annealed (green) samples. Samples are fitted to find the workfunction (bottom left) and location of the VBM with respect to the E_F at 0 (bottom right).

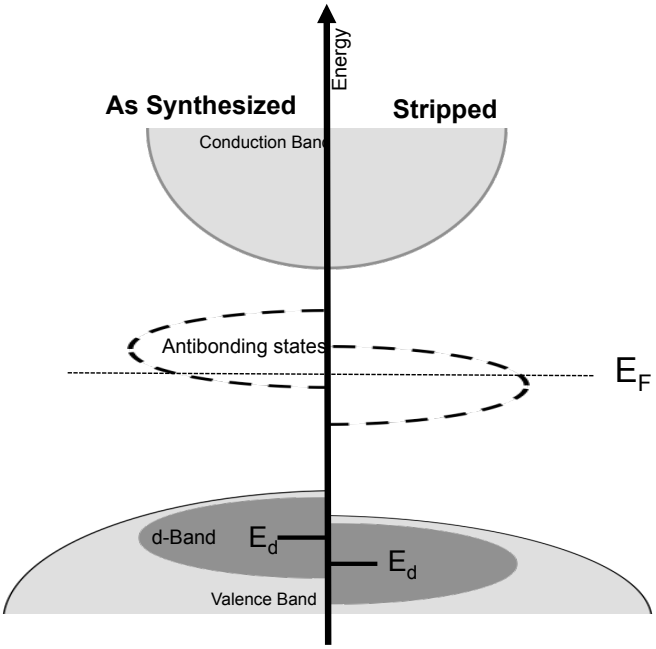

Figure 4.11. Qualitative d-band diagram, demonstrating difference in E_d between samples.

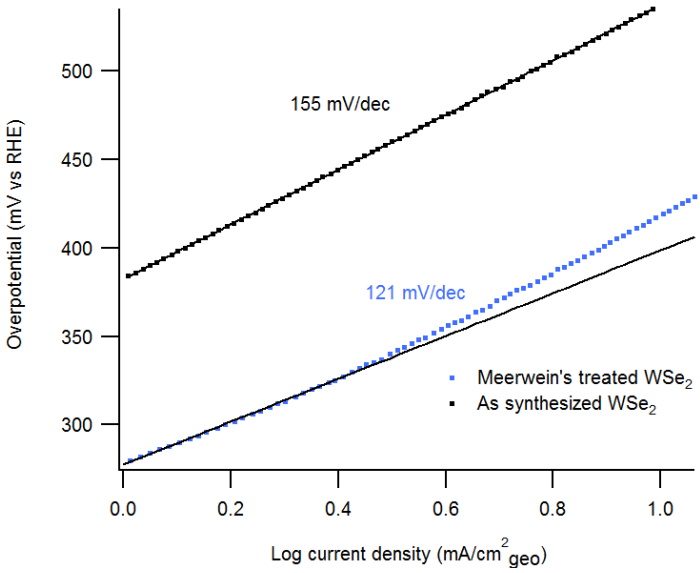

Figure 4.12. Tafel slopes plotted from LSV data shown in Figure 2a

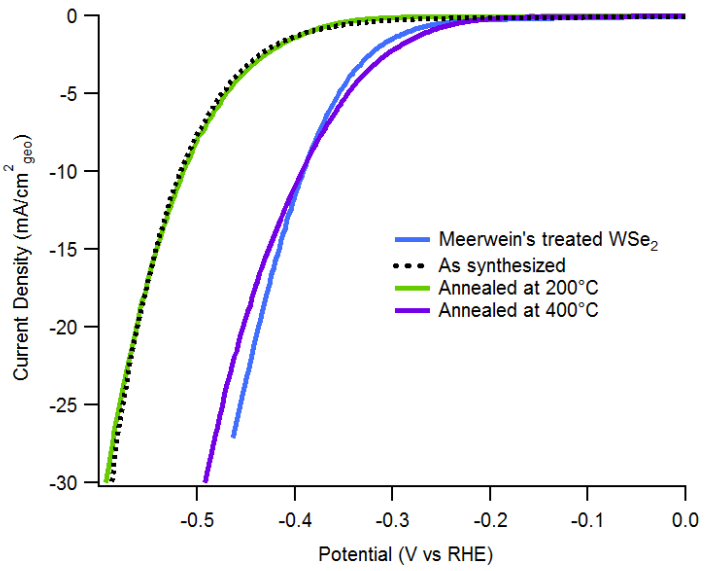

Figure 4.13. LSVs from the WSe_2 electrodes annealed at 200°C and 400°C compared to the as synthesized and Meerwein's treated electrodes

Thermogravimetric analysis reveals that only a small fraction of amine is stripped away with the Meerwein's reagent. We interpret this subset of ligand to be passively adsorbed to the material, as annealing above 200 ^{o}C is required for de-intercalation. When comparing normalized TGA traces for the as-synthesized and stripped samples, one observes a small difference in mass loss above 400 ^{o}C. We ascribe that difference to the stripping away of surface bound ligands by the Meerwein's reagent (Fig. 4.14). XRD confirms this interpretation, as the spectrum from the as-synthesized sample is identical to the stripped sample, while the annealed sample is distinctly different and peak locations align with the standard WSe_2 spectrum (Fig. 4.2). It is usual in the ligand stripping literature to use FTIR to confirm the removal of ligands, however with the intercalated amines in our sample, FTIR data does not present definitive data (Fig. 4.15). The only significant peak changes are visible between 2800-3000 cm^{-1} where the C-H stretches are visible until after annealing at 400 ^{o}C.

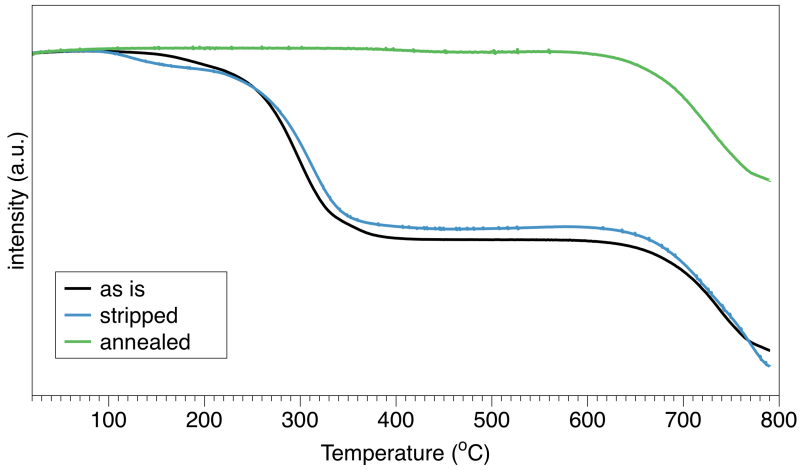

Figure 4.14. Thermogravemetric analysis of WSe_2 nanocrystals under N_2 atmosphere. We interpret these traces to indicate that with chemical stripping only the surface amines are removed, the intercalated amines remain until the material is annealed. TGA was completed at a 5 °C/min heating rate.

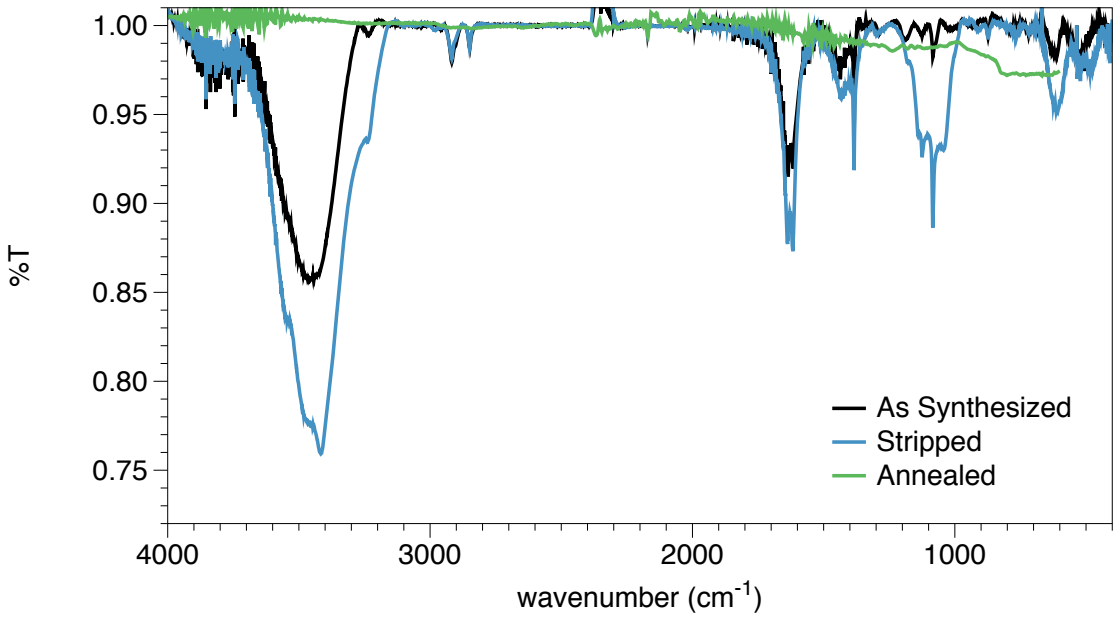

Figure 4.15. FTIR of WSe_2 as synthesized, stripped, and annealed indicates that only with annealing is all the amine eliminated from the sample.

Though the 1T and 2H polytypes of WSe_2 have different crystal structures, it is challenging to distinguish them via XRD.[203,204] As mentioned before, we turn to XPS, where careful analysis of the W^{4+} binding energies can help determine how much 1T and 2H is present in each sample.[205] The 2H polytype produces a pair of W^{4+} peaks, the $4f_{7/2}$ and $4f_{5/2}$, at ~ -31.5

eV and -33.5 eV, respectively. If there is 1T present, a pair of peaks at ~ -31 eV and -33 eV will be present. Peaks at higher binding energies can be ascribed to the W^{6+} state, which we assume is in the form of WO_3. The W $5p_{3/2}$ peak is also located in this binding energy area, at ~ -37 eV. The synthesis presented here produces oxide-free WSe_2 when the work up is done under rigorous air-free conditions and oxide formation in annealed samples is attributed to air exposure (Fig. 4.7a) before and after the annealing step. WSe_2 samples worked up under ambient conditions show the presence of W^{6+} peaks (Fig. 4.16). It is likely that the 1T polytype is stabilized by the intercalated ligands, but I cannot test this hypothesis as I am unable to de-intercalate the material without heat and, as previously described, heat also promotes 2H formation.[203]

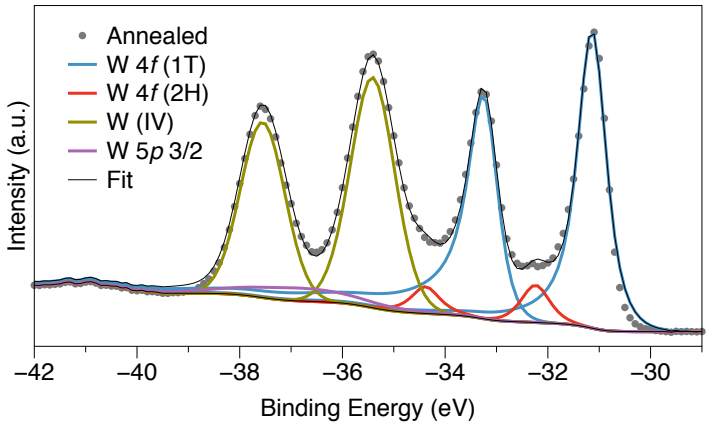

Figure 4.16. Fitted XPS spectrum of the W 4*f* binding energy for an as synthesized sample that was worked up in ambient conditions. Peaks for W^{4+} have been deconvoluted into separate peaks for the 1T and 2H polymorphs and W^{6+}.

By EDS analysis across a variety of samples, this synthesis produces WSe_2 with an atomic % composition of 66.9/33.1 (+/- 2.21) Se/W. After stripping the composition changes to 65.6/34.4 (+/- 3.05) Se/W; effectively the same as before within the margin of error (Fig. 4.17).

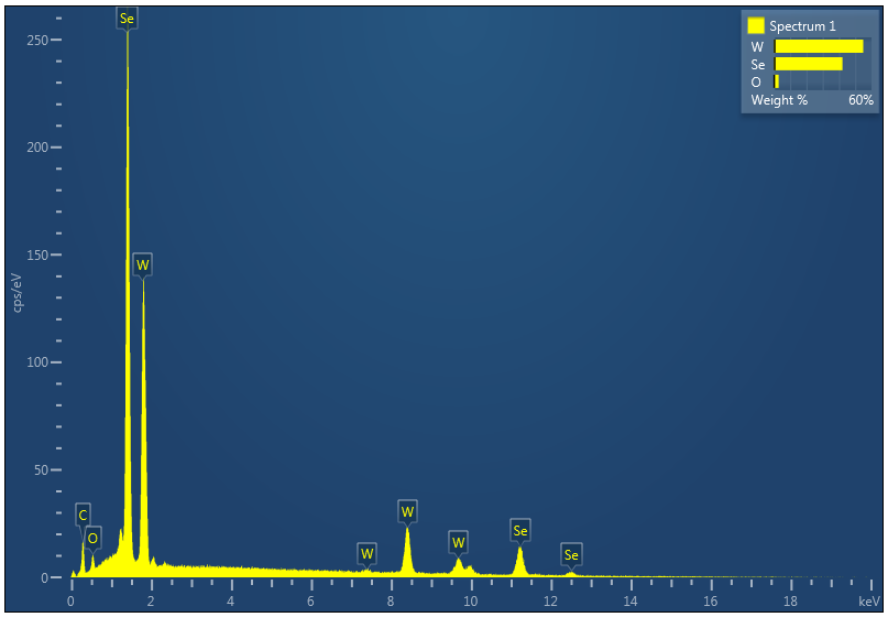

Figure 4.17. Sample EDS spectrum for intercalated WSe_2. Samples were prepared by depositing and treating samples on glass slides and then transferred to carbon tape for measurement.

Raman spectroscopy offers additional insight as to the structure of the WSe_2 NCs. Literature reports of pure 2H-WSe_2 identify peaks at 248 cm^{-1} and 250 cm^{-1} as A_{1g} and E_{2g} modes, respectively.[206] The limitations of the Raman spectroscopy instrumentation mean that one is unable to differentiate between the two peaks; instead a single peak is observed around 250 cm^{-1}. In all of our Raman experiments, the laser light was not intentionally polarized and wavelengths of 514 nm or 785 nm in a backscattering geometry was used to probe the sample. Additionally, both laser wavelengths produce a resonant Raman condition, as WSe_2 has A and B exciton energies of 1.17 eV (725 nm) and 230 eV (539 nm), respectively.[207,208] As seen in figure 4.18, the resulting Raman spectrum from each incident wavelength is distinctly different from one another and the as-synthesized sample spectra differ from the annealed spectra. The latter is expected, as the intercalation and defects present in the as-synthesized sample change the intensity of the Raman active modes. There are a number of variables present in these samples that change the Raman spectrum: the interlayer distance increased with the intercalation; there

are a limited, but not consistent, number of layers per 'petal'; there is significant 1T-polytype present in the as-synthesized samples; there is disorder on the basal plane; and many edge sites are present. Utilizing peak assignments found in the literature for $z(xx)\bar{z}$ polarized light spectra, which produces spectra essentially the same as using unpolarized light, peaks are assigned in the annealed spectrum measured with 785 nm light to specific expected Raman modes.[209] As the XRD reveals deintercalation with a 400 ^{o}C anneal and the XPS shows the material predominately made from 2H-polytype, this is not surprising. There is disagreement in the literature as to the locations of the A_{1g} and E^{1}_{2g} modes, with some assigning the A_{1g} peak around 260 cm-1[210,211] and others assigning them both around 250 cm-1 with the peak at 260 cm^{-1} assigned to a second order mode that becomes active with the presence of structural disorder.[147,209,212,213] A careful study under cross- and parallel-polarized light by Akintola et al. and Zhao et al. convincingly argues that the 260 cm^{-1} peak is not due to the A_{1g} peak because of its appearance under both polarizations.[170,209] The A_{1g} mode should not be visible under cross-polarized light. It is noted that the most detailed literature descriptions of WSe_2 Raman modes use fully 2H samples, exfoliated to a few layers with little disorder. As mentioned above, the samples here do not have such regularity nor are they pure 2H, as indicated by the XPS spectra, so the Raman spectra might not completely match with one published in the literature.

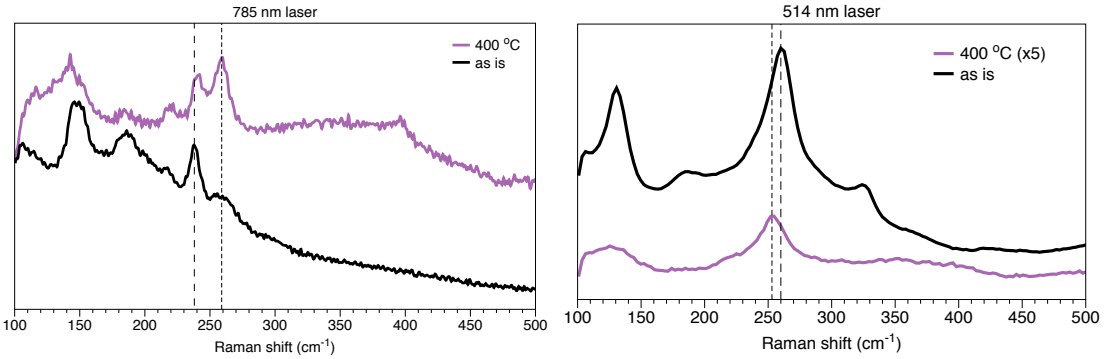

Figure 4.18. Unmodified Raman spectra of (black) as synthesized and (purple) annealed WSe_2 samples with two different incident lasers.

While the literature on Raman signatures for different TMDC polytypes is limited, in the case of MoS_2, it is shown that with intercalation and change to 1T-polytype, the A_{1g} and E^1_{2g} modes will disappear and peaks at lower wavenumbers will be present.[214–217] Similarly, the sole report on 2H- to 1T-WSe_2 measured with Raman spectroscopy argues that A_{1g} and E_{2g} shouldn't show up in the 1T-polytype and that peaks at ~50 and 150 cm^{-1} grow in.[211] In these samples, not all peaks could be indexed to a known Raman mode, but when the area between 245-260 cm^{-1} is fitted, no significant peaks are observed around 250 cm^{-1} in the as-synthesized samples, but they are seen in the annealed samples (Fig. 4.19). This correlates with the XPS data that indicates that the WSe_2 nanocrystals are majority 1T-polytype in the as-synthesized samples and become majority 2H with annealing. In the MoS/Se_2 literature, the ratio of A_{1g} to E^1_{2g} peak intensity is used to determine if the material is edge- or basal plane-terminated.[202,218,219] While those peaks are too close together to differentiate for WSe_2, it is suggested that the extra peaks in the Raman section indicate disorder and edge-abundance. This disorder contributes to the decreased overpotential values required for our WSe_2 nanocrystals when compared to values published for less disordered samples. Recently a theoretical study of 16 types of defects on the MoS_2 basal plane indicated that a number of them should be favorable for hydrogen absorption, with ΔG_H values close to thermoneutral.[220]

TABLE 4.1. PEAKS IDENTIFIED IN WSe_2 SAMPLES WITH RAMAN SPECTROSCOPY, UNDER CONDITIONS SPECIFIED IN THE TABLE.

				2M [209]	2M [209]	E^1_{2g}	A_{1g}	2(LA)M		A'^2_1 [169]		2M [209]
514 nm												
As Is		131.5	188.4		241.9			260.7	295		324.6	
Anneal		124.9				250.6	253.9			305.2	352.7	398.7
785 nm												
As is	108.9	148.4	186.9	215.1	238.31			260.6				
Anneal		140	184.7	219.5	240.14	251.59		259.7				396.6

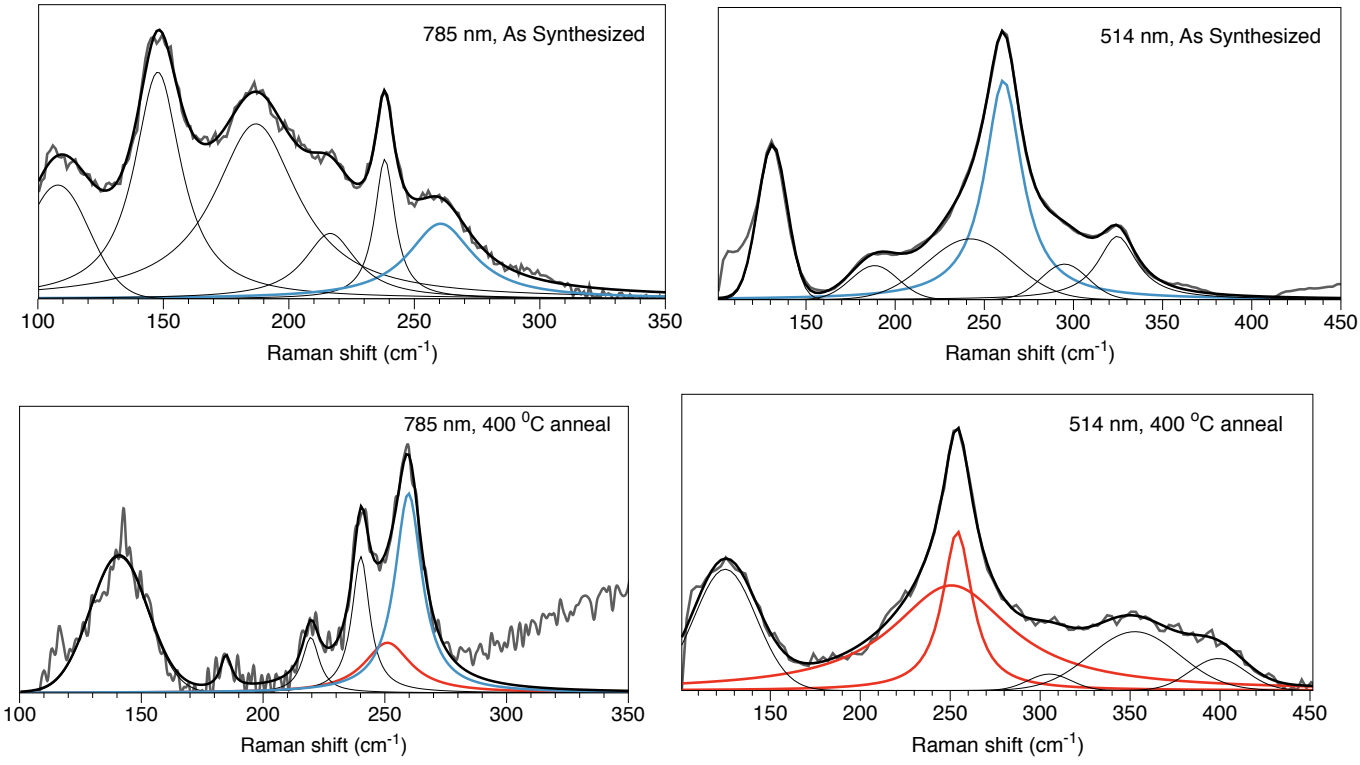

Figure 4.19 Fitted Raman spectra for (top) as-synthesized and (bottom) annealed samples analyzed with a (left) 785 nm or (right) 514 nm laser. Blue color indicates peak ~260 cm^{-1}, red indicates peaks around 250 cm^{-1}.

In addition to the research discussed above, there is an ongoing investigation of intentionally intercalated WSe_2 nanoflowers for HER. In this case, a large reduction in

overpotential is observed after electrochemically intercalating WSe_2 with a small amount of H^+, Li^+, Na^+, or K^+ ions. In the structural investigation of these catalysts, I have found that the ions are intercalating without the co-intercalation of the water solvent and, unexpectedly, the material remains in the 2H polytype after intercalation (Fig. 4.20, 4.21) Currently, the decrease in overpotential is attributed to an increase in electrons present, required for charge balance, in the WSe_2 catalyst with the intercalation of the alkali metals, but the investigation is ongoing.

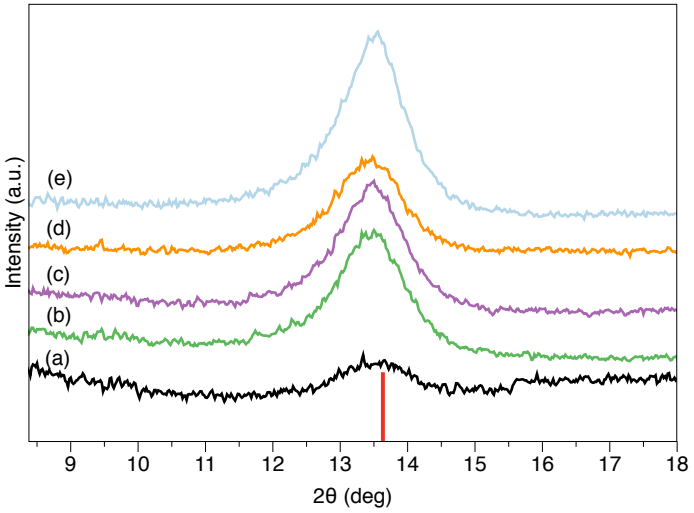

Figure 4.20. Close up view of the (002) peak in the (a) as synthesized, (b) Li, (c) K, and (d) Na intercalated WSe_2. Spectrum (e) was observed after the extended Na intercalation time. The bar on the x-axis is the expected (002) peak location for a bulk WSe_2 sample.

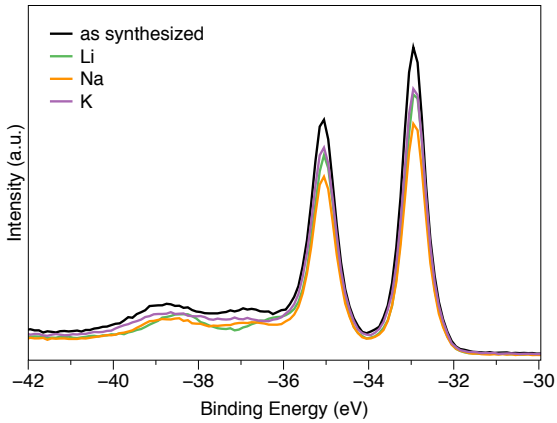

Figure 4.21. W 4*f* XPS data from the intercalated WSe_2 samples. The similarity of the spectrum before and after intercalation indicates that the material remains in the original 2H polytype post-intercalation.

4.3 CONCLUSIONS

In this chapter, the ligand influence on the catalytic activity of WSe_2 for hydrogen evolution was investigated and found to impact the catalyst beyond simply blocking active sites on the catalyst. After chemically removing the dodecylamine ligands, the increased electrochemically active surface area could not account for the full decrease in overpotential required at 10 mA/cm^2. An investigation of the surface with XPS and UPS revealed that the ligands additionally donated electron density to the as synthesized material, decreasing the distance between the d-band center and the Fermi level. This decrease in E_d has been linked to stronger M-H bonding due to a higher availability of antibonding states to bond with the H^+. This stronger M-H bonding is correlated with a larger ΔG_H, which in turn is linked with a comparatively higher overpotential. Thus, removal of the ligands affects both the availability of active sites and decreases the M-H bond strength, making the resulting WSe_2 material a more efficient catalyst.

4.4 EXPERIMENTAL DETAILS

4.4.1 *Materials*

Tungsten tetrachloride (WCl_4, Strem, stored in glovebox), dodecylamine (DDA, TCI America, distilled and stored in glovebox), diphenyl ether (distilled and stored in glovebox), triethyl orthoformate (TCI America), N,N′-dimethylethylenediamine (TCI America), selenium powder (Se, Sigma Aldrich, 200 mesh), acetonitrile (MeCN, Sigma Aldrich, anhydrous), and triethyloxonium tetrafluoroborate (Et_3OBF_4, Sigma Aldrich) are used as received unless otherwise noted.

4.4.2 *Synthesis of intercalated WSe_2 nanocrystals*

WCl_4 (0.23 mmol, 0.095 g) and dodecylamine (10 g) are combined in a scintillation vial in the glovebox and capped with a rubber septa. The vial is then sonicated for a minimal amount of time until the DDA has melted and all the WCl_4 has dissolved. The solution should be a uniform black color with yellow tones. The solution is injected into a three-neck flask fitted with a reflux condenser, thermocouple, and magnetic stir bar under an inert nitrogen atmosphere. The flask is heated to 105 ^{o}C and cycled three times between vacuum and nitrogen to remove any remaining water. The reaction is then heated to 150 ^{o}C and a solution of 1,3-diethyl-imidazolidine-2-selenone (1 mmol, 1.97 g) and diphenyl ether (0.5 mL) is injected. The temperature is then set to 225 ^{o}C and the solution is allowed to react for 6 hours. The reactivity of the W precursor will decrease if the solution is held for an extended time at any temperature besides the 225 ^{o}C reaction temperature. The solution will be an orange color until nucleation occurs, at which time it will become black. The flask is then cooled to room temperature and 8 mL of toluene are injected. 8 mL methanol is added and the solution is centrifuged. The precipitate is washed and centrifuged twice more with 1:1 toluene:MeOH and is finally suspended in toluene.

4.4.3 *Synthesis of 1,3-Diethyl-imidazolidine-2-selenone*

Adapted from Zhou *et al*.[221] 8.316 mL (50 mmol) triethyl orthoformate, 1.669 mL (25 mmol) N,N′-dimethylethylenediamine, and 1.974 g (25 mmol) Se are combined in an air-free single-neck round bottom Schlenk flask with a magnetic stir bar. Following three freeze-pump-thaw cycles, the reaction mixture is placed under vacuum, heated to 180 ^{o}C, and held at that temperature for 6+ hours. (Yield will depend on how much unreacted selenium is left.) After cooling to room temperature, the flask is opened to air and minimal acetonitrile is added. The

orange-colored liquid is passed through a 0.45 um PTFE syringe filter into a scintillation vial, which is then sealed and placed in the freezer to recrystallize. Product forms needle-like colorless crystals which can be filtered and vacuum dried. The product is stored in the freezer in the glovebox. For best yield, save filtered supernat and then remove the solvent under vacuum until orange crystals are left. Add minimal amount of acetonitrile (if recrystallizing in a glovebox) to dissolve and recrystallize in freezer; repeat as necessary to maximize yield. Outside of a glovebox, a 3:1 ether:ethanol mix is best for recrystallization.

Caution: This reaction produces vile smelling by-products and it is recommended that all items used (including gloves) be either doused in a bleach bath before disposal or placed in a separate disposal container that is only opened within a fumehood.

4.4.4 *Characterization*

Scanning electron microscope (SEM) images were acquired with a FEI XL830 dual beam instrument with integrated electron dispersive X-ray spectrometer (EDS) by Oxford. Typical operating conditions were 5 keV electron beam for SEM and 20 keV for EDS. Powder X-ray diffraction patterns (XRD) were taken with a Bruker D8 Discover with GADDS 2-D XRD using Cu ka radiation. X-ray photoelectron spectroscopy (XPS) and ultraviolet photoelectron spectroscopy (UPS) was performed under high vacuum conditions in a Kratos AXIS Ultra instrument; samples were prepared by dropcasting the nanocrystals from an organic suspension on to a clean piece of Si or Ti, typically within a glovebox. Once on the substrate, samples were treated by annealing or chemical stripping as mentioned in the text and quickly transferred to the instrument chamber to minimize oxidation in air. Electrodes and XPS/UPS samples were annealed under Ar in a tube furnace with a boat containing Se powder upstream. Samples were

exposed to air during transfer to and from the furnace but stored in a glovebox until analysis. XPS spectra were referenced to the C-C peak at 284.4 eV and UPS spectra were referenced to a Au sample. A Bruker Vertex 70 Fourier transform infrared spectrometer (FTIR) and a TA Q50 thermogravimetric analyzer (TGA) were also used for characterization. Raman spectra were collected by a confocal Horiba instrument with 514 nm incident light. Samples were dropcasted on to glass slides for measurement and carefully monitored for changes due to local heating by the laser.

4.4.5 *Electrochemical Characterization (courtesy of Danielle Henckel)*

Electrochemical measurements were conducted in a custom four-neck cell fitted with a platinum coil auxiliary electrode separated in a fritted compartment, a $Ag/AgSO_4$ reference electrode separated by a Vycor frit and a working electrode. The working electrodes used in this study were fabricated from carbon paper (Fuel Cell Store, Spectracarb 2050A 0850). The carbon fiber electrodes were made by cutting a 1 cm x 3 cm rectangle and attaching a copper wire with silver epoxy to the electrode material. The copper wire/silver epoxy was then covered with gel epoxy to create a 1 cm x 1 cm surface area. (Note: the backside of the electrode was not covered due to its porosity with epoxy leaking onto both sides.)

All cyclic voltammograms depicting proton reduction were performed after sparging the cell with Ar or N_2. The electrolyte solution is 0.5 M H_2SO_4 in 18 MΩ Millipore water. All measurements in this study was referenced to RHE, which was measured using a platinum coil electrode in H_2 saturated 0.5 M H_2SO_4. Tafel slope analysis was performed on LSVs with 5 mV/s scan rate from the onset of the reductive current to ~150mV after the onset and fitted to a best fit line. In cases where the fit wasn't linear in this region, the line was fit to the initial linear portion of the curve. A Gamry Interface 1000 was used for all electrochemical measurements.

Chapter 5. CONCLUSIONS AND FUTURE WORK

In this thesis, three different chalcogenide materials were investigated for application in solar cells as the absorber layer. With an initial goal of fabricating each material through colloidal synthesis for future scalability in both synthesis and layer deposition, I looked in to FeS_2, Fe_2GeS_4, and WSe_2 nanomaterials. FeS_2 has demonstrated inherent issues that will keep it from implementation as a solar absorber in its current form. There is perhaps a potential to dope the material, but additional elements and processing steps make FeS_2 less desirable for the motivations of this thesis and for its general use in PV applications. Instead of investigating doping FeS_2, I then moved on to Fe_2GeS_4 as related compound, but with a different crystal structure and thermodynamic stability that could potentially avoid the bulk and surface issues found in FeS_2.

In the course of investigating this material, I modified a published synthesis to make Fe_2GeS_4 less reliant on expensive, air-sensitive, and pungent precursors, and shortened the reaction time, which helps decrease the energy input and could shrink the energy payback period for any future PV devices. Characterization of the material revealed that Fe_2GeS_4 is S-deficient as synthesized and the V_S result in a degenerate *n*-type semiconductor. Annealing with H_2S eliminated V_S and reduced the degeneracy of the material and weak PL emission was observed under high sun illumination conditions. In order for this material to be a viable PV candidate, I believe a deeper understanding of the material through a single crystal study is critical. If the single crystal samples demonstrate strong PL and good mobilities, then work should continue on the nanocrystal form. But, if like FeS_2, there is are inherent issues beyond V_S, they would be revealed most clearly in a single crystal study and if they cannot be overcome in the single crystal system, then it is likely they cannot be overcome in the nanocrystal system.

The positive case for WSe_2 for solid-state PV is hard to make after this investigation. While the material has attractive individual properties, the issues of anisotropic transport, high concentration of recombination sites due to edge sites, diminished PL with increased layer number, and co-existence of a metallic polytype are individually challenging to overcome, let alone overcoming all of them in one material. Though I was able to demonstrate the successful synthesis of fully 2H semiconducting WSe_2 nanocrystals, I was unable to solve the other issues with the material. While this does not completely exclude WSe_2 and other TMDCs from solar applications, I would suggest continuing to look into single layer devices and photoelectrochemical cells, as these specific cases appear to be where the TMDC properties excel. These device configurations can eliminate one or more of the issues outlined for PV application of TMDCs.

The TMDCs, as evidenced by the WSe_2 studied in this work, have solid potential for applications in hydrogen evolution. With the ability to tailor morphology, polytype, and surface chemistry through colloidal synthesis, the activity of these materials can be rapidly advanced. The research discussed here brings more insight into how ligands affect both the physical and electronic properties of WSe_2 and how the resulting material performs as a catalyst for HER. Though experimental work needs to be done for confirmation, it is likely that the trends uncovered in this WSe_2 research can be extended to the other TMDC materials, especially the Mo and S systems.

LIST OF PUBLICATIONS

Henckel, Danielle A., Olivia Lenz, and Brandi M. Cossairt. "Effect of Ligand Coverage on Hydrogen Evolution Catalyzed by Colloidal WSe2." ACS Catalysis 7.4 (2017): 2815-2820.

Lenz, Olivia, Danielle A., Henckel, Kannan M. Krishnan, and Brandi M Cossairt. “Improved HER Catalysis through Facile, Aqueous Intercalation of Nanoscale WSe2.” *In preparation*

Lenz, Olivia, and Kannan M. Krishnan. “Colloidal synthesis, thermal stability, and electronic characterization of Fe2GeS4 nanocrystals with air-stable precursors.” *In preparation.*

BIBLIOGRAPHY

(1) Vesborg, P. C. K.; Seger, B.; Chorkendorff, I. *J. Phys. Chem. Lett.* **2015**, *6* (6), 951.
(2) *The Future of Solar Energy*; 2015.
(3) Jones-Albertus, R.; Feldman, D.; Fu, R.; Horowitz, K.; Woodhouse, M. *Prog. Photovoltaics Res. Appl.* **2016**, *24* (9), 1272.
(4) Park, N. G. *Mater. Today* **2015**, *18* (2), 65.
(5) Green, M. a. *Prog. Photovoltaics Res. Appl.* **2001**, *9* (2), 123.
(6) Conibeer, G. *Mater. Today* **2007**, *10* (11), 42.
(7) Shockley, W.; Queisser, H. J. *J. Appl. Phys.* **1961**, *32* (3), 510.
(8) Wadia, C.; Alivisatos, a P.; Kammen, D. M. *Environ. Sci. Technol.* **2009**, *43* (6), 2072.
(9) Alharbi, F.; Bass, J. D.; Salhi, A.; Alyamani, A.; Kim, H.; Miller, R. D. *Renew. Energy* **2011**, *36*, 2753.
(10) *Metal Chalcogenide Nanostructures for Renewable Energy Applications*; Qurashi, A., Ed.; John Wiley & Sons, Inc.: Hoboken, NJ, USA, 2014.
(11) LaMer, V.; Dinegar, R. *J. Am. Chem. ...* **1950**, *72* (8), 4847.
(12) Hillhouse, H. W.; Beard, M. C. *Curr. Opin. Colloid Interface Sci.* **2009**, *14* (4), 245.
(13) Ennaoui, A.; Fiechter, S.; Pettenkofer, C.; Alonsovante, N.; Buker, K.; Bronold, M.; Hopfner, C.; Tributsch, H. *Sol. Energy Mater. Sol. Cells* **1993**, *29* (4), 289.
(14) Layek, A.; Middya, S.; Ray, P. P. *J. Mater. Sci. Mater. Electron.* **2013**.
(15) Mao, B.; Dong, Q.; Xiao, Z.; Exstrom, C. L.; Darveau, S. a.; Webber, T. E.; Lund, B. D.; Huang, H.; Kang, Z.; Huang, J. *J. Mater. Chem. A* **2013**.
(16) Vasekar, P. S.; Dhakal, T. P. **2013**.
(17) Khan, M. A.; Manasreh, M. O.; Kang, Y. *Mater. Lett.* **2014**.
(18) Ennaoui, A; Fiechter, S. *J. Electrochem. Soc.* **1986**, *133* (1).
(19) Smestad, G.; Ennaoui, A.; Fiechter, S.; Tributsch, H.; Hofmann, W. k.; Birkholz, M.; Kautek, W. *Sol. Energy Mater.* **1990**, *20*, 149.
(20) Ferrer, I. J.; Sanchez, C. *J. Appl. Phys.* **1991**, *70* (5), 2641.
(21) Rezig, B.; Dahman, H.; Kenzari, M. *Renew. Energy* **1992**, *2* (2), 125.
(22) Jagadeesh, M. S.; Seehra, M. S. *Phys. Lett. A* **1980**, *80* (1), 59.
(23) Bullett, D. *J. Phys. C solid state Phys.* **1982**, *15*, 6163.
(24) Ferrer, I. J.; Ares, J. R.; Sánchez, C. R. *Sol. Energy Mater. Sol. Cells* **2003**, *76* (2), 183.
(25) Altermatt, P. P.; Kiesewetter, T.; Ellmer, K. **2002**, *71*, 181.
(26) Kou, W. W.; Seehra, M. S. *Phys. Rev. B* **1978**, *18* (12), 7062.
(27) Birkholz, M.; Hartmann, A.; Tributsch, H. *Phys. Rev. B* **1991**, *43* (14), 926.
(28) Lennie, A. R.; Vaughan, D. J. *Am. Mineral.* **1992**, *77*, 1166.
(29) Buerger, M. *Am. Miner.* **1934**, *19* (2), 37.
(30) Meng, L.; Liu, M. S. *Mater. Sci. Eng. B* **1999**, *60*, 168.
(31) Huang, L.; Wang, F.; Luan, Z.; Meng, L. *Mater. Lett.* **2010**, *64* (23), 2612.
(32) Seefeld, S.; Limpinsel, M.; Liu, Y.; Farhi, N.; Weber, A.; Zhang, Y.; Berry, N.; Kwon, Y. J.; Perkins, C. L.; Hemminger, J. C.; Wu, R.; Law, M. *J. Am. Chem. Soc.* **2013**, *135* (11), 4412.

(33) Li, L.; Cabán-Acevedo, M.; Girard, S. N.; Jin, S. *Nanoscale* **2014**.
(34) Hoare, I. C.; Hurst, H. J.; Stuart, W. I.; White, T. J. **1988**, *84* (9), 3071.
(35) Soukup, R. J.; Prabukanthan, P.; Ianno, N. J.; Sarkar, A.; Kamler, C. a.; Sekora, D. G. *J. Vac. Sci. Technol. A Vacuum, Surfaces, Film.* **2011**, *29* (1), 11001.
(36) Dhakal, T.; Ganta, L. *... (PVSC), 2012 38th ...* **2012**, 170.
(37) Jagadeesh, M. S.; Seehra, M. S. **1981**, *2153*.
(38) Lehner, S.; Ciobanu, M.; Savage, K.; Cliffel, D. E. *J. Electrochem. Soc.* **2008**, *155* (5), P61.
(39) Büker, K.; Alonso-vante, N.; Tributsch, H. *J. Appl. Phys.* **1992**, *72* (12), 5721.
(40) Fiechter, S.; Birkholz, M.; Hartmann, A.; Dulski, P.; Giersig, M.; Tributsch, H.; Tilley, R. J. D. *J. Mater. Res.* **1992**, *7* (7), 1829.
(41) Lehner, S. W.; Newman, N.; van Schilfgaarde, M.; Bandyopadhyay, S.; Savage, K.; Buseck, P. R. *J. Appl. Phys.* **2012**, *111* (8), 83717.
(42) Cabán-Acevedo, M.; Kaiser, N. S.; English, C. R.; Liang, D.; Thompson, B. J.; Chen, H.-E.; Czech, K. J.; Wright, J. C.; Hamers, R. J.; Jin, S. *J. Am. Chem. Soc.* **2014**, *136* (49), 17163.
(43) Limpinsel, M.; Farhi, N.; Berry, N.; Lindemuth, J.; Perkins, C. L.; Lin, Q.; Law, M. *Energy Environ. Sci.* **2014**.
(44) Wan, D.; Wang, Y.; Wang, B.; Ma, C.; Sun, H.; Wei, L. *J. Cryst. Growth* **2003**, *253* (1–4), 230.
(45) Cabán-Acevedo, M.; Faber, M. S.; Tan, Y.; Hamers, R. J.; Jin, S. *Nano Lett.* **2012**, *12* (4), 1977.
(46) Wang, X.; Wang, G.; Chen, J.; Zhu, X.; Tian, J.; Liu, X.; Wang, R. *Mater. Lett.* **2013**, 4.
(47) Ding, L.; Fan, X.; Sun, X.; Du, J.; Liu, Z.; Tao, C. *RSC Adv.* **2013**, *3* (14), 4539.
(48) Khalid, S.; Ahmed, E.; Malik, M. *New J. ...* **2014**.
(49) Mlowe, S.; Lewis, D. J.; Malik, M. A.; Raftery, J.; Mubofu, E. B.; O'Brien, P.; Revaprasadu, N. *Dalt. Trans.* **2016**, *45* (6), 2647.
(50) Wilcoxon, J. P.; Bliss, D. E.; Martin, J. E.; Newcomer, P. P.; Samara, G. A.; Martino, A. *Photocatalytic Semiconductor Clusters for Fuel Production*; 1995.
(51) Wilcoxon, J.; Newcomer, P.; Samara, G. *Solid State Commun.* **1996**, *98* (6), 581.
(52) Anuar, K.; Ph, D.; Tan, W. T.; Saravanan, N.; Ho, S. M.; Sc, M. *Pacific J. Sci. Technol.* **2009**, *10* (2), 801.
(53) Lin, Y.; Wang, D.; Yen, H.; Chen, H.; Chen, C.; Chen, C.; Tang, C. **2009**, *405207*.
(54) Wadia, C.; Wu, Y.; Gul, S.; Volkman, S. K.; Guo, J.; Alivisatos, a. P. *Chem. Mater.* **2009**, *21* (13), 2568.
(55) Kassim, a; WeeTee, T.; Abdullah, D. *Indones. J. Chem.* **2010**, *2* (1), 8.
(56) Wang, D.; Wang, Q.; Wang, T. *CrystEngComm* **2010**, *12* (11), 3797.
(57) Wang, D.-W.; Wang, Q.-H.; Wang, T.-M. *CrystEngComm* **2010**, *12* (3), 755.
(58) Bi, Y.; Yuan, Y.; Exstrom, C. L.; Darveau, S. A.; Huang, J. *Nano Lett.* **2011**, *11* (11), 4953.
(59) Puthussery, J.; Seefeld, S.; Berry, N.; Gibbs, M.; Law, M. *J. Am. Chem. Soc.* **2011**, *133* (4), 716.
(60) Hsiao, S.-C.; Hsu, C.-M.; Chen, S.-Y.; Perng, Y.-H.; Chueh, Y.-L.; Chen, L.-J.; Chou, L.-H. *Mater. Lett.* **2012**, *75*, 152.

(61) Kirkeminde, A.; Ruzicka, B. a; Wang, R.; Puna, S.; Zhao, H.; Ren, S. *ACS Appl. Mater. Interfaces* **2012**, *4* (3), 1174.
(62) Macpherson, H. A.; Stoldt, C. R. *ACS Nano* **2012**.
(63) Reddy, Y. M.; Vedavathi, A. *Journal of Applied Sciences*. 2012, pp 1772–1774.
(64) Bai, Y.; Yeom, J.; Yang, M.; Cha, S.-H.; Sun, K.; Kotov, N. A. *J. Phys. Chem. C* **2013**, *117* (6), 2567.
(65) Zhu, L.; Richardson, B.; Tanumihardja, J.; Yu, Q. *CrystEngComm* **2012**, *14* (12), 4188.
(66) Gong, M.; Kirkeminde, A.; Ren, S. *Sci. Rep.* **2013**, *3*, 2092.
(67) Gong, M.; Kirkeminde, A.; Xie, Y.; Lu, R.; Liu, J.; Wu, J. Z.; Ren, S. *Adv. Opt. Mater.* **2013**, *1* (1), 78.
(68) Kirkeminde, A.; Ren, S. *J. Mater. Chem. A* **2013**, *1* (1), 49.
(69) Lucas, J.; Tuan, C.; Lounis, S.; Britt, D. *Chem. ...* **2013**, 2.
(70) Mangham, S. C.; Alam Khan, M.; Benamara, M.; Manasreh, M. O. *Mater. Lett.* **2013**, *97*, 144.
(71) Qiu, X.; Liu, M.; Hayashi, T.; Miyauchi, M.; Hashimoto, K. *Chem. Commun. (Camb).* **2013**, *49* (12), 1232.
(72) Zhu, L.; Richardson, B.; Yu, Q. *Nanoscale* **2013**, No. 207890.
(73) Ge, H.; Hai, L.; Prabhakar, R. R.; Ming, L. Y.; Sritharan, T. *RSC Adv.* **2014**, *4* (32), 16489.
(74) Li, W.; Dittrich, T.; Jäckel, F.; Feldmann, J. *Small* **2014**, 1.
(75) Xuefeng, Q.; Yi, X.; Yitai, Q. *Mater. Lett.* **2001**, *48*, 109.
(76) Duan, H.; Zheng, Y. F.; Dong, Y. Z.; Zhang, X. G.; Sun, Y. F. *Mater. Res. Bull.* **2004**, *39* (12), 1861.
(77) Kar, S.; Chaudhuri, S. *Chem. Phys. Lett.* **2004**, *398* (1–3), 22.
(78) Wu, R.; Zheng, Y. F.; Zhang, X. G.; Sun, Y. F.; Xu, J. B.; Jian, J. K. *J. Cryst. Growth* **2004**, *266* (4), 523.
(79) Chen, X.; Wang, Z.; Wang, X.; Wan, J.; Liu, J. *Inorg. Chem.* **2005**, *44* (4), 951.
(80) Kar, S.; Chaudhuri, S. *Mater. Lett.* **2005**, *59* (2–3), 289.
(81) Jiao, J.; Chen, L.; Kuang, D.; Gao, W.; Feng, H.; Xia, J. *RSC Adv.* **2011**, *1*, 255.
(82) Xia, J.; Jiao, J.; Dai, B.; Qiu, W.; He, S.; Qiu, W.; Shen, P.; Chen, L. *RSC Adv.* **2013**, *3* (17), 6132.
(83) Yoder, T. S.; Cloud, J. E.; Leong, G. J.; Molk, D. F.; Tussing, M.; Miorelli, J.; Ngo, C.; Kodambaka, S.; Eberhart, M. E.; Richards, R. M.; Yang, Y. *Chem. Mater.* **2014**, *26* (23), 6743.
(84) Kirkeminde, A.; Scott, R.; Ren, S. *Nanoscale* **2012**, No. 207890.
(85) Wang, D.-Y.; Jiang, Y.-T.; Lin, C.-C.; Li, S.-S.; Wang, Y.-T.; Chen, C.-C.; Chen, C.-W. *Adv. Mater.* **2012**, *24* (25), 3415.
(86) Schlegel, A.; Wachter, P. *J. Phys. C Solid State Phys.* **1976**, *9*, 3363.
(87) Folkerts, W.; Sawatzky, G.; Haas, C.; de Groot, R.; Hillebrecht, F. *J. Phys. C ...* **1987**, *20*, 4135.
(88) Goodenough, J. *Mater. Res. Bull.* **1978**, *13*, 1305.
(89) Opahle, I.; Koepernik, K.; Eschrig, H. *Comput. Mater. Sci.* **2000**, *17* (2–4), 206.
(90) Opahle, I.; Koepernik, K.; Eschrig, H. **1999**, *60* (20), 35.
(91) Zhao, C.; Wu, B.; Chen, J.; Li, Y.; Chen, Y. *Int. J. Miner. Metall. Mater.* **2013**, *20* (7),

671.
(92) Lichtenberger, D.; Ellmer, K.; Schieck, R.; Fiechter, S.; Tributsch, H. *Thin Solid Films* **1994**, *246* (1–2), 6.
(93) Ellmer, K.; Tributsch, H. *Proc. 12th Work. ...* **2000**, No. Quantsol, 10.
(94) Letters, P. **1980**, *80* (I), 77.
(95) Spagnoli, D.; Refson, K.; Wright, K.; Gale, J. D. *Phys. Rev. B* **2010**, *81* (9), 1.
(96) Sun, R.; Chan, M.; Ceder, G. *Phys. Rev. B* **2011**, *83* (23), 1.
(97) Yu, L.; Lany, S.; Kykyneshi, R.; Jieratum, V.; Ravichandran, R.; Pelatt, B.; Altschul, E.; Platt, H. A. S.; Wager, J. F.; Keszler, D. A.; Zunger, A. *Adv. Energy Mater.* **2011**, *1* (5), 748.
(98) Hu, J.; Zhang, Y.; Law, M.; Wu, R. *Phys. Rev. B* **2012**, *85* (8), 85203.
(99) Yu, L.; Lany, S.; Kykyneshi, R.; Jieratum, V.; Ravichandran, R.; Pelatt, B.; Altschul, E.; Platt, H. a. S.; Wager, J. F.; Keszler, D. a.; Zunger, A. *Adv. Energy Mater.* **2011**, *1* (5), 748.
(100) Zhang, Y.; Hu, J.; Law, M.; Wu, R. *Phys. Rev. B* **2012**, *85* (8), 1.
(101) Krishnamoorthy, A.; Herbert, F. W.; Yip, S.; Van Vliet, K. J.; Yildiz, B. *J. Phys. Condens. Matter* **2013**, *25* (4), 45004.
(102) Herbert, F. W.; Krishnamoorthy, a.; Van Vliet, K. J.; Yildiz, B. *Surf. Sci.* **2013**, *618*, 53.
(103) Limpinsel, M.; Farhi, N.; Berry, N.; Lindemuth, J.; Perkins, C. L.; Lin, Q.; Law, M. *Energy Environ. Sci.* **2014**, *7* (6), 1974.
(104) Bronold, M.; Pettenkofer, C.; Jaegermann, W. *J. Appl. Phys.* **1994**, *76* (10), 5800.
(105) Liang, D.; Caba, M.; Kaiser, N. S.; Jin, S. **2014**.
(106) Ho, C. H.; Huang, C. E.; Wu, C. C. *J. Cryst. Growth* **2004**, *270* (3–4), 535.
(107) Kunst, M.; Tributsch, H.; Thomas, B.; Ellmer, K.; Bohne, W.; Ro, J. **1999**, *111*, 235.
(108) Díaz-Chao, P.; Ares, J. R.; Ferrer, I. J.; Sánchez, C. *J. Mater. Sci.* **2013**, *48* (14), 4914.
(109) Yu, Q.; Cai, S.; Jin, Z.; Yan, Z. *Mater. Res. Bull.* **2013**, *48* (9), 3601.
(110) Samad, L.; Cab??n-Acevedo, M.; Shearer, M. J.; Park, K.; Hamers, R. J.; Jin, S. *Chem. Mater.* **2015**, *27* (8), 3108.
(111) Hu, J.; Zhang, Y.; Law, M.; Wu, R. *J. Am. Chem. Soc.* **2012**, *134* (32), 13216.
(112) Zhang, Y. N.; Law, M.; Wu, R. Q. *J. Phys. Chem. C* **2015**, *119* (44), 24859.
(113) Wang, Y.-C.; Wang, D.-Y.; Jiang, Y.-T.; Chen, H.-A.; Chen, C.-C.; Ho, K.-C.; Chou, H.-L.; Chen, C.-W. *Angew. Chem. Int. Ed. Engl.* **2013**, 6694.
(114) Shukla, S.; Loc, N. H.; Boix, P. P.; Koh, T. M.; Prabhakar, R. R. *ACS Nano* **2014**, *8* (10), 10597.
(115) Koo, B.; Jung, H.; Park, M.; Kim, J.-Y.; Son, H. J.; Cho, J.; Ko, M. J. *Adv. Funct. Mater.* **2016**, 1.
(116) Jieratum, V. Iron and Copper Chalcogenides: Photovoltaic Absorber Candidates and YZrF7: A New Upconversion Host, 2012.
(117) Fredrick, S. J.; Prieto, A. L. *J. Am. Chem. Soc.* **2013**, *1*, 1.
(118) Chesman, A. S. R.; Embden, J. Van; Gaspera, E. Della; Du, N. W.; Webster, N. A. S.; Jasieniak, J. J. *Chem. Mater.* **2014**, *26*, 5482.
(119) Yuan, M.; Kemp, K. W.; Thon, S. M.; Kim, J. Y.; Chou, K. W.; Amassian, A.; Sargent, E. H. *Adv. Mater.* **2014**, *26* (21), 3513.
(120) Orefuwa, S.; Lai, C.-Y.; Dobson, K.; Ni, C.; Radu, D. In *Materials Reseach Society*

Symposium; 2014; Vol. 1670, pp 1–5.
(121) Park, B.-I.; Yu, S.; Hwang, Y.; Cho, S.-H.; Lee, J.-S.; Park, C.; Lee, D.-K.; Lee, S. Y. *J. Mater. Chem. A* **2015**, *3* (5), 2265.
(122) McPhail, M. R.; Weiss, E. a. *Chem. Mater.* **2014**, No. May, 140515145706000.
(123) Atkins, B. P. W.; Child, M. S.; Phillips, C. S. G. *Tables Gr. Theory* **2006**, 1.
(124) Luther, J. M.; Law, M.; Song, Q.; Perkins, C. L.; Beard, M. C.; Arthur, J.; Nozik, A. J. *ACS Nano* **2008**, *2* (2), 271.
(125) Kameyama, T.; Osaki, T.; Okazaki, K.; Shibayama, T.; Kudo, A.; Kuwabata, S.; Torimoto, T. *J. Mater. Chem.* **2010**, *20* (25), 5319.
(126) Lammer, M. U.; Klemm, U.; Powalla, M. *Thin Solid Films* **2001**, *387*, 33.
(127) Thota, N.; Venkata Subbaiah, Y. P.; Prathap, P.; Reddy, Y. B. K.; Hema Chandra, G. *Phys. B Condens. Matter* **2014**, *449*, 255.
(128) Fernandes, P. A.; Salomé, P. M. P.; Cunha, A. F. da. *J. Phys. D. Appl. Phys.* **2010**, *43* (21), 215403.
(129) Upadhyayula, L. C. *J. Appl. Phys.* **1968**, *39* (10), 4736.
(130) Pospischil, A.; Furchi, M. M.; Mueller, T. *Nat. Nanotechnol.* **2014**, *9* (4), 257.
(131) Ma, Q.; Kyureghian, H.; Banninga, J. D.; Ianno, N. J. *MRS Proc.* **2014**, *1670*, mrss14.
(132) Cui, Q.; Ceballos, F.; Kumar, N.; Zhao, H. *ACS Nano* **2014**, *8* (3), 2970.
(133) Hossain, M. I.; Alharbi, F. H. *Mater. Technol. Adv. Perform. Mater.* **2013**, *28* (1), 88.
(134) Späh, R. *Appl. Phys. Lett.* **1983**, *43* (1), 79.
(135) Patel, P. R.; Rathod, J. R.; Patel, H. S.; Patel, K. D.; Pathak, V. M. *Adv. Mater. Res.* **2013**, *665* (1), 53.
(136) Tsirlina, T.; Cohen, S.; Cohen, H.; Sapir, L.; Peisach, M.; Tenne, R.; Matthaeus, A.; Tiefenbacher, S.; Jaegermann, W.; Ponomarev, E. A.; Lévy-Clément, C. *Sol. Energy Mater. Sol. Cells* **1996**, *44* (4), 457.
(137) Spectroscopy, D. P. *J Phys Chem* **1982**, *86*, 463.
(138) Agarwal, M. K.; Patel, P. D.; Vijayan, O. *Phys. status solidi* **1983**, *78* (1), 133.
(139) Klein, A.; Tomm, Y.; Schlaf, R.; Pettenkofer, C.; Jaegermann, W.; Lux-Steiner, M.; Bucher, E. *Sol. Energy Mater. Sol. Cells* **1998**, *51* (2), 181.
(140) Antunez, P. D.; Webber, D. H.; Brutchey, R. L. *Chem. Mater.* **2013**, *25* (12), 2385.
(141) Duphil, D.; Bastide, S.; Rouchaud, J. C.; Pastol, J. L.; Legendre, B.; Lévy-Clément, C. *Nanotechnology* **2004**, *15* (7), 828.
(142) James, D.; Zubkov, T. *J. Photochem. Photobiol. A Chem.* **2013**, *262*, 45.
(143) Yu, H.; Liu, Y.; Brock, S. L. **2008**, *47* (5), 1428.
(144) Jung, W.; Lee, S.; Yoo, D.; Jeong, S.; Miró, P.; Kuc, A.; Heine, T.; Cheon, J. *J. Am. Chem. Soc.* **2015**, *137* (23), 7266.
(145) Zhao, W.; Ribeiro, R. M.; Eda, G. *Acc. Chem. Res.* **2015**, *48* (1), 91.
(146) Tsai, C.; Chan, K.; Nørskov, J. K.; Abild-Pedersen, F. *Surf. Sci.* **2015**, *640*, 133.
(147) Yu, X.; Prévot, M. S.; Guijarro, N.; Sivula, K. *Nat. Commun.* **2015**, *6* (May), 7596.
(148) Yong, A.; Eng, S.; Ambrosi, A.; Sofer, Z.; Šimek, P.; Pumera, M.; Simek, P.; Yong, A.; Ambrosi, A.; Pumera, M. **2014**, No. 12, 12185.
(149) Ambrosi, A.; Sofer, Z.; Pumera, M. *Chem. Commun.* **2015**, 2.
(150) Lukowski, M. a; Daniel, A. S.; English, C. R.; Meng, F.; Forticaux, A.; Hamers, R. J.; Jin, S. *Energy Environ. Sci.* **2014**, *7* (8), 2608.

(151) Voiry, D.; Yamaguchi, H.; Li, J.; Silva, R.; Alves, D. C. B.; Fujita, T.; Chen, M.; Asefa, T.; Shenoy, V. B.; Eda, G.; Chhowalla, M. *Nat. Mater.* **2013**, *12* (9), 850.
(152) Agarwal, M. K.; Jani, A. R.; Kshtriya, J. D.; Vashi, M. N. *Cryst. Res. Technol.* **1984**, *19* (12), 1575.
(153) Mahalu, D.; Jakubowicz, A.; Wold, A.; Tenne, R. *Phys. Rev. B* **1988**, *38* (2), 1533.
(154) Jakubowicz, A.; Mahalu, D.; Wolf, M.; Wold, A.; Tenne, R. *Phys. Rev. B* **1989**, *40* (5), 2992.
(155) Mahalu, D.; Margulis, L.; Wold, A.; Tenne, R. *Phys. Rev. B* **1992**, *45* (4), 1943.
(156) Hodes, G. *Appl. Phys. Lett.* **1989**, *54* (21), 2085.
(157) Hodes, G.; Watkins, E.; Mantell, D.; Brillson, L. J.; Peisach, M.; Wold, A. *J. Appl. Phys.* **1992**, *71* (10), 5077.
(158) Mahalu, D.; Peisach, M.; Jaegermann, W.; Wold, A.; Tenne, R. *J. Phys. Chem.* **1990**, *94* (21), 8012.
(159) Bernede, J. C.; Hadouda, H.; Li, S. J.; Essaidi, H.; Pouzet, J.; Khelil, A. *J. Phys. III* **1996**, *6* (12), 1697.
(160) Cabrera, C. R.; Abruna, H. D. *J. Phys. Chem.* **1985**, *89* (8), 1279.
(161) Akari, S.; Lux-Steiner, M. C.; Glockler, K.; Schill, T.; Heitkamp, R.; Koslowski, B.; Dransfeld, K. *Ann. Phys.* **1993**, *505* (2), 141.
(162) Parkinson, B. a.; Furtak, T. E.; Canfield, D.; Kam, K.-K.; Kline, G. *Faraday Discuss. Chem. Soc.* **1980**, *70*, 233.
(163) Prasad, G.; Srivastavat, N. *Semicond. Sci. Technol.* **1993**, *8*, 2161.
(164) White, H. S.; Fan, F. F.; Bard, A. J. *J. Electrochem. Soc.* **1981**, *128* (5), 1045.
(165) *Photoelectrochemistry and Photovoltaics of Layered Semiconductors*; Aruchamy, A., Ed.; Physics and Chemistry of Materials with Low-Dimensional Structures; Springer Netherlands: Dordrecht, 1992; Vol. 14.
(166) Zhao, W.; Ribeiro, R. M.; Toh, M.; Carvalho, A.; Kloc, C.; Castro Neto, A. H.; Eda, G. *Nano Lett.* **2013**, *13* (11), 5627.
(167) Arora, A.; Koperski, M.; Nogajewski, K.; Marcus, J.; Faugeras, C.; Potemski, M. *Nanoscale* **2015**, *7* (23), 10421.
(168) Sahin, H.; Tongay, S.; Horzum, S.; Fan, W.; Zhou, J.; Li, J.; Wu, J.; Peeters, F. M. *Phys. Rev. B - Condens. Matter Mater. Phys.* **2013**, *87* (16), 1.
(169) Terrones, H.; Del Corro, E.; Feng, S.; Poumirol, J. M.; Rhodes, D.; Smirnov, D.; Pradhan, N. R.; Lin, Z.; Nguyen, M. a T.; Elías, a L.; Mallouk, T. E.; Balicas, L.; Pimenta, M. a; Terrones, M. *Sci. Rep.* **2014**, *4*, 4215.
(170) Zhao, W.; Ghorannevis, Z.; Amara, K.; Pang, J. *Nanoscale* **2013**, *5* (20), 9677.
(171) Xue, X.; Ji, W.; Mao, Z.; Mao, H.; Wang, Y.; Wang, X.; Ruan, W.; Zhao, B.; Lombardi, J. R. *J. Phys. Chem. C* **2012**, *116* (15), 8792.
(172) Islam, M. N.; Pradhan, A.; Kumar, S. *J. Appl. Phys.* **2005**, *98* (2).
(173) Ning, Z.; Voznyy, O.; Pan, J.; Hoogland, S.; Adinolfi, V.; Xu, J.; Li, M.; Kirmani, A. R.; Sun, J.; Minor, J.; Kemp, K. W.; Dong, H.; Rollny, L.; Labelle, A.; Carey, G.; Sutherland, B.; Hill, I.; Amassian, A.; Liu, H.; Tang, J.; Bakr, O. M.; Sargent, E. H. *Nat. Mater.* **2014**, *13* (8), 822.
(174) Tsai, C.; Chan, K.; Abild-Pedersen, F.; Nørskov, J. K. *Phys. Chem. Chem. Phys.* **2014**, *16* (26), 13156.
(175) Velazquez, J. M.; Saadi, F. H.; Pieterick, A. P.; Spurgeon, J. M.; Soriaga, M. P.;

Brunschwig, B. S.; Lewis, N. S. *J. Electroanal. Chem.* **2014**, *716*, 45.
(176) Ma, C.-B.; Qi, X.; Chen, B.; Bao, S.; Yin, Z.; Wu, X.-J.; Luo, Z.; Wei, J.; Zhang, H.-L.; Zhang, H. *Nanoscale* **2014**, *6* (11), 5624.
(177) Benck, J. D.; Hellstern, T. R.; Kibsgaard, J.; Chakthranont, P.; Jaramillo, T. F. *ACS Catalysis*. 2014, pp 3957–3971.
(178) Lukowski, M. a.; Daniel, A. S.; Meng, F.; Forticaux, A.; Li, L.; Jin, S. *J. Am. Chem. Soc.* **2013**, *135* (28), 10274.
(179) Voiry, D.; Salehi, M.; Silva, R.; Fujita, T.; Chen, M.; Asefa, T.; Shenoy, V. B.; Eda, G.; Chhowalla, M. *Nano Lett.* **2013**, *13* (12), 6222.
(180) Wang, H.; Kong, D.; Johanes, P.; Cha, J. J.; Zheng, G.; Yan, K.; Liu, N.; Cui, Y. *Nano Lett.* **2013**.
(181) Seo, B.; Jeong, H. Y.; Hong, S. Y.; Zak, A.; Joo, S. H. *Chem. Commun.* **2015**, *51*, 8334.
(182) Wang, D.; Pan, Z.; Wu, Z.; Wang, Z.; Liu, Z. *J. Power Sources* **2014**, *264*, 229.
(183) Li, H.; Wu, J.; Yin, Z.; Zhang, H. *Acc. Chem. Res.* **2014**, *47* (4), 1067.
(184) Chen, L.; Liu, B.; Abbas, A. N.; Ma, Y.; Fang, X.; Liu, Y.; Zhou, C. *ACS Nano* **2014**, *8* (11), 11543.
(185) Xu, K.; Wang, F.; Wang, Z.; Zhan, X.; Wang, Q.; Cheng, Z.; Safdar, M.; He, J. *ACS Nano* **2014**, *2* (8), 8468.
(186) Eichfeld, S. M.; Hossain, L.; Lin, Y.; Piasecki, A. F.; Kupp, B.; Birdwell, a G.; Burke, R. a; Lu, N.; Peng, X.; Li, J.; Azcatl, A.; Mcdonnell, S.; Wallace, R. M.; Kim, M. J.; Mayer, T. S.; Redwing, J. M.; Robinson, J. a. *ACS Nano* **2015**, *9* (2), 2080.
(187) Huang, J.; Pu, J.; Hsu, C.; Chiu, M. *ACS ...* **2014**, No. 1, 923.
(188) Mayorga-Martinez, C. C.; Ambrosi, A.; Eng, A. Y. S.; Sofer, Z.; Pumera, M. *Electrochem. commun.* **2015**, *56*, 24.
(189) Morales-Guio, C. G.; Stern, L.-A.; Hu, X. *Chem. Soc. Rev.* **2014**, *43* (18), 6555.
(190) Bushmarinov, I. S.; Goloveshkin, A. S.; Lenenko, N. D.; Zaikovskii, V. I.; Korlyukov, A. A.; Golub, A. S.; Eremenko, I. L. *J. Phys. Chem. Lett.* **2016**, 5162.
(191) Vanchura, B. A.; He, P.; Antochshuk, V.; Jaroniec, M.; Ferryman, A.; Barbash, D.; Fulghum, J. E.; Huang, S. D. *J. Am. Chem. Soc.* **2002**, *124* (41), 12090.
(192) Jiang, M.; Zhang, J.; Wu, M.; Jian, W.; Xue, H.; Ng, T.-W.; Lee, C.-S.; Xu, J. *J. Mater. Chem. A* **2016**, *4* (39), 14949.
(193) Bain, C. D.; Whitesides, G. M. *J. Am. Chem. Soc.* **1989**, *111* (18), 7155.
(194) Yurdakoc, M. K. *Turkish J. Chem.* **1999**, *23*, 105.
(195) Vrubel, H.; Moehl, T.; Grätzel, M.; Hu, X. *Chem. Commun.* **2013**, *49* (79), 8985.
(196) Morales-Guio, C. G.; Liardet, L.; Hu, X. *J. Am. Chem. Soc.* **2016**, *138* (28), 8946.
(197) Henckel, D. A.; Lenz, O.; Cossairt, B. M. *ACS Catal.* **2017**, 2815.
(198) Gorzkowski, M. T.; Lewera, A. *J. Phys. Chem. C* **2015**, *119* (32), 18389.
(199) Zeradjanin, A. R.; Grote, J. P.; Polymeros, G.; Mayrhofer, K. J. J. *Electroanalysis* **2016**, 2256.
(200) Kuc, A. In *Chemical Modelling: Volume 11*; 2014; Vol. 11, pp 1–29.
(201) Lebègue, S.; Eriksson, O. *Phys. Rev. B* **2009**, *79* (11), 115409.
(202) Gao, M.-R.; Chan, M. K. Y.; Sun, Y. *Nat. Commun.* **2015**, *6* (May), 7493.
(203) Goloveshkin, A. S.; Bushmarinov, I. S.; Korlyukov, A. A.; Buzin, M. I.; Zaikovskii, V. I.; Lenenko, N. D.; Golub, A. S. *Langmuir* **2015**, *31* (32), 8953.

(204) Goloveshkin, A. S.; Lenenko, N. D.; Zaikovskii, V. I.; Golub, A. S.; Korlyukov, A. A.; Bushmarinov, I. S. *RSC Adv.* **2015**, *5* (25), 19206.
(205) Mahler, B.; Hoepfner, V.; Liao, K.; Ozin, G. A. *J. Am. Chem. Soc.* **2014**, *136* (40), 14121.
(206) Corro, E.; Terrones, H.; Elias, A.; Fantini, C.; Feng, S.; Nguyen, M. A.; Mallouk, T. E.; Terrones, M.; Pimenta, M. A.; Fisica, D. De; Federal, U.; Gerais, D. M.; Carlos, A. A.; Postal, C.; Horizonte, B.; Corro, D. E. L.; Al, E. T. **2014**, No. 9, 9629.
(207) Coehoorn, R.; Haas, C.; de Groot, R. A. *Phys. Rev. B* **1987**, *35* (12), 6203.
(208) Lu, X.; Luo, X.; Zhang, J.; Quek, S. Y.; Xiong, Q. *Nano Res.* **2016**, No. November.
(209) Akintola, K.; Andrews, G. T.; Curnoe, S. H.; Koehler, M. R.; Keppens, V. *J. Phys. Condens. Matter* **2015**, *27* (39), 395401.
(210) Zeng, H.; Liu, G.-B.; Dai, J.; Yan, Y.; Zhu, B.; He, R.; Xie, L.; Xu, S.; Chen, X.; Yao, W.; Cui, X. *Sci. Rep.* **2013**, *3*, 1608.
(211) Ma, Y. G.; Liu, B. L.; Zhang, A. Y.; Chen, L.; Fathi, M.; Shen, C. F.; Abbas, A. N.; Ge, M. Y.; Mecklenburg, M.; Zhou, C. W. *ACS Nano* **2015**, *9* (7), 7383.
(212) Luo, X.; Zhao, Y.; Zhang, J.; Toh, M.; Kloc, C.; Xiong, Q.; Quek, S. Y. *Phys. Rev. B - Condens. Matter Mater. Phys.* **2013**, *88* (19), 1.
(213) Zhang, M.; Wu, X. J.; Zhu, X. Y.; Dumcenco, X. D. O.; Hong, J.; Mao, N. **2014**.
(214) Jiménez Sandoval, S.; Yang, D.; Frindt, R. F.; Irwin, J. C. *Phys. Rev. B* **1991**, *44* (8), 3955.
(215) Leng, K.; Chen, Z.; zhao, xiaoxu; Tang, W.; Tian, B.; Nai, C. T.; Zhou, W.; Loh, K. P. *ACS Nano* **2016**, acsnano.6b05746.
(216) Chou, S. S.; Huang, Y. K.; Kim, J.; Kaehr, B.; Foley, B. M.; Lu, P.; Dykstra, C.; Hopkins, P. E.; Brinker, C. J.; Huang, J.; Dravid, V. P. *J. Am. Chem. Soc.* **2015**, *137* (5), 1742.
(217) Guo, Y.; Sun, D.; Ouyang, B.; Raja, A.; Song, J.; Heinz, T. F.; Brus, L. E. *Nano Lett.* **2015**, *15* (8), 5081.
(218) Kong, D.; Wang, H.; Cha, J. J.; Pasta, M.; Koski, K. J.; Yao, J.; Cui, Y. *Nano Lett.* **2013**, *13* (3), 1341.
(219) Wang, H.; Lu, Z.; Kong, D.; Sun, J.; Hymel, T. M.; Cui, Y. *ACS Nano* **2014**, *8* (5), 4940.
(220) Ouyang, Y.; Ling, C.; Chen, Q.; Wang, Z.; Shi, L.; Wang, J. *Chem. Mater.* **2016**, *28* (12), 4390.
(221) Zhou, Y.; Denk, M. K. *Tetrahedron Lett.* **2003**, *44* (6), 1295.